GROUND MOTION PREDICTION EQUATIONS AND SPATIAL CORRELATION MODEL FOR ISTANBUL– DEVELOPED BY REAL AND SIMULATED GROUND MOTIONS

by

Hakan Süleyman

B.S., Civil Engineering, Yıldız Technical University, 2014

M.Sc., Earthquake Engineering, Boğaziçi University 2018

Submitted to the Kandilli Observatory and Earthquake Research Institute
in partial fulfillment of the requirements for the degree of
Doctor of Philosophy

Graduate Program in Earthquake Engineering
Boğaziçi University
2025

GROUND MOTION PREDICTION EQUATIONS AND SPATIAL CORRELATION MODEL FOR ISTANBUL– DEVELOPED BY REAL AND SIMULATED GROUND MOTIONS

APPROVED BY:

Prof. Eser Çaktı (Thesis Supervisor)	.....
Assoc. Prof. A. Özgün Konca	.....
Prof. Ufuk Hancılar	.....
Prof. Ayşegül Askan Gündoğan	.....
Assist. Prof. Ülgen Mert Tuğsal	.....

DATE OF APPROVAL: 20.09.2025

To my parents, with deepest gratitude and love.

ACKNOWLEDGEMENTS

I am grateful to my supervisor, Prof. Eser Çaktı, for her unwavering guidance, insightful feedback, and encouragement throughout this research. Her example has shaped both my scientific thinking and professional growth.

I am deeply grateful to my mother and father, whose endless love, sacrifices, and belief in me shaped who I am today, and to my wife for her patience, unwavering support, and steadfast companionship through every challenge of this journey.

I am indebted to the jury members—Prof. Ufuk Hancılar, Prof. Ayşegül Askan Gündoğan, Assoc. Prof. A. Özgün Konca, and Assist. Prof. Ülgen Mert Tuğsal—for their time, thoughtful reviews, and constructive comments that strengthened this dissertation.

I would also like to acknowledge the Earthquake Engineering Department of the Kandilli Observatory and Earthquake Research Institute for providing invaluable data and technical support that made this study possible.

This work was supported through the projects developed under TÜBİTAK 1001 program and the Tomorrow's Cities initiative, whose financial and institutional backing I gratefully acknowledge.

ABSTRACT

GROUND MOTION PREDICTION EQUATIONS AND SPATIAL CORRELATION MODEL FOR ISTANBUL– DEVELOPED BY REAL AND SIMULATED GROUND MOTIONS

This study develops regional ground-motion models for the Istanbul region by combining instrumental observations (M_W 4.0–6.1) with a large suite of synthetic broadband simulations (M_W 6.05–7.6). More than 170 stations in and around Istanbul were compiled and uniformly processed for model development. A stochastic simulation approach was first validated against five small-to-moderate Marmara earthquakes in both time and frequency domains. Following validation, broadband motions were generated for five historical Istanbul scenarios (1509 M_W 7.6; 1766 M_W 7.0–7.1; 1894 M_W 6.8–6.9) and 13 additional adapted global scenarios (Mw 6.05–7.6) on predefined rupture models, by merging the stochastic simulations with available 3-D physics-based deterministic simulations to cover 0.1–20 Hz range.

Three ground-motion prediction models (GMPEs) are constructed and evaluated: (i) an empirical GMPE calibrated on Marmara Sea events recorded in Istanbul (M_W 4.0–6.1); (ii) a machine-learning–enhanced GMPE trained on the same set of observations; and (iii) a synthetic-only GMPE for M_W 6.05–7.6 that addresses the lack of regional recordings for moderate-to-large events. Predictive performance is evaluated against well-established GMPEs through quantitative comparisons. To characterize spatial variability, empirical semivariograms of residuals are developed and fitted with exponential models, revealing a clear period-dependent correlation structure.

Overall, integrating observations with physically consistent broadband simulations improves predictive skill in magnitude–distance ranges that are poorly sampled by data and yields region-specific inputs suitable for engineering applications in Istanbul and the wider Marmara region.

ÖZET

İSTANBUL İÇİN GERÇEK VE BENZETİM YER HAREKETLERİ TABANLI YER HAREKETİ TAHMİN DENKLEMLERİ İLE MEKÂNSAL KORELASYON MODELİ

Bu çalışmada, İstanbul ve yakın bölgesindeki aletsel gözlemlerden (M_W 4.0–6.1) ve büyük bir geniş bant benzetimlerinden oluşan veri setlerinden (M_W 6.05–7.6) yararlanarak yer hareketi modelleri geliştirilmiştir. İstanbul ve çevresindeki 170'i aşkın istasyondan elde edilen kayıtlar derlenmiş, ve model geliştirmede kullanılmak üzere işlenmiştir. Benzetim oluşturmada kullanılan stokastik benzetim yaklaşımı, zaman ve frekans alanlarında beş küçük-orta büyüklükte Marmara depremine karşı doğrulanmıştır. Doğrulamanın ardından, kırılma modelleri üzerinde beş tarihsel İstanbul senaryosu (1509 M_W 7.6; 1766 M_W 7.0–7.1; 1894 M_W 6.8–6.9) ve buna ek olarak uyarlanmış 13 diğer senaryo (M_W 6.05–7.6) için geniş bant yer hareketleri üretilmiştir. Stokastik benzetimler, mevcut 3-B fizik temelli deterministik benzetimlerle birleştirilmiş ve 0.1–20 Hz aralığı kapsaması sağlanmıştır.

Üç adet yer hareketi tahmin deklemi (GMPE) oluşturulmuş ve başarımı ölçülmüştür. Bu kapsamda, (i) İstanbul'da kaydedilen Marmara Denizi depremlerine dayanarak oluşturulan ampirik bir GMPE (M_W 4.0–6.1); (ii) aynı gözlemsel veri kümesi üzerinde eğitilmiş ve makine öğrenimiyle zenginleştirilmiş bir GMPE; ve (iii) bölgedeki orta-büyük deprem eksikliğini gidermeyi amaçlayan, yalnızca benzetim verisine dayalı bir GMPE (M_W 6.05–7.6) geliştirilmiştir. Bu modellerin tahmin başarımı, literatürde yerleşik GMPE'lerle yapılan nicel karşılaştırmalarla değerlendirilmiştir. Mekânsal korelasyon modeli oluşturmak için rezidüel ampirik yarı varyogramları oluşturulmuş ve üstel modellerle karşılaştırılmış; sonuçlar, belirgin bir spektral periyoda bağımlı korelasyon yapısını ortaya koymuştur.

Genel olarak, gözlemler ile fiziksel olarak tutarlı geniş bant benzetimlerin bütünleştirilmesi, gerçek verinin sınırlandığı büyüklük–uzaklık aralıklarında tahmin başarımını artırmakta ve İstanbul ve yakın bölgesindeki mühendislik uygulamaları için bölgeye özgü girdiler sağlamaktadır.

TABLE OF CONTENTS

ACKNOWLEDGEMENTS iv
ABSTRACT v
ÖZET vi
LIST OF FIGURES x
LIST OF TABLES xiv
LIST OF SYMBOLS xv
LIST OF ACRONYMS/ABBREVIATIONS xviii
1. INTRODUCTION 1
1.1. Compilation and Standardization of Observed Data 1
1.2. Ground Motion Simulations 2
1.3. Development of a Hybrid Dataset 3
1.4. Ground Motion Prediction Equation Development 3
1.5. Spatial Correlation Model Development 5
2. REGIONAL SEISMOTECTONIC FRAMEWORK 7
3. DATASET COMPILATION AND DATA PROCESSING 9
3.1. Compilation and Unification of Earthquake Recording Catalogs 9
3.1.1. Station Data 10
3.1.2. Earthquake Data 10
3.1.2.1. Earthquake Information. 10
3.1.3. Initial Dataset Compilation 11
3.2. Data Processing 14
3.2.1. Baseline Correction and Bandpass Filtering 14
3.2.2. Onset Identification and the Duration of Ground Motion 15
3.2.2.1. Picking of P- and S-Wave Onsets. 15
3.2.2.2. Arias Intensity Computation. 15
3.2.3. Elimination of Low-Quality or Non-Representative Traces 15
3.2.4. Computation of Ground-Motion Parameters 15
3.2.4.1. Peak Ground Motion Values 15
3.2.4.2. Pseudo Spectral Acceleration and Rotation-Based Metrics. 16

3.2.5. Signal-to-Noise Ratio Evaluation 16
3.2.6. Final Outputs and Data Preservation 16
4. GROUND MOTION SIMULATIONS 18
4.1. Ground Motion Simulation Efforts for the Marmara Region 18
4.2. Stochastic Finite-Fault Ground Motion Modelling Algorithm, EXSIM 19
4.3. Validation of the EXSIM Algorithm for the Istanbul Region 21
4.4. Stochastic Ground Motion Simulations of Scenario Earthquakes 27
4.4.1. Testing the Validated Model 27
4.4.2. Simulations of Historical Istanbul Earthquakes 33
4.4.3. Simulations of Adapted Global Earthquakes 36
4.5. Broadband Ground Motion Simulations 38
5. GMPE DEVELOPMENT 44
5.1. GMPEs Developed Using Real Ground Motions 44
5.1.1. Data Selection and Filtering 44
5.1.1.1. Preliminary Data Filtering. 44
5.1.1.2. RotD50 Calculation for GMPE Development. 45
5.1.1.3. Final Dataset. 45
5.1.1.4. Partitioning the Dataset into Training and Test Sets. 45
5.1.2. Development of a Conventional GMPE Model 46
5.1.2.1. Magnitude Scaling Function, $f_{mag}(M)$. 46
5.1.2.2. Distance Attenuation Function, $f_{dist}(R, M)$. 46
5.1.2.3. Site Amplification Function, $f_{site}(V_{S30})$. 47
5.1.3. Exploration of Functional Forms 47
5.1.3.1. Distance Attenuation Models 47
5.1.3.2. Magnitude Scaling Models. 48
5.1.4. Two-Stage Regression Procedure 50
5.1.5. Site Amplification 50
5.1.5.1. Role of V_{S30} and Rock PGA. 50
5.1.5.2. Best-Fit Nonlinear Site Terms. 50
5.1.6. Final GMPE Formulation 51
5.1.7. Variability Analysis 54
5.1.7.1. Intra-Event and Inter-Event Residuals. 54
5.1.7.2. Model Comparison. 54

5.1.8. Machine-Learning–Enhanced GMPE 56
5.1.8.1. Gradient-Boosted Regression Trees 56
5.1.8.2. Integrating GBRT to GMPE model. 56
5.1.9. Model Comparison 57
5.1.10. Comparing the GMPE Models with Existing GMPEs 59
5.1.11. Concluding Remarks 63
5.2. GMPE Modeling with Synthetic Ground-Motion Data 63
6. SPATIAL CORRELATION MODEL DEVELOPMENT 75
6.1. Theoretical Framework of Spatial Correlation 75
6.1.1. Constructing the Semivariogram 76
6.1.2. Deriving the Spatial Correlation Function 76
6.1.3. Predictive Models 77
6.1.4. Assessing Isotropy 77
6.2. Analysis and Results 77
6.2.1. Empirical Semivariogram Analysis 77
6.2.2. Theoretical Model Fitting 79
6.2.3. Interpretation of Results 81
7. CONCLUSIONS 82
REFERENCES 84
APPENDIX A: STOCHASTIC AND 3D PHYSICS-BASED SIMULATION COMPARISONS 95
APPENDIX B: PREDICTIVE POWER EVALUATION OF THE DEVELOPED MODELS 105
APPENDIX C: PERIOD-DEPENDENT SPATIAL CORRELATION MODELS 132

LIST OF FIGURES

Figure 3.1. Geographical distribution of recording stations in the study region. 11

Figure 3.2. (a) Total number of recordings annually; (b) Total number of recordings annually, categorized by network. 12

Figure 3.3. (a) Total number of recordings based on VS30 bins; (b) Total number of recordings based on VS30 bins, categorized by network. 13

Figure 3.4. Distribution of the recordings, considering magnitude and hypocentral distance 14

Figure 4.1. Epicentral locations, magnitudes and occurrence dates of the five earthquakes considered in the validation study. 23

Figure 4.2. Finite-fault slip model developed in Karabulut et al. (2021) for M_W 5.8 Silivri earthquake; the values in grid cells show the variations in slip values, measured in cm 23

Figure 4.3. Comparison of observed and synthetic records in time and frequency domains 24

Figure 4.4. Observed versus simulated PGA and PGV values against hypocentral distance. 25

Figure 4.5. Simulated versus observed PGA and PGV comparisons 26

Figure 4.6. Residual analysis performed using spectral amplitudes in frequency domain 27

Figure 4.7. Segments considered for realizing scenario earthquakes. 28

Figure 4.8. V_{S30} map based on the studies of IMM (2007, 2009) and MTA (2004). 29

Figure 4.9. PGA distributions of M7.4 scenario, when hypocenter is located on east end of the rupture (a) and on the west of the rupture. 30

Figure 4.10. PGA distributions of M7.4 scenarios, considering stress parameter of (a) 100 bars, (b) 120 bars and (c) 130 bars 31

Figure 4.11. PGA distributions of M7.4 scenarios versus hypocentral distance, categorized in (a) site class C, (b) site class B and (c) site class A. 32

Figure 4.12. Two-dimensional displacement models in centimeters, generated using the Rupgen MATLAB routine 34

Figure 4.13. Distribution of PGA values obtained using the stochastic simulation method for five historical earthquakes. 35

Figure 4.14. Merged waveforms at four selected grid cells, in time domain and frequency domain 40

Figure 4.15. Distribution of PGA values obtained from broadband simulations for the 1894 (M_W 6.8 and M_W 6.9) and 1766 (M_W 7.0 and M_W 7.1) Istanbul earthquakes on the map 41

Figure 4.16. Distributions of RotD50 PSA at 0.3, 1 and 3 seconds obtained from broadband simulations for 1894 (M_W 6.8 and M_W 6.9) and 1766 (M_W 7.0 and M_W 7.1) Istanbul earthquakes on the map..... 43

Figure 5.1. Residuals versus hypocentral distance for PGA and PGV. 55

Figure 5.2. Predicted versus observed PGA, PSAs at 0.02-5 seconds and PGV comparisons 55

Figure 5.3. Residual analysis versus hypocentral distance for PGA and PGV..... 58

Figure 5.4. Comparisons of predicted and observed PGA and PGV 59

Figure 5.5. Predicted versus observed PGA, considering the GMPE model developed in this study and different GMPEs 60

Figure 5.6. Predicted versus observed PGV, considering the GMPE model developed in this study and different GMPEs 61

Figure 5.7. Comparison of magnitudes and distances in the synthetic and observational datasets 64

Figure 5.8. Comparison of (a) observational and synthetic data for M_W 7.2–7.4 range; (b) comparison for M_W 6.0–6.21 range. 65

Figure 5.9. Distribution of the training dataset versus R_{rup} for PGA and selected PSA values; curves denote mean predictions for selected M_W values, shaded regions indicate the ±1-sigma range, and points represent individual records in the dataset 66

Figure 5.10. Distribution of the training dataset versus M_W for PGA and selected PSA values; curves denote mean predictions for selected R_{rup} values, shaded regions indicate the ±1-sigma range, and points represent individual records in the dataset 69

Figure 6.1. Empirical semivariogram for PGA; circles represent mean values, while error ranges show ±1 standard deviation at distance bins 78

Figure A.1. Stochastic and 3D physics-based simulation comparisons in time domain; at selected grid cells 95

Figure B.1. Residuals versus hypocentral distance for PGA, PSA values at 0.02-5 seconds and PGV 105

Figure B.2. Predicted versus observed PGA, PSAs at 0.02-5 seconds and PGV comparisons 110

Figure B.3. Residual Analysis of the GMPEs as a function of hypocentral distance for PSA at periods 0.02–5.0 s 115

Figure B.4. Comparisons between observed PSA and GMPE predictions across the 0.02–5.0 s period range..... 121

Figure B.5. Comparison of observed and predicted PSA at 0.2 s using the GMPE developed in this study, benchmarked against alternative GMPEs 127

Figure B.6. Comparison of observed and predicted PSA at 0.5 s using the GMPE developed in this study, benchmarked against alternative GMPEs 128

Figure B.7. Comparison of observed and predicted PSA at 1.0 s using the GMPE developed in this study, benchmarked against alternative GMPEs 129

Figure B.8. Comparison of observed and predicted PSA at 2.0 s using the GMPE developed in this study, benchmarked against alternative GMPEs 130

Figure B.9. Comparison of observed and predicted PSA at 4.0 s using the GMPE developed in this study, benchmarked against alternative GMPEs 131

Figure C.1. Empirical semivariogram for periods between 0.02 – 5 seconds and PGV; circles represent mean values, while error ranges show ±1 standard deviation at distance bins..... 132

LIST OF TABLES

Table 4.1. Input parameters used in the stochastic simulations.....22

Table 4.2. Adapted source parameters used in the ground motion simulations. 33

Table 4.3. Finite-fault models adjusted to NAF for ground motion simulations. 37

Table 5.1. Coefficients of the prediction model. 53

Table 5.2. R^2 estimations for observed versus predicted PGA, selected PSA and PGV values.. 62

Table 5.3. Model agreement with training dataset quantified by R^2 estimations regarding NEHRP site classes. 72

Table 5.4. Coefficients of the ground-motion prediction model. 73

Table 6.1. Fitted model parameters for PGA, PGV and all PSA.....80

LIST OF SYMBOLS

A	Rupture area
a	Sill (semivariogram)
a(t)	Ground-acceleration time history
a_1, a_2	Peak ground acceleration thresholds
$a_E(t)$, $a_N(t)$	Orthogonal horizontal accelerations
$a_\theta(t)$	Rotational acceleration time series
b_i, c_i	GMPE regression coefficients (magnitude, distance, site terms)
b_{nl}	Nonlinear slope
b_1, b_2	Nonlinear slope parameters for specific V_{S30} ranges
c′, d′	Coefficients for the quadratic and cubic terms in the middle region
c_1, c_2	Coefficients for the near-field attenuation model
c_3, c_4	Coefficients for the far-field attenuation model
e_1, e_2	Coefficients for the low-magnitude model
e_3, e_4	Coefficients for the high-magnitude model
f	Frequency
f_c	Corner frequency
f_s	Sampling frequency
f_x	Crossover frequency used in broadband merging
f_{mag}, f_{dist}, f_{site}, f_{style}	Terms forming the prediction model
g	Gravitational acceleration
h	Separation (lag) distance
I_A	Arias intensity
L, W	Rupture length, width
L_{corr}	Correlation range (semivariogram)
ln	Natural logarithm
M	Earthquake magnitude

$\mathbf{M_o}$	Seismic moment
$\mathbf{M_D}$	Duration magnitude
$\mathbf{M_h}$	Hinge magnitude
$\mathbf{M_L}$	Local magnitude
$\mathbf{M_W}$	Moment magnitude
n	Nugget (semivariogram)
N	Number of samples
N(h)	Number of site pairs
$\mathbf{N_f}$	Filter order
$\mathbf{PGA_{rock}}$	Reference/rock peak ground acceleration used in nonlinear site term
PGA	Peak ground acceleration
$\mathbf{PGA_{low}}$	Lower bound PGA value for nonlinear amplification
PGV	Peak ground velocity
$\mathbf{Q_S(f)}$	Quality factor for S-waves
R	Distance
$\mathbf{R_{epi}}$	Epicentral distance
$\mathbf{R_h}$	Hinge distance
$\mathbf{R_{hyp}}$	Hypocentral distance
$\mathbf{R_{JB}}$	Joyner–Boore distance (to surface projection of rupture)
$\mathbf{R_{rup}}$	Closest distance to the ruptured plane
refPGA	Reference peak ground acceleration
$\mathbf{R^2}$	Coefficient of determination
RotD50	Median (50th-percentile) orientation-independent spectral ordinate
T	Spectral period
$\mathbf{t_p}$, $\mathbf{t_s}$	Start times of P-wave and S-wave
$\mathbf{V_1}$, $\mathbf{V_2}$	Shear wave velocity thresholds
$\mathbf{V_p}$	P-wave velocity
$\mathbf{V_r}$	Rupture velocity
$\mathbf{V_{ref}}$	Reference shear-wave velocity used in site term

V_{S30}	Shear-wave velocity in top 30 m
Y	The sum of the prediction model terms
Y_{ij}	Observed ground motion at site i, during earthquake j
$\overline{Y_{ij}}$	Median ground motion predicted by the GMPE
z	Depth of the hypocenter
Z(u), Z(u+h)	Random variables corresponding to normalized intra-event residuals
γ(h)	Semivariogram at lag h
Δ_{epi}	Great-circle distance in degrees
Δ_{GBRT}	ML-derived residual at the spectral period T
Δt	Sampling interval
Δx, Δy	Differences in log space for defining the polynomial coefficients
Δσ	Stress drop
δW	Within-event, site-centered residuals
ϵ_{ij}	Intra-event residuals
η_j	Inter-event residuals
κ_0	Site attenuation (zero-distance kappa)
μ	Mean
ρ	Crustal density
ρ(h)	Spatial correlation function at lag h
σ	Total standard deviation
τ	Between-event (inter-event) standard deviation
φ	Within-event (intra-event) standard deviation
ω_l, ω_h	Low and high corner frequencies

LIST OF ACRONYMS/ABBREVIATIONS

3D	Three-dimensional
AFAD	Disaster and Emergency Management Authority
Avg.	Average
EMSC	European-Mediterranean Seismological Centre
ESM	Engineering Strong Motion Database
EXSIM	Extended Finite-Fault Ground-Motion Simulation Algorithm
FAS	Fourier Amplitude Spectrum
GBRT	Gradient Boosted Regression Trees
GMPE	Ground Motion Prediction Equation
GPS	Global Positioning System
IERREWS	Istanbul Rapid Response and Early Warning System
IM	Intensity measure
IMM	Istanbul Metropolitan Municipality
KOERI	Kandilli Observatory and Earthquake Research Institute
ML	Machine-learning
MTA	Mineral Research and Exploration General Directorate
NAF	North Anatolian Fault
NEHRP	National Earthquake Hazards Reduction Program
NGA-West	Next Generation Attenuation Relationships for the western United States
PGA	Peak Ground Acceleration
PGV	Peak Ground Velocity
PSA	Pseudo-Spectral Acceleration
PSHA	Probabilistic Seismic Hazard Analysis
RETMC	Regional Earthquake-Tsunami Monitoring Center
RMSE	Root-mean-square error

SA	Spectral acceleration
SNR	Signal-to-Noise Ratio
SRCMOD	Earthquake Source Model Database

1. INTRODUCTION

Earthquake hazard assessments are vital for disaster preparedness and mitigation, particularly in regions prone to high seismic activity. Ground motion prediction equations (GMPEs) are essential tools for estimating the ground motion intensity of future earthquakes, and they play an integral role in earthquake hazard modeling. However, the reliability of GMPEs heavily depends on the availability of a comprehensive dataset, particularly for medium to large magnitude events. In many regions, including Istanbul and the Marmara region, the lack of sufficient observed ground motion data for such events presents a significant challenge in developing robust GMPEs. This study aims to address this critical gap by leveraging both observed and simulated datasets to develop comprehensive GMPEs for a wide range of magnitudes, including medium to large magnitude events, tailored to the unique seismotectonic setting of the region. Additionally, the study aims to develop a regional spatial correlation model by analyzing residual estimates between observed and predicted ground motions, providing insights into correlations between observation sites.

The primary purpose of this study is to overcome the limitations posed by the scarcity of ground motion recordings for medium to large magnitude earthquakes. To address this, the study employs a hybrid approach, combining high-quality observed data with rigorously validated ground motion simulations. The overarching goal is to create GMPEs that are both empirically grounded and enriched by simulated data, capturing a wide range of magnitudes and providing a more accurate representation of the region's seismic characteristics.

This research is structured around several critical steps, each contributing to the development of robust GMPEs for the Istanbul region.

1.1. Compilation and Standardization of Observed Data

This study begins with the systematic compilation of strong-motion recordings from the greater Istanbul region. The recording sources used to develop this dataset are the seismic networks of the Kandilli Observatory and Earthquake Research Institute (KOERI) and the Disaster and Emergency Management Authority (AFAD). These recordings were collected

from 171 stations and unified under a single, consistent database to ensure comprehensive regional coverage. A series of preprocessing steps were applied to standardize the recordings, eliminate inconsistencies, and ensure data quality. Special attention was devoted to assigning reliable metadata - including station coordinates, site conditions (V_{S30}), and earthquake source parameters such as magnitude and hypocentral distance, so that the dataset could serve as a robust foundation for ground-motion model development.

1.2. Ground Motion Simulations

Given the limited strong-motion recordings from medium-to-large earthquakes affecting wider Istanbul region, simulation-based ground motions are essential to close magnitude and distance gaps and enable robust hazard analyses. Recent regional studies show that well-calibrated simulations reproduce observed motions for moderate events and clarify when upper-magnitude ruptures may yield amplified shaking due to basin and directivity effects (Infantino et al., 2020). Stochastic finite-fault approaches tailored to Istanbul have produced site-specific spectra consistent with local recordings and historical damage patterns, including reconstructions of the 1509, 1766, and 1894 earthquakes (Zengin and Çaktı, 2012; Yenihayat, 2022). Focused simulations on the 26 September 2019 M_W 5.8 Silivri event demonstrates that region-tuned parameters successfully simulate recorded amplitudes and frequency content (Yenihayat et al., 2024). Medium-to-large magnitude rupture scenarios along central Marmara and the Princes' Islands segments further quantify epistemic uncertainties related to hypocenter location and stress parameters in site-specific estimates for Istanbul (Süleyman and Çaktı, 2024). Scenarios developed for simulating the M_W 7.2 Düzce earthquake of November 12, 1999, have made several contributions to the literature: near-fault records were successfully reproduced using EXSIM with a dynamic corner frequency; comparisons confirmed the engineering applicability of the results; and hybrid deterministic-stochastic methods yielded broadband time histories suitable for nonlinear analysis (Uğurhan and Aşkan, 2010; Karimzadeh et al., 2018; Özmen et al., 2020).

Building on this literature, the present dissertation generates broadband ground motions by combining region-calibrated stochastic finite-fault simulations with physics-based low-frequency predictions, then evaluates their consistency against observations using standard intensity measures such as peak ground acceleration (PGA), peak ground velocity

(PGV), and pseudo-spectral acceleration (PSA). This approach provides physically credible and empirically consistent inputs for the GMPE development (Uğurhan and Aşkan, 2010; Zengin and Çaktı, 2012; Karimzadeh et al., 2018; Infantino et al., 2020; Özmen et al., 2020; Yenihayat, 2022; Süleyman and Çaktı, 2024; Yenihayat et al., 2024).

1.3. Development of a Hybrid Dataset

To address the lack of strong-motion recordings from medium-to-large earthquakes in the Istanbul–Marmara region, we constructed a hybrid dataset. This involved merging observational data with validated broadband synthetic simulations. The simulated records, generated using stochastic and deterministic physics-based approaches, were rigorously validated against real recordings to ensure physical consistency.

Integrating both data sources allows the final database to span a wider magnitude–distance range than observations alone. This hybrid dataset is crucial for the GMPE development in this study, enabling reliable modeling for both well-recorded moderate events and rare, critical large-magnitude scenarios. Furthermore, the size of this dataset provides sufficient data to split it into test and training subsets in the next step, ensuring reliable model development.

1.4. Ground Motion Prediction Equation Development

In this study we develop GMPEs tailored to Istanbul, using a unified framework that couples high-quality regional recordings with broadband synthetic simulations representative of Marmara sources and path/site conditions. Our approach calibrates magnitude–distance scaling and nonlinear site amplification to local geology (via V_{S30}). We also benchmark our Istanbul-specific models against widely used global and regional equations to understand and identify regional adjustments that materially improve fit for the Marmara region.

Contemporary GMPEs balance physical parameters (magnitude scaling, geometric and anelastic attenuation, hanging-wall and basin terms, and nonlinear site amplification) with increasingly rich strong-motion datasets. Within this family, the NGA-West models—

Campbell and Bozorgnia (2008), Chiou and Youngs (2008), and Boore and Atkinson (2008)—set early benchmarks for magnitude–distance scaling and site nonlinearity using large Californian and global datasets. Their subsequent updates (e.g., Boore et al., 2014) refined period-dependent attenuation, V_{S30}-based site terms, and aleatory variability partitioning, and they remain widely adopted as "global" reference models against which regional equations are compared and weighted.

Parallel to these global developments, regionalized European–Mediterranean and Turkey-inclusive GMPEs have expanded both data coverage and epistemic diversity relevant to the Marmara region. Akkar and Çağnan (2010) developed equations tailored to Europe–Middle East datasets that include extensive recordings from western Türkiye (including Marmara), improving near-fault and moderate-to-large magnitude scaling over earlier local models. Building on a substantially enlarged database and improved metadata curation, Akkar et al. (2014) provided new pan-regional models (commonly used with RESORCE/ESM datasets) with explicit period-dependent heteroscedasticity and site nonlinearity; these also include Turkish recordings from Marmara and the western Anatolian extensional domain, strengthening transferability to Istanbul-centric applications. Complementing these, Kotha et al. (2020) proposed a European GMPE family with robust random-effects treatment, regionalized anelastic attenuation, and carefully regularized site terms; their calibrated dataset covers western Türkiye, offering an additional, modern alternative for logic-tree weighting in Marmara hazard studies.

Turkish ground-motion modeling has a longer lineage. Özbey et al. (2004) produced one of the early regional GMPEs using strong motions from northwestern Türkiye, providing period-wise coefficients that, despite smaller sample sizes by today's standards, remain instructive for regional attenuation and site amplification tendencies. Akkar and Bommer (2010) offered a systematic regionalization and comparison framework for European/Mediterranean ground-motion models, highlighting data-driven differences pertinent to western Türkiye and guiding selection/weighting for site-specific studies in and around Marmara. More recently, Kale et al. (2015) and Sandıkkaya et al. (2023) advanced Turkey-relevant modeling with updates to magnitude scaling, distance metrics, and nonlinear site terms; both incorporate recordings from western Türkiye (Marmara included)

and emphasize compatibility with station metadata (such as, V_{S30}), thereby improving applicability to Istanbul's diverse site conditions.

An equally important component of performance-based assessment is the spatial correlation of ground motion, which governs footprint-scale loss aggregation. While the GMPEs above provide median and dispersion at a site, spatial correlation models describe how within-event residuals co-vary across sites. Empirically, these correlations depend on period, separation distance, and path/regional effects; they also interact with the site-to-site structure implied by GMPE nonlinear amplification. In this dissertation, we adopt residual definitions consistent with the GMPE developed particularly for Istanbul, and we calibrate distance-decay of residuals using an observed Marmara-inclusive dataset alongside synthetic broadband simulations representative of Istanbul's source–path–site configurations.

1.5. Spatial Correlation Model Development

In addition to GMPE development, this study incorporates a detailed spatial correlation analysis to examine the statistical relationships between ground motion observations at different sites. By analyzing residuals between observed and predicted ground motions, a regional spatial correlation model was developed. This model provides insights into how ground motion intensities are interrelated across observation locations, offering a deeper understanding of spatial variability. The findings from this analysis contribute to enhancing the accuracy of GMPEs and refining regional seismic hazard assessments.

Spatial correlation models quantify how within-event ground-motion residuals co-vary across sites as a function of separation distance and period. These correlations control the footprint of shaking from a single earthquake and, therefore, the clustering of losses in portfolio risk. A widely used benchmark is the Jayaram and Baker (2009, 2010) models, which developed period-dependent correlation relationships for residuals (PGA and RotD50 PSA) and showed that short-period intensity measures (IM) exhibit stronger short-range correlation (larger nugget, shorter range) while longer-period ordinates decorrelate more slowly with distance. Their work also emphasized that the shape of the correlation function—and hence the spatial clustering of damage—depends strongly on the IM and spectral period selected for analysis (Jayaram and Baker, 2009; Jayaram and Baker, 2010).

Building on this, Loth and Baker (2013) extended the framework to treat cross-correlation between different IMs/periods, enabling consistent multivariate simulations of spatial fields used in regional loss studies (Loth and Baker, 2013).

Regional data sets revealed meaningful geographic variability. Using Canadian and Japanese networks, Goda and Atkinson (2010) showed that correlation length scales can differ by region and tectonic context, with implications for portfolio aggregation and for the transferability of models across regions (Goda and Atkinson, 2010). For European data, Esposito and Iervolino (2012) provided period-dependent correlation models consistent derived from Italian and European datasets, showing that correlation length tends to increase with period (Esposito and Iervolino, 2012).

We built the spatial correlation model exclusively from the observed ground-motion records. After screening the database to retain reliable mainshock recordings, we first calibrated a baseline prediction model to account for magnitude, distance, and site effects. Using that as a reference, we calculated residuals at each station. We measured station separation distances and summarized how the residual differences changed with distance by constructing empirical semivariograms. These semivariograms were then combined to obtain a stable regional picture of spatial dependence, and a smooth correlation curve was fitted to the pooled results to characterize how similarity between sites diminishes with increasing separation.

2. REGIONAL SEISMOTECTONIC FRAMEWORK

The North Anatolian Fault (NAF) is widely recognized as one of the most prominent right-lateral strike-slip faults in the world, stretching approximately 1200 km between the Anatolian and Eurasian plates (Şengör et al., 2005; Bohnhoff et al., 2013). In the Marmara Region, the NAF splays into several distinct fault segments beneath the Sea of Marmara, forming a series of pull-apart basins and structural complexities that bear on both seismic hazard and tectonic evolution (Armijo et al., 2002; Yaltırak, 2002; Pondard et al., 2007). Notably, the Marmara fault segments, estimated to be around 100 km in total length (Bohnhoff, 2013; Ergintav et al., 2014), lie in a seismic gap where the fault has not ruptured in a major earthquake for centuries despite the energetic twentieth-century NAF ruptures to the east.

Following the devastating earthquakes of August 17, 1999 (M_W 7.4 Kocaeli) and November 12, 1999 (M_W 7.2 Düzce), the deep crustal structure of the Marmara region became the subject of extensive research. For instance, within the framework of the French-Turkish research program SEISMARMARA (Hirn et al., 2001), data on the NAF beneath the Sea of Marmara were collected, contributing to studies on the seismic risk in Istanbul and the Marmara Region. Various research teams (Karabulut et al., 2003; Bécel et al., 2009; Bécel et al., 2010; Polat et al., 2016; Tarancıoğlu et al., 2020) have examined the deep crustal structure along with the tectonic and geological features of the Marmara region.

Historical and paleoseismic records reinforce the peril inherent in this seismic gap. Ambraseys (2002) reports a 150–400-year recurrence interval for large earthquakes in the Marmara Region, referencing catastrophic events, including the 1766 earthquake, that significantly impacted Istanbul and nearby settlements. Similarly, Drab et al. (2015) identified four major earthquake sequences between C.E. 740 and 1999, highlighting how the Çınarcık segment functioned as a “permanent seismic barrier.” Their findings underscore the propensity for multiple, sequential ruptures along the NAF, although large, throughgoing ruptures remain relatively rare—only once did a rupture successfully propagate through the

bend between the Çınarcık segment and the western portion of the İzmit segment in a single event.

Contemporary geodetic and seismological studies confirm that the unbroken Marmara fault segment remains loaded and capable of generating a large earthquake (Parsons, 2004). Ergintav et al. (2014) and Lange et al. (2019) both conclude that the locked segment beneath the Sea of Marmara could produce an event of moment magnitude $M_W \geq 7$. Coupled with modeling efforts by Murru et al. (2016), the probability of an $M_W \geq 7.3$ earthquake along this segment in the next 30 years may range from 35% to as high as 47%, casting an ominous outlook for densely populated urban centers around the Marmara coast.

Structural evidence, derived from multi-channel seismic reflection surveys, marine geophysics, and GPS campaigns, reveals a network of step-overs, subsiding basins, and bend-related normal faults (Armijo et al., 1999; Yaltırak, 2002; Le Pichon et al., 2003). Indeed, active pull-apart basins such as Çınarcık, Tekirdağ, and Central Basins reflect the ongoing interplay of strike-slip motion and localized extension (Barka, 1997; Pondard et al., 2007). These structural complexities shape the region's seismicity distribution and underscore how smaller segments may act as barriers or, conversely, may become enablers of multi-segment ruptures under certain stress conditions.

Ultimately, the intricate seismotectonic framework of the Marmara Region provides a natural laboratory for earthquake research, and it underscores the need for detailed studies of fault kinematics, rupture scenarios, and ground-motion modeling (Bohnhoff, 2013; Lange et al., 2019). The hazard implications for Istanbul—Turkey's economic and cultural hub—are profound, particularly as geologic history and modern GPS data converge on the likelihood of a major, imminent event.

3. DATASET COMPILATION AND DATA PROCESSING

This section describes the procedure of compilation and unification of disparate earthquake recording catalogs from AFAD and KOERI (VDC, 2024; AFAD 2025; ESM, 2025; IERREWS, 2025) databases. This process involved steps such as compiling station metadata, computing moment magnitudes for certain events, assigning site information (e.g., V_{S30}) where needed, merging waveform recordings from multiple sources, and standardizing the recordings within the same compilation database. The further step includes processing these recordings (including baseline correction, bandpass filtering, and signal-to-noise ratio assessment). The dataset is limited to $R_{hyp} \leq 200$ km, $M_W \geq 4.0$, primarily serving engineering needs. The outcome of this multi-stage workflow is a unified database containing not only event and recording information but also processed ground motion time series that are ready for further analyses.

3.1. Compilation and Unification of Earthquake Recording Catalogs

A primary step involved merging multiple earthquake recording catalogs. These catalogs cover recordings of two major networks of Turkey, two earthquake databases from KOERI, namely, Regional Earthquake-Tsunami Monitoring Center - RETMC (VDC, 2024; ESM, 2025) and Istanbul Earthquake Rapid Response and Early Warning System - IERREWS (2025), and AFAD (2025). This step was particularly challenging and time-consuming, due to the different data types and formats used in these databases. Therefore, this data needed to be standardized before moving forward to the next steps. Several procedures were applied, such as choosing among slight difference between earthquake information (as date/time, latitude, longitude, depth and magnitude) and, sometimes calculating moment magnitude, when only other magnitude estimates were available. All three components of ground-motion traces were kept - the north–south (N), east–west (E), and vertical (Z) components.

3.1.1. Station Data

Station coordinates (latitude and longitude), local station codes, V_{S30} values, and other relevant site descriptors were all included in the metadata file. In certain cases, multiple codes exist for the same station, due to the changes over time. However, the most recent code was considered.

Shear-wave velocity in the top 30 meters (V_{S30}) is a key site parameter. Particularly, at most AFAD stations V_{S30} values exist, while most stations of the two other networks don't have any V_{S30} values assigned. Whenever station-specific V_{S30} values were unavailable, geospatial interpolation was used. V_{S30} map of Istanbul by IMM (2007, 2009) was the primary source to match and interpolate each station's coordinates, yielding a station-specific V_{S30}. For the stations outside Istanbul metropolitan area, the MTA (2004) maps were used to assign V_{S30} values.

3.1.2. Earthquake Data

3.1.2.1. Earthquake Information. The following information was primarily gathered from the KOERI database, AFAD database was used as a secondary source when any earthquake data was missing.

(i). Event Time and Source. Date and time of the recorded ground motion and identification of the catalog or agency from which the event originated.

(ii). Epicentral Information. Each ground motion event's latitude, longitude and depth were retrieved.

(iii). Distances. A hypocentral distance was computed for each station–event pair, using

$$R_{hyp} = \sqrt{\left(\Delta_{epi} \times 111.32\right)^2 + h^2}\,, \tag{3.1}$$

where Δ_{epi} is the great-circle distance (in degrees) between station and epicenter, converted to kilometers (1°≈111.32 km), then combined with the focal depth.

(iv). Magnitudes. Moment magnitudes of the events were assigned from the KOERI or AFAD databases. If an event did not have an M_W record but did have local magnitude (M_L) or duration magnitude (M_D), the missing M_W was derived through published

empirical relationships. Where events were missing M_W but contained alternative magnitudes, two linear relationships (adapted from Kadirioğlu and Kartal, 2016) were applied as

$$M_w = 0.951M_D + 0.5862, \quad (3.2)$$

$$M_w = 1.0292M_L + 0.2269. \quad (3.3)$$

Hence, each event was consistently assigned a representative M_W.

3.1.3. Initial Dataset Compilation

2984 three-component recordings ranging from M_W 4 to M_W 7.4 at 171 stations, within 200 km of epicentral distance were compiled and unified under a single metadata file. While most of these stations are located within Istanbul, many stations from the neighboring region are also utilized (Figure 3.1).

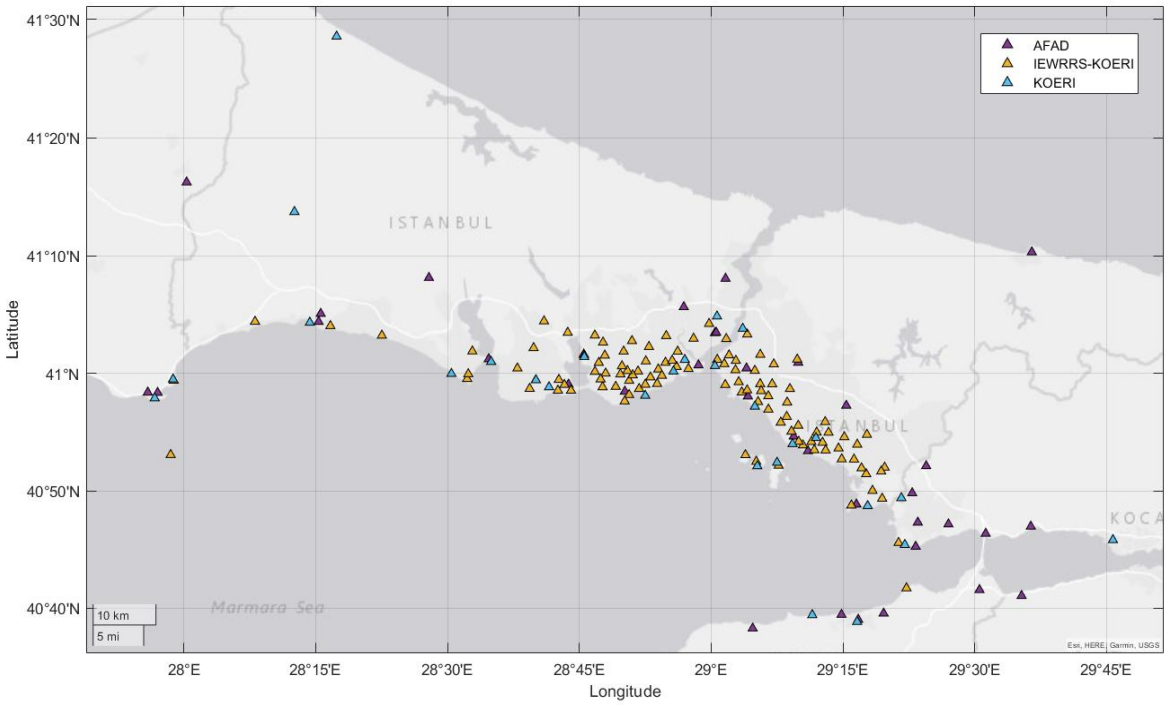

Figure 3.1. Geographical distribution of recording stations in the study region.

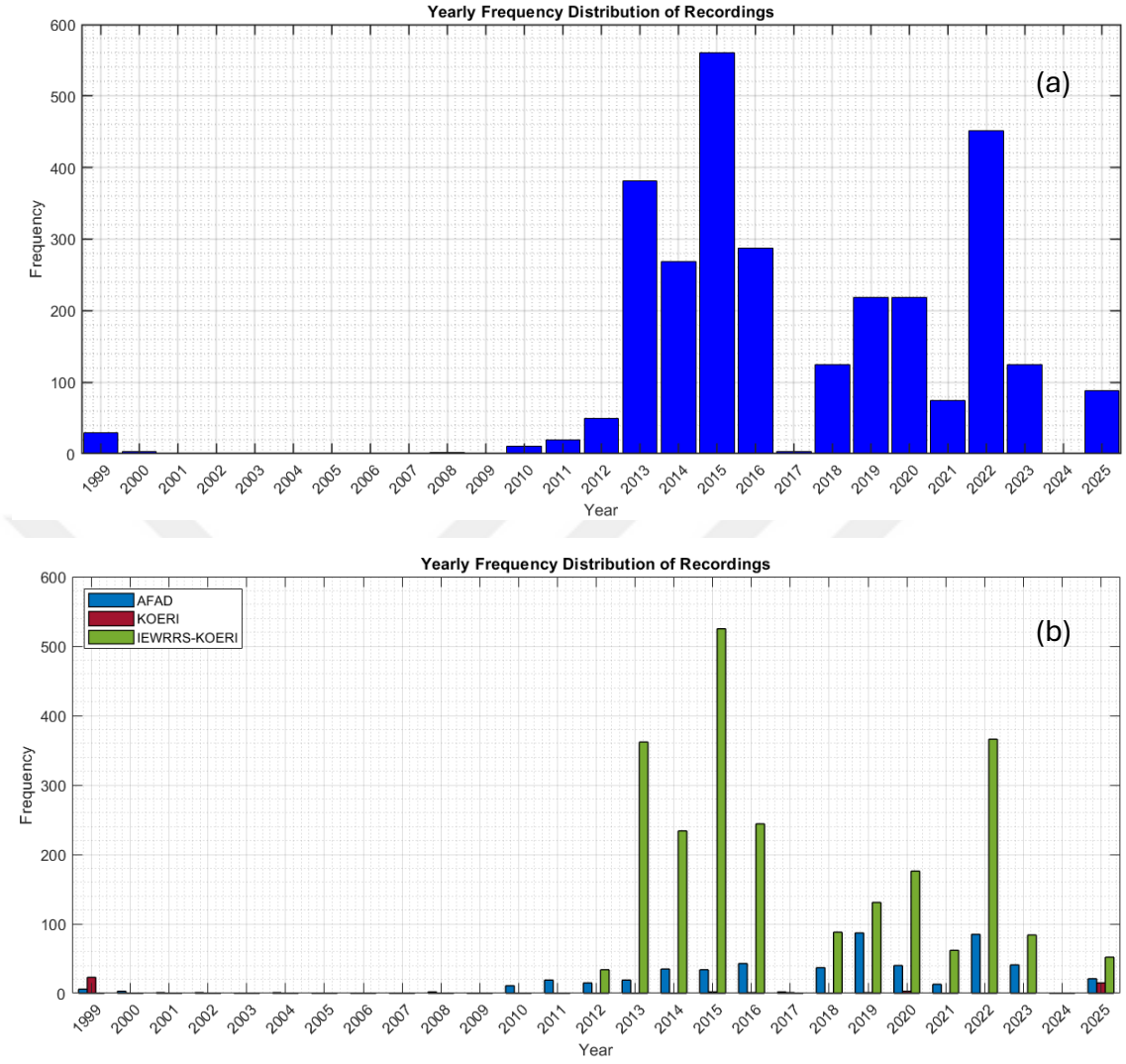

Figure 3.2. (a) Total number of recordings annually; (b) Total number of recordings annually, categorized by network.

The recordings included in this dataset cover the years 1999 to 2025. Most of the recordings in this dataset belong to the IERREWS network. The annual distribution of the total number of recordings, based on station networks can be seen in Figure 3.2. Similarly, Figure 3.3 shows the annual distribution of the total number of recordings based on V_{S30} bins.

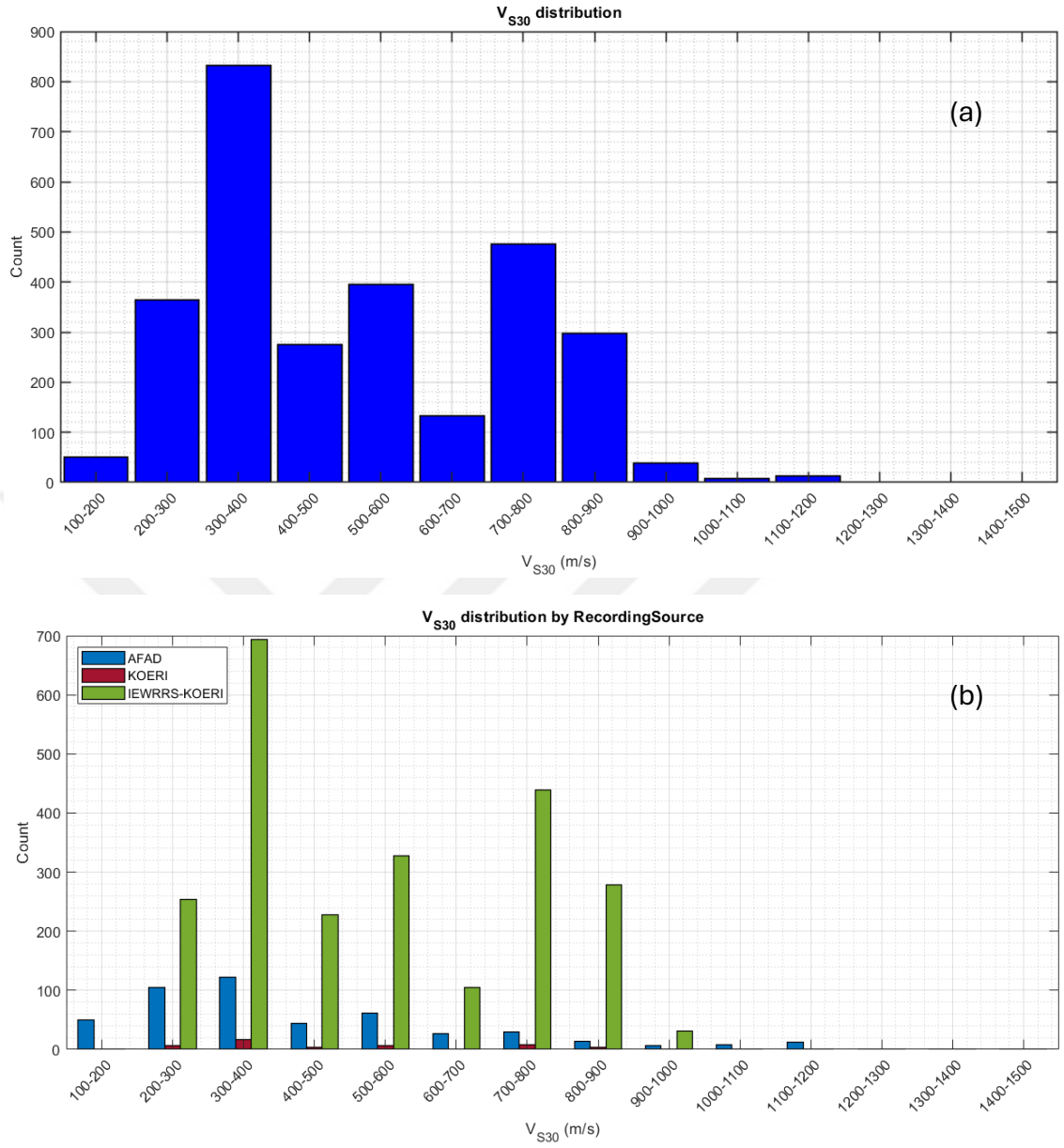

Figure 3.3. (a) Total number of recordings based on V_{S30} bins; (b) Total number of recordings based on V_{S30} bins, categorized by network.

Figure 3.4 shows the distribution of the recordings in terms of moment magnitude and hypocentral distance. The vast majority of the data is stacked between M_W 4 - M_W 5. The distribution is much sparser above M_W 5 and there is no recorded data between M_W 6.2 - M_W 7.1 in the stations used in this study.

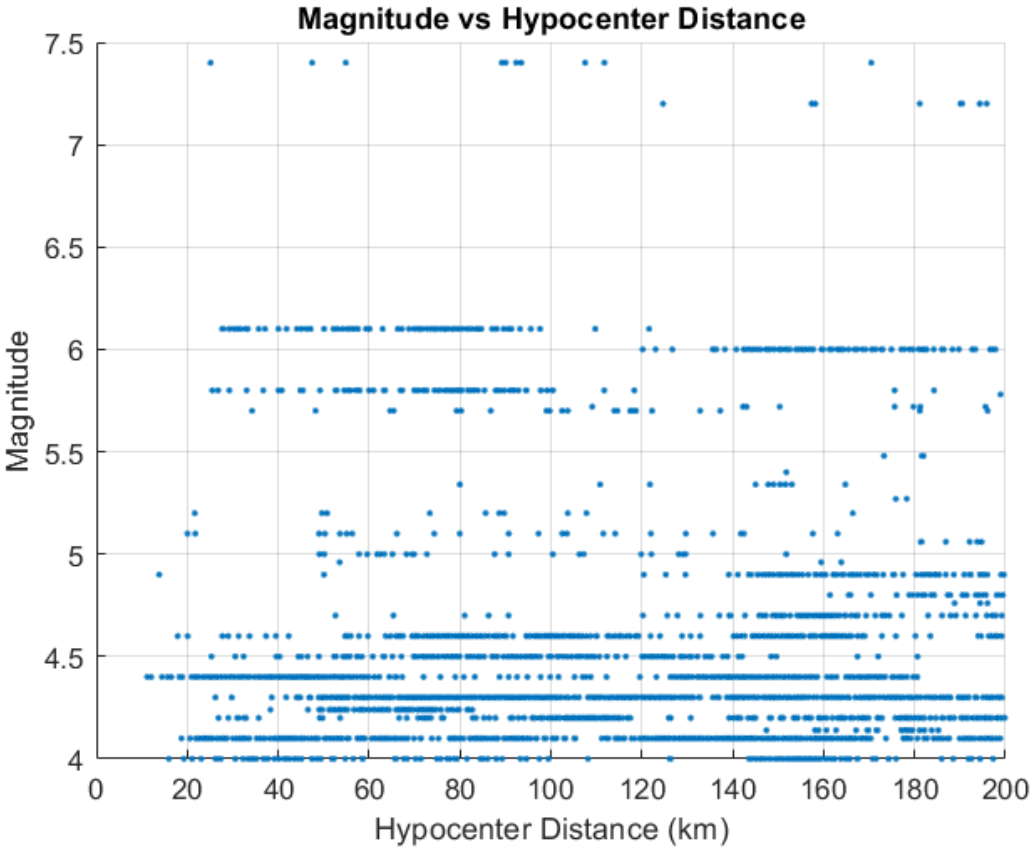

Figure 3.4. Distribution of the recordings, considering magnitude and hypocentral distance.

3.2. Data Processing

3.2.1. Baseline Correction and Bandpass Filtering

All waveforms underwent baseline adjustment to remove offsets, followed by a bidirectional bandpass filter (Butterworth, 1930) within a chosen frequency interval of typically 0.2–30 Hz. Symbolically, the bandpass filter can be represented as

$$H(\omega) = \frac{\omega^{2N_f}}{\left(\omega^{2N_f} + \omega_1^{2N_f}\right) \cdot \left(\omega_h^{2N_f} + \omega^{2N_f}\right)}, \tag{3.4}$$

where ω_l and ω_h are the low- and high-corner frequencies, and N_f is the filter order. This step suppresses both low-frequency drifts and high-frequency noise.

3.2.2. Onset Identification and the Duration of Ground Motion

3.2.2.1. Picking of P- and S-Wave Onsets. Next, the start times of the P-wave (t_p) and S-wave (t_s) phases were identified. Initially, an automated picker provided approximate onsets, after which manual validation or refinement was conducted. Where manual adjustments were deemed necessary, we zoomed into specific time intervals of the waveform to mark more precise arrival times.

3.2.2.2. Arias Intensity Computation. To define an energy-based window, Arias intensity integrals were computed following a typical approach (Arias, 1970) as

$$I_A(t) = \frac{\pi}{2g} \int_0^t a^2(\tau)\ dt, \tag{3.5}$$

where $a(\tau)$ is the acceleration time series, and g is gravitational acceleration. The time required to reach 95% of the total Arias intensity, denoted as t_{95}, helps constrain signal duration and guide the end of the window considered for certain analyses.

3.2.3. Elimination of Low-Quality or Non-Representative Traces

Even after initial filtering, some traces were deemed unsuitable upon visual inspection, due to extreme noise contamination or truncation. Such traces were flagged for elimination. Additional criteria included ensuring that baseline corrections were not overly disruptive to the waveform shape. Aftershock events were also flagged to avoid them from the main dataset, to maintain consistency in mainshock-based analyses.

3.2.4. Computation of Ground-Motion Parameters

3.2.4.1. Peak Ground Motion Values. From the processed horizontal components, the average horizontal PGA and PGV were determined. PGA is simply

$$PGA = max\,|a(t)|\,, \tag{3.6}$$

where a(t) is the acceleration time series. PGV is the peak of the time-integrated velocity trace. Similar computations were performed to store the vertical component.

3.2.4.2. Pseudo Spectral Acceleration and Rotation-Based Metrics. For engineering applications, 5% damped PSA was computed across a wide range of oscillator periods (e.g., 0.02–5.0 s) using response spectrum analyses. Specifically, each pair of horizontal components (E and N) was rotated by small increments between 0–180° to produce RotD50 parameter (Boore, 2010) - the median (50th percentile) of the spectral amplitudes across all rotations.

Formally, if $\mathbf{a_E}(t)$ and $\mathbf{a_N}(t)$ are the two orthogonal horizontal accelerations, the rotated signal at angle θ is

$$\mathbf{a}_\theta(t) = \mathbf{a_E}(t)\cos(\theta) + \mathbf{a_N}(t)\sin(\theta). \quad (3.7)$$

A separate response spectrum is computed for each θ, and the RotD50 values at each period are taken thereafter.

3.2.5. Signal-to-Noise Ratio Evaluation

For quality assurance, a signal-to-noise ratio (SNR) check was performed by comparing the frequency-domain amplitude of the S-wave portion against that of a preceding noise window:

(i). Noise Window Selection. A window prior to P-wave onset was chosen (often 1–2 seconds before the onset) and constrained by the estimated coda end times to ensure that the duration matched the main S-wave window length.

(ii). Fourier Amplitude Calculations. Fourier transforms of both signal and noise windows were obtained, and the average or integrated magnitudes were used to determine SNR.

(iii). Thresholding. Recordings with SNR below a chosen benchmark were flagged or excluded from final usage.

3.2.6. Final Outputs and Data Preservation

The resulting integrated database was arranged as a comprehensive table of ground motions with:

(i). Event Information: Unified origin time, magnitude (M_W), magnitude source, epicentral coordinates, focal depth, mainshock/aftershock flags.

(ii). Station Metadata: Station codes, coordinates, assigned V_{S30} values, V_{S30} source, and other site descriptors.

(iii). Waveform Data: Waveform source, raw, filtered and baseline-corrected traces for the E, N, and Z components, t_p and t_s picks, hypocentral distances, and sampling rates.

(iv). Derived Parameters: PGA, PGV, Arias intensity durations as ground motion durations, RotD50 spectral values.

This unified resource then becomes the foundation for subsequent quantitative analyses, such as ground-motion model development.

4. GROUND MOTION SIMULATIONS

4.1. Ground Motion Simulation Efforts for the Marmara Region

Several studies have been conducted over the past two decades, attempting to improve our understanding of the potential hazard of large magnitude earthquakes in the region of Marmara. Even though they involve different techniques for simulating ground motions, they serve the same hazard modeling purpose for Istanbul and the nearby region.

Infantino et al. (2020) present 3D physics-based numerical simulations (PBSs) for a series of earthquake scenarios (M_W ranging from 7.0 to 7.4) along the Marmara segment of the NAF, offshore Istanbul. The authors detail the construction and validation of their 3D velocity model, source characterization, and simulation approach. Their findings demonstrate that for magnitude 7.0 – 7.2 events, the physics-based simulations align well with established empirical ground motion prediction models, but for M_W 7.4 scenarios, directivity effects significantly amplify ground motion estimates. Zengin and Çaktı (2012) present a stochastic finite-fault simulation approach for various fault-rupture scenarios in Istanbul. They generate site-specific ground motions for the M_L 5.1 2011 earthquake, using systematically calibrated source, path, and site model parameters. By integrating historical damage data and modern stochastic finite-fault simulations, Yenihayat (2022) conducted simulations for the 1509, 1766, and 1894 Istanbul earthquakes. Correlating synthetic ground-motion intensities with documented damage distributions thus offers a detailed view of the most plausible seismic scenarios for these historical events. Yenihayat et al. (2024) perform stochastic finite-fault simulations for the M_W 5.8 Silivri earthquake, addressing the need to understand high-frequency ground motions in the Istanbul region. Their best-fit model parameters not only reproduce observed ground-motion amplitudes and frequency content but also align with PGA estimates from NGA-West2 ground-motion models. Süleyman and Çaktı (2024) stochastically simulated ground motions for several large-magnitude earthquake scenarios along the central Marmara and Princes' Islands segments of the NAF. They analyzed the estimations at the Büyükçekmece district of Istanbul and discussed the uncertainties associated with hypocenter location and stress parameters.

Alongside the M_W 7.4 Marmara earthquake of 1999, the M_W 7.2 Düzce earthquake of 1999 was also a particular focus of the researchers for many years, due to the hazardous characteristics. Uğurhan and Askan (2010) stochastically simulate near-field ground motions for this earthquake, applying a dynamic corner frequency approach within the EXSIM algorithm. Karimzadeh et al. (2018) evaluate the applicability of stochastically simulated ground motions in structural and earthquake engineering by comparing them to observed data from the M_W 7.2 Düzce earthquake of 1999. Focusing on this earthquake, Özmen et al. (2020) propose a hybrid simulation methodology combining a low-frequency deterministic approach (using discrete wavenumber finite element modeling) and a high-frequency stochastic method for generating broadband ground motions of the 1999 Düzce earthquake.

4.2. Stochastic Finite-Fault Ground Motion Modelling Algorithm, EXSIM

EXSIM is a finite-fault stochastic ground motion simulation algorithm capable of generating synthetic waveforms of strong ground motions (Motazedian and Atkinson, 2005; Boore, 2009). This algorithm accounts for finite-fault effects by incorporating rupture slip models, rupture dimensions, and fault geometry. The finite-fault modeling structure in EXSIM are constructed as an array of subsources, each assumed to be a point source with different slip values. The concept of combining subfaults to create a finite-fault model is based on the Stochastic Method SIMulation (SMSIM) algorithm (Boore, 2003; Boore, 2005), which is only capable of simulating point sources. The point-source approach for shear radiation was fundamentally developed by Brune (1970, 1971). This method uses the stress parameter and seismic moment to produce the theoretical Fourier amplitude spectrum at the seismic source, attenuated by an empirical model in the frequency domain. In EXSIM, the waveforms generated for each subsource are combined to create the final synthetic waveform of an earthquake.

Multiple versions of EXSIM have been developed over the years (Beresnev and Atkinson, 1997; Motazedian and Atkinson, 2005; Assatourians and Atkinson, 2007; Boore, 2009). Significant improvements include a more effective treatment of low frequencies proposed by Boore (2009), and further refinement by Assatourians and Atkinson (2007), who enhanced the algorithm's capability to model finite faults with complex slip distributions.

In point-source simulations, it is assumed that seismic energy is radiated from a single point. The SMSIM algorithm of Boore (2005) performs this simulation through the following steps:

- Generation of White Noise: A normally distributed random noise signal with zero mean is generated to represent the stochastic nature of seismic wave propagation.
- Windowing: This noise signal is multiplied by a window function of predefined duration, such as a boxcar or tapered window, to confine the signal in time and simulate the finite duration of seismic energy release.
- Fourier Transform: The Fourier transform of the windowed signal is calculated to obtain its frequency-domain representation.
- Shaping the Amplitude Spectrum: The amplitude spectrum is shaped according to a theoretical source spectrum model, which depends on parameters like seismic moment, stress drop, and corner frequency. This step models the frequency content of the seismic source.
- Attenuation Effects: The shaped spectrum is modified to account for attenuation effects, including geometrical spreading (how seismic waves decrease in amplitude with distance), anelastic attenuation (energy loss due to the Earth's material properties, often represented by a quality factor, Q), and site amplification factors (local soil and rock conditions that can amplify seismic waves).
- Inverse Fourier Transform: The modified frequency-domain signal is transformed back into the time domain using the inverse Fourier transform, resulting in a synthetic time-history of ground motion at a specific site.

In EXSIM, this point-source approach is extended to simulate finite faults by dividing the fault plane into multiple subsources or subfaults:

- Subdivision of Fault Plane: The fault is discretized into small rectangular elements, each representing a subsource with its own seismic moment and slip.
- Time Shifting and Summation: The synthetic ground motions from each subsource are calculated using the point-source method. These individual waveforms are time-shifted to account for rupture propagation effects (such as rupture velocity and direction) and are summed to produce the final ground motion at a site.

- Incorporation of Rupture Complexity: By assigning different slip values and rupture initiation times to subsources, EXSIM can model complex rupture processes, including heterogeneous slip distributions and directivity effects.

This approach allows EXSIM to generate realistic synthetic ground motions that capture the effects of finite-fault dimensions, rupture propagation, and source complexity. The algorithm is particularly useful for seismic hazard analysis in regions lacking sufficient recorded ground motion data.

4.3. Validation of the EXSIM Algorithm for the Istanbul Region

In our study, we used the most recent version of EXSIM available (EXSIM, 2018), incorporating the latest corrections and improvements. The latest versions include bug fixes and enhancements that improve the accuracy and reliability of the simulations.

A validation study of the stochastic finite-fault ground motion simulation algorithm EXSIM was conducted by compiling parameters from research developed at both regional and global scales. Site amplifications were considered as frequency-dependent amplification factors (Margaris and Boore, 1998). Distance and site-dependent attenuation at high frequencies was measured by Süleyman and Çaktı (2018) following the approach of Anderson and Hough (1984). The model by Horasan et al. (1998) was used to define anelastic attenuation at selected central frequencies on Fourier amplitude spectra. The durations of the simulated ground motions were scaled according to the model proposed by Boore and Thompson (2014) (Table 4.1).

Ground motion records from the Istanbul Earthquake Rapid Response and Early Warning System stations for five earthquakes with magnitudes between M_W 4.0 and M_W 5.8 that occurred in the Marmara Sea (Figure 4.1) were utilized. For the M_W 5.8 2019 Silivri earthquake, a finite fault source model studied by Karabulut et al. (2021) was used (Figure 4.2). For the other earthquakes, a point source assumption was made due to the relatively small rupture dimensions of the faults. The parameters used in the validation study are summarized in Table 4.1. Some of these parameters were developed regionally, specifically

for Istanbul and the Marmara region. The bottom rows of Table 4.1 summarize the source parameters of the five earthquakes used in the validation.

Table 4.1. Input parameters used in the stochastic simulations.

Parameters	**Values**		**References**
Crustal density (ρ, g/cm^3)	2.7		
Average S-wave velocity (km/s)	3.4		
Anelastic attenuation model for S-waves	$Q_s(f) = 50\ f^{1.09}$		Horasan et al. (1998)
S-wave duration model	**R_{rup} (km)**	**D_p (s)**	Boore and Thompson (2014)
	0	0	
	7	2.4	
	45	8.4	
	125	10.9	
	175	17.4	
	270	34.2	
	Slope of the last segment	0.156	
Geometrical spreading model	**R (km)**	**Coefficients**	Akıncı et al. (2013)
	0–20	1	
	20–40	0.8	
	40–100	0.7	
	>100	0.5	
Site kappa model (κ_0)	V_{S30}-dependent functional form × 1.5		Süleyman and Çaktı (2018)
Site amplification model	Site-class specific generic amplification coefficients		Margaris and Boore (1998)

Source Parameters					
Magnitude (M_W)	Stress Drop, Δσ (Bars)	Fault Type	Length (km)	Width (km)	Sub-fault size (km)
5.8	60	Strike-slip	20	5.5	0.8 × 0.5
4.6	15	Strike-slip	1	1	1 × 1
4.5	25	Strike-slip	1	1	1 × 1
4.3	70	Strike-slip	1	1	1 × 1
4.0	90	Strike-slip	1	1	1 × 1

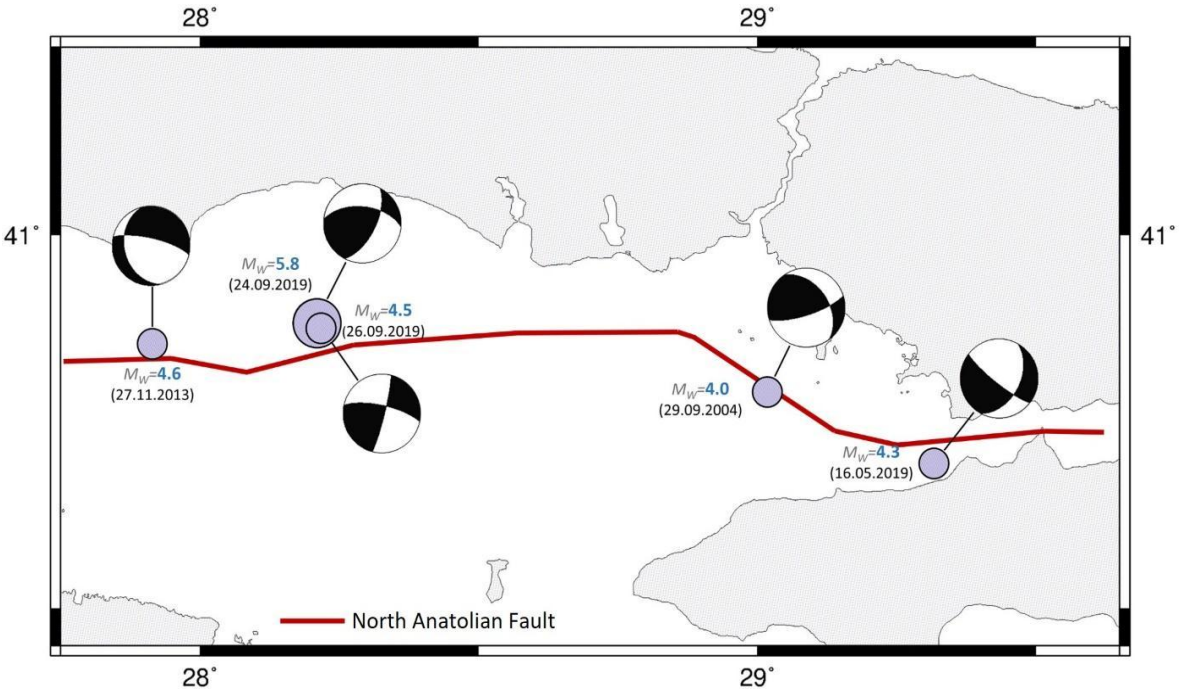

Figure 4.1. Epicentral locations, magnitudes and occurrence dates of the five earthquakes considered in the validation study.

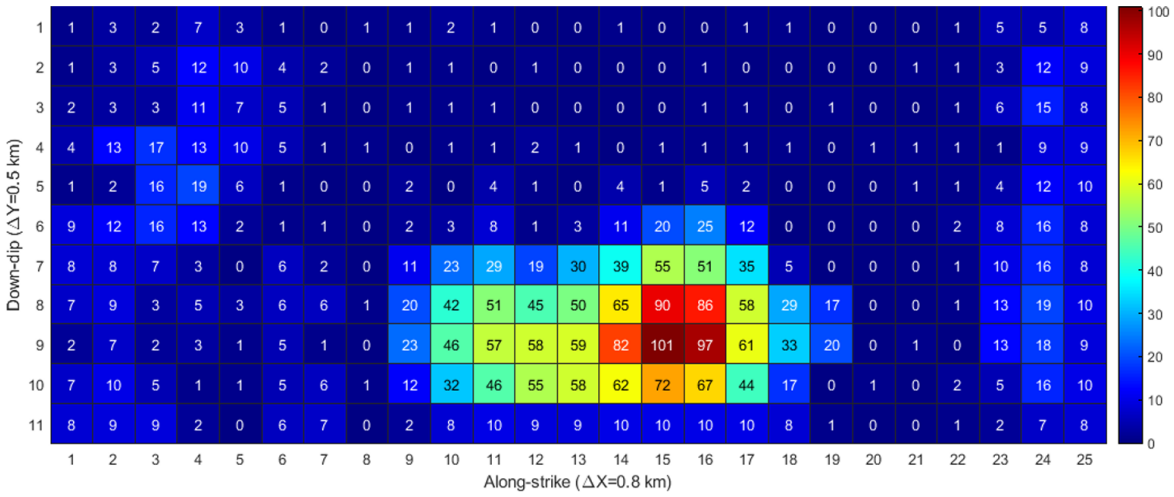

Figure 4.2. Finite-fault slip model developed in Karabulut et al. (2021) for M_W 5.8 Silivri earthquake; the values in grid cells show the variations in slip values, measured in cm.

The validation study was carried out by generating synthetic records and then comparing them with the observed records in both time and frequency domains (Figure 4.3). In the time domain, the consistency between PGA and S-wave record durations was

evaluated; in most comparisons, agreement was observed by these criteria. In the frequency domain, the agreement across amplitudes was examined, and better consistency was observed at frequencies of 1.5 Hz and above. These observations were further supported in subsequent stages by numerical analyses. Records from over a hundred earthquake recording stations were utilized. Additionally, distance and site effects were considered in comparisons made against GMPE curves.

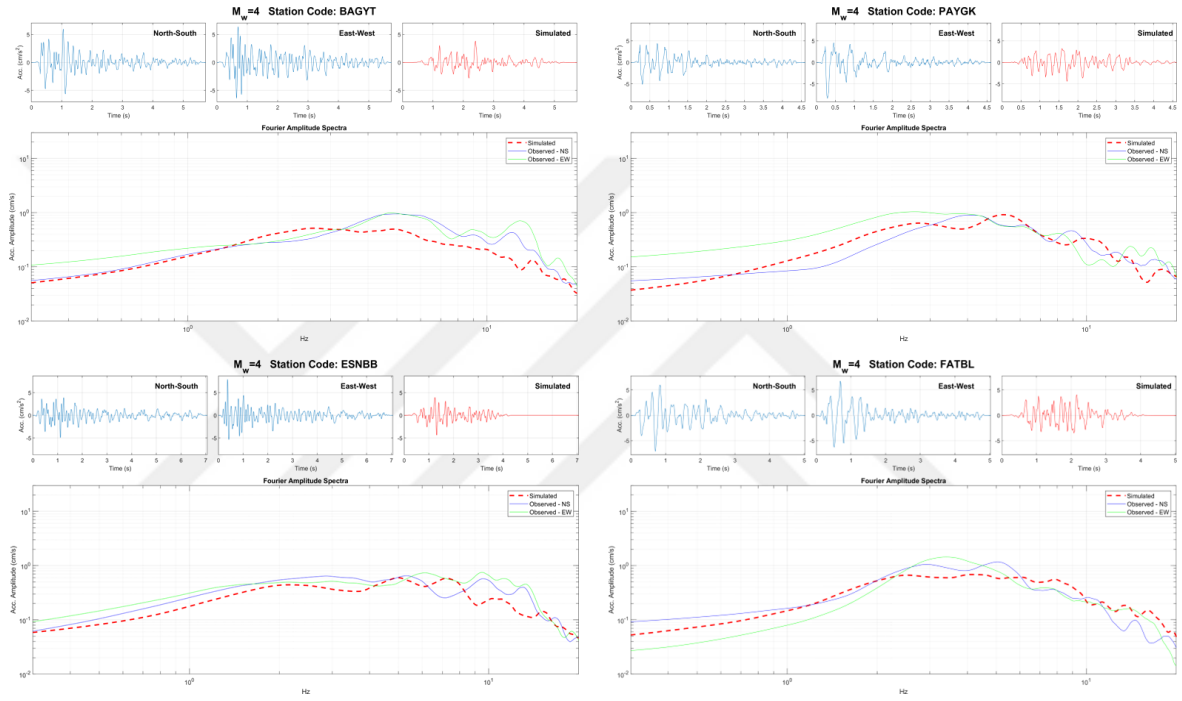

Figure 4.3. Comparison of observed and synthetic records in time and frequency domains.

In Figure 4.4, the distributions of observed and synthetic PGA and PGV with respect to hypocentral distance are presented. Here, it is seen that the synthetic values for the M_W 5.8 event are somewhat lower than the observed values. Figure 4.5 presents a similar comparison, this time directly comparing the observed and synthetic PGA and PGV values. In Figure 4.5, the diagonal line in both graphs represents the region where equality is achieved. Overall, the data are seen to be proportionally distributed around the agreement lines. However, for the M_W 5.8 earthquake, the synthetic peak ground motion values remain noticeably lower than the observed values in both the PGA and PGV graphs. This is related to the rapid attenuation of the observed ground motion values with distance for this specific earthquake, as also noted in the study by Malcıoğlu et al. (2022). For this reason, defining a

general anelastic attenuation model for such events has been one of the challenging aspects of this stage. Nevertheless, since this situation pertains to a single earthquake example, it does not adversely affect the overall results of the study.

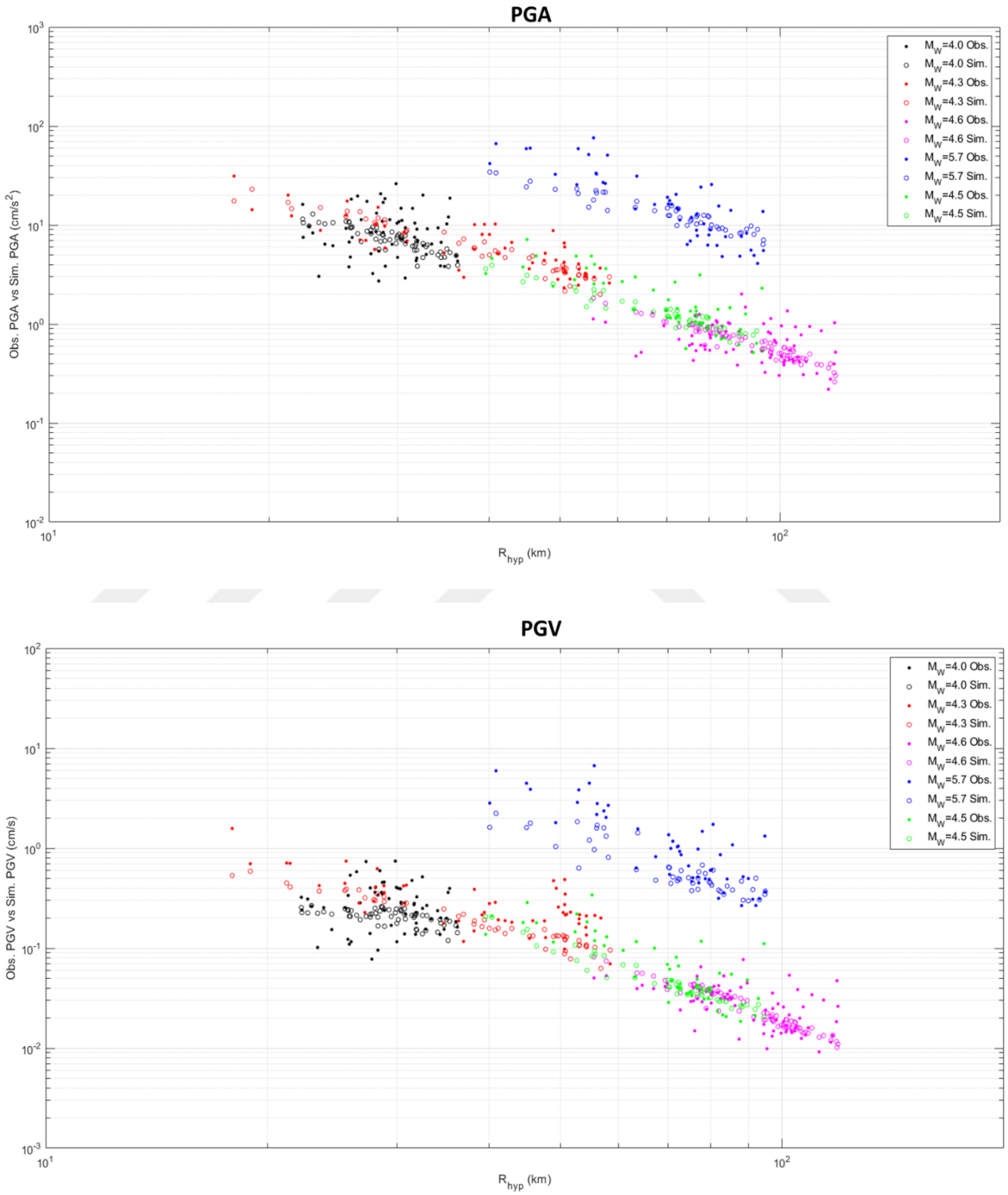

Figure 4.4. Observed versus simulated PGA and PGV values against hypocentral distance.

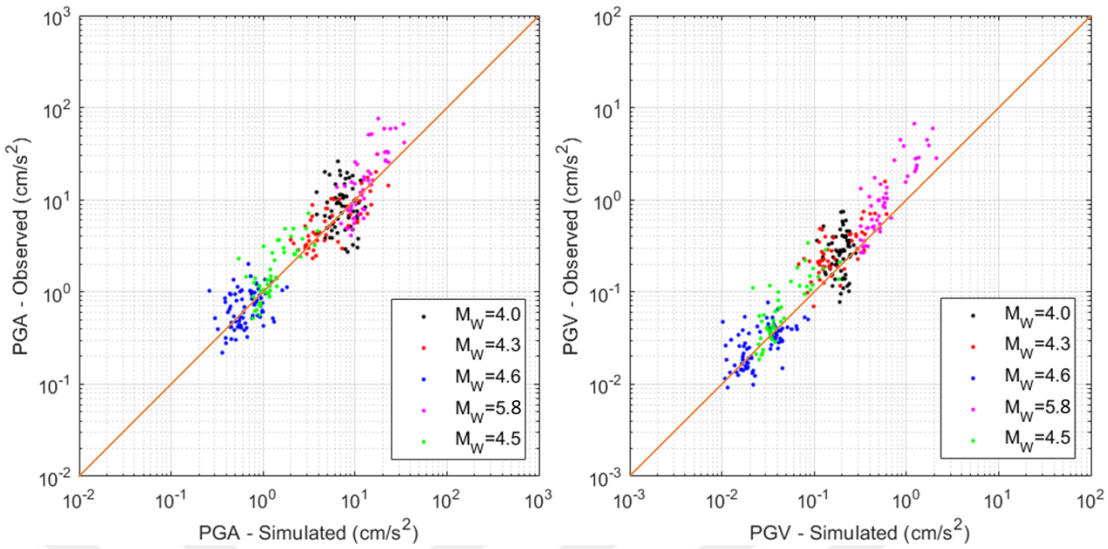

Figure 4.5. Simulated versus observed PGA and PGV comparisons.

Thorough analyses were prepared for each earthquake using PSA (Figure 4.6). Analyses measuring the difference between synthetic and observed records were conducted over the frequency range of 0.3–20 Hz. In these analyses, a relatively stable fit was observed at high frequencies around the zero line, while fluctuations were noted at low to medium frequencies. The results obtained were considered quite satisfactory.

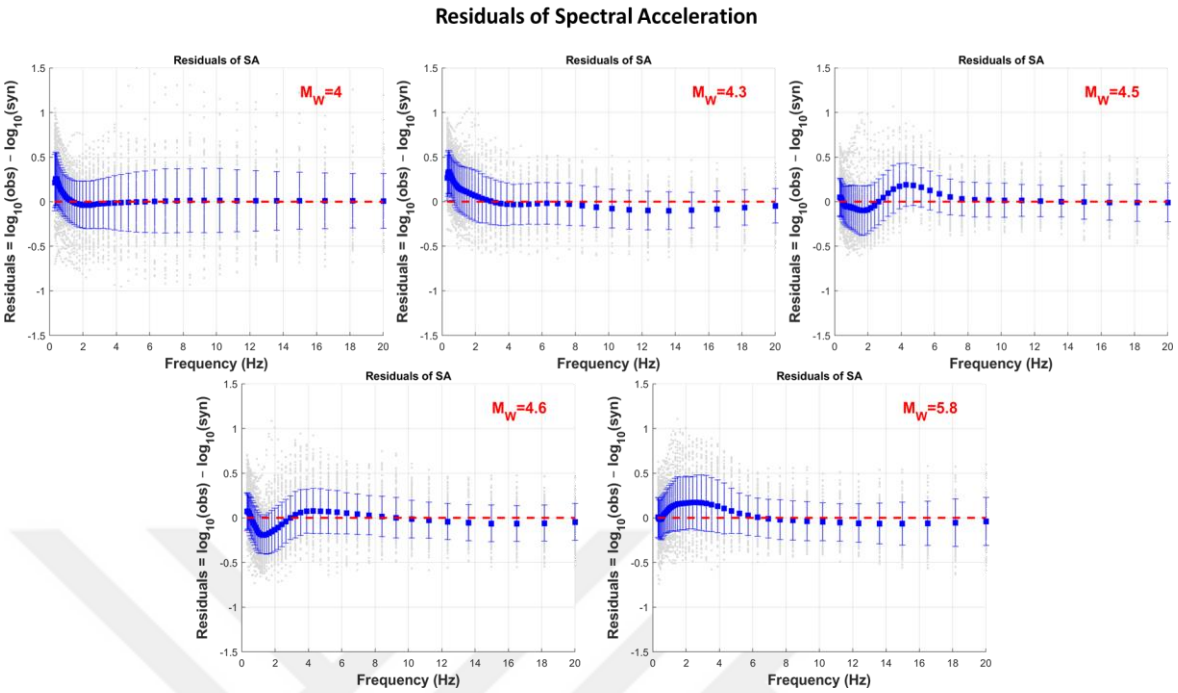

Figure 4.6. Residual analysis performed using spectral amplitudes in frequency domain.

4.4. Stochastic Ground Motion Simulations of Scenario Earthquakes

4.4.1. Testing the Validated Model

Upon the completion of the validation study, the project advanced to its second phase. In this phase, the validated algorithm was evaluated using medium to large magnitude scenario earthquakes located along the central Marmara and Princes' Islands segments of the NAF. Parameters for these scenario earthquakes were carefully developed to construct a comprehensive test scenario dataset. Specifically, several scenarios with magnitudes ranging from M_W 6.3 to 6.7 were formulated for the Princes' Islands segment, and magnitudes from M_W 7.2 to 7.4 for the central Marmara segment (Figure 4.7). Additionally, by combining certain scenarios, earthquake events with magnitudes between M_W 7.41 and M_W 7.42 were realized. The primary objective of generating this test scenario dataset was to assess the applicability of the validated algorithm and to compare the simulated ground motions with well-established GMPEs (Abrahamson et al., 2014; Boore et al., 2014).

To define the rectangular dimensions of the rupture events for these scenarios, empirical models developed by Thingbaijam et al. (2017) and Wells and Coppersmith (1994) were utilized. Based on these dimensions, random finite-fault ruptures were generated using the Rupgen (2000) algorithm. In total, 25 test scenarios were developed. For each scenario, hypocenters were randomly assigned within the designated rupture models. Defining the stress drop parameter, which must be established prior to simulations, was one of the most challenging aspects of this study. Due to the limited observations of medium to large magnitude earthquakes in the region and the inherently variable nature of this parameter, a range of stress drop values was employed to investigate its effect on ground motion estimations. Specifically, stress drop values ranged from 100 to 160 bars in 5-bar increments for scenarios with magnitudes M7 and above, and from 60 to 120 bars in 5-bar increments for scenarios below M7.

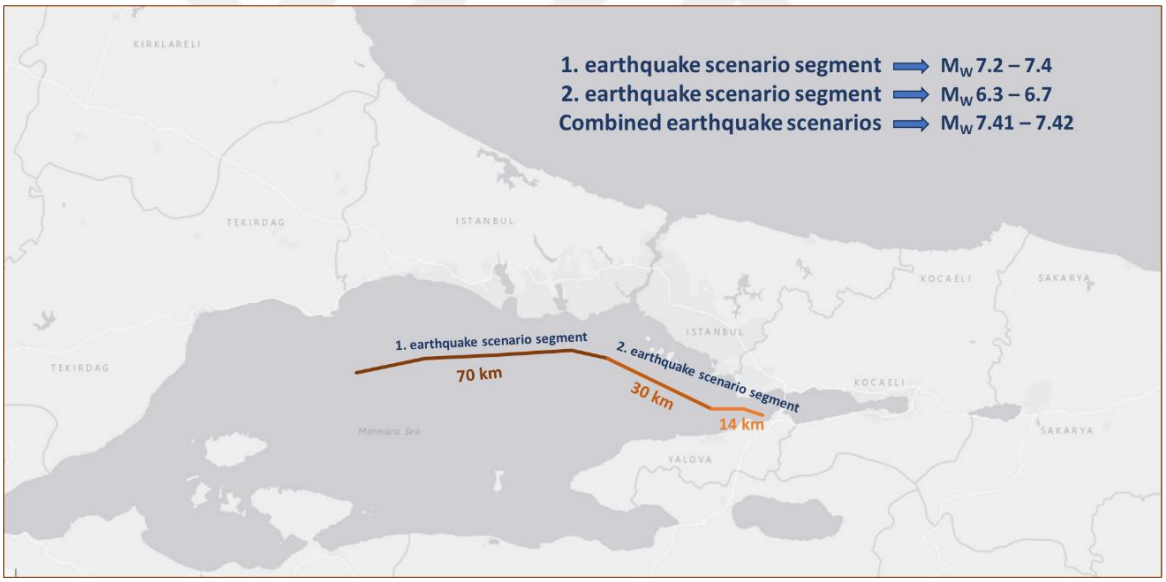

Figure 4.7. Segments considered for realizing scenario earthquakes.

The locations for the ground motion simulation observations were selected based on high-resolution V_{S30} maps previously developed for the entire Istanbul area. These maps encompass over 24,000 grid cells across Istanbul with available V_{S30} data (MTA, 2004; IMM, 2007; IMM, 2009). To optimize computational efficiency, the number of simulation observation points was reduced to 6,096. The V_{S30} values assigned to the grid cells range from 200 to 1,300 m/s, as depicted in Figure 4.8. This extensive dataset enables the

generation of simulated ground motion parameters over a wide area, facilitating detailed and comprehensive analyses.

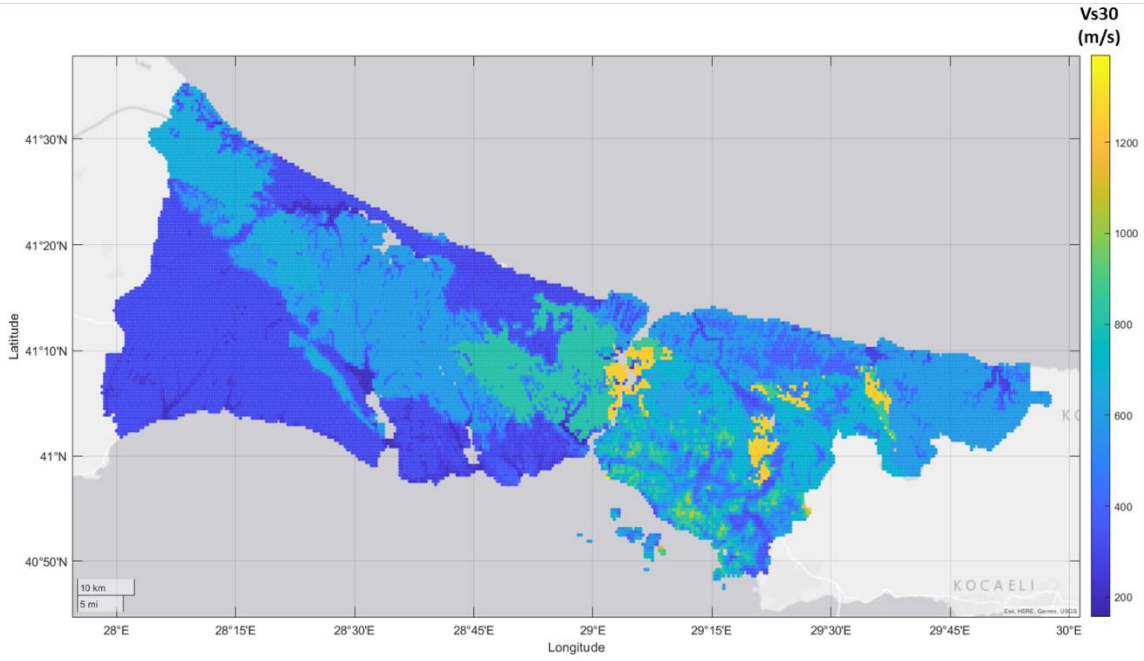

Figure 4.8. V_{S30} map based on the studies of IMM (2007, 2009) and MTA (2004).

In the initial test configuration, all source parameters—including magnitude, stress drop, and finite-fault rupture—were held constant, except for the hypocenter location, which was allowed to vary freely. This setup enabled the assessment of how different hypocenter positions influence observed ground motions. As illustrated in Figure 4.9, the hypocenter location significantly impacts the ground motion observations. Specifically, when the hypocenter is situated near the western end of the rupture, higher ground motions are detected near the eastern end. Conversely, when the hypocenter is positioned near the eastern end, higher ground motions tend to occur on the western side.

In the second test configuration, all source parameters—including magnitude, hypocenter location, and finite-fault rupture—were fixed, with the exception of the stress parameter, which was systematically varied. This approach facilitated the evaluation of the stress parameter's effect on ground motion levels. The results, shown in Figure 4.10, clearly demonstrate that increasing the stress parameter in increments of 10 bars leads to a linear rise in ground motion values across all observation locations when utilizing the EXSIM

algorithm. A thorough analysis on the uncertainty caused by hypocenter location and the stress parameter is developed and discussed in Süleyman and Çaktı (2024).

Subsequently, the estimated ground motions were compared with globally validated GMPEs. Based on these comparisons, optimal stress parameter values were determined to be 130 bars for events with magnitudes M7 and above, and 100 bars for events ranging from M6 to M7. These values were selected by observing the optimal match of the simulated ground motion values with the mean and one sigma estimations of the GMPEs. Figure 4.11 depicts the comparison of the M7.4 event with a 130-bar stress parameter against GMPEs, categorized by site class.

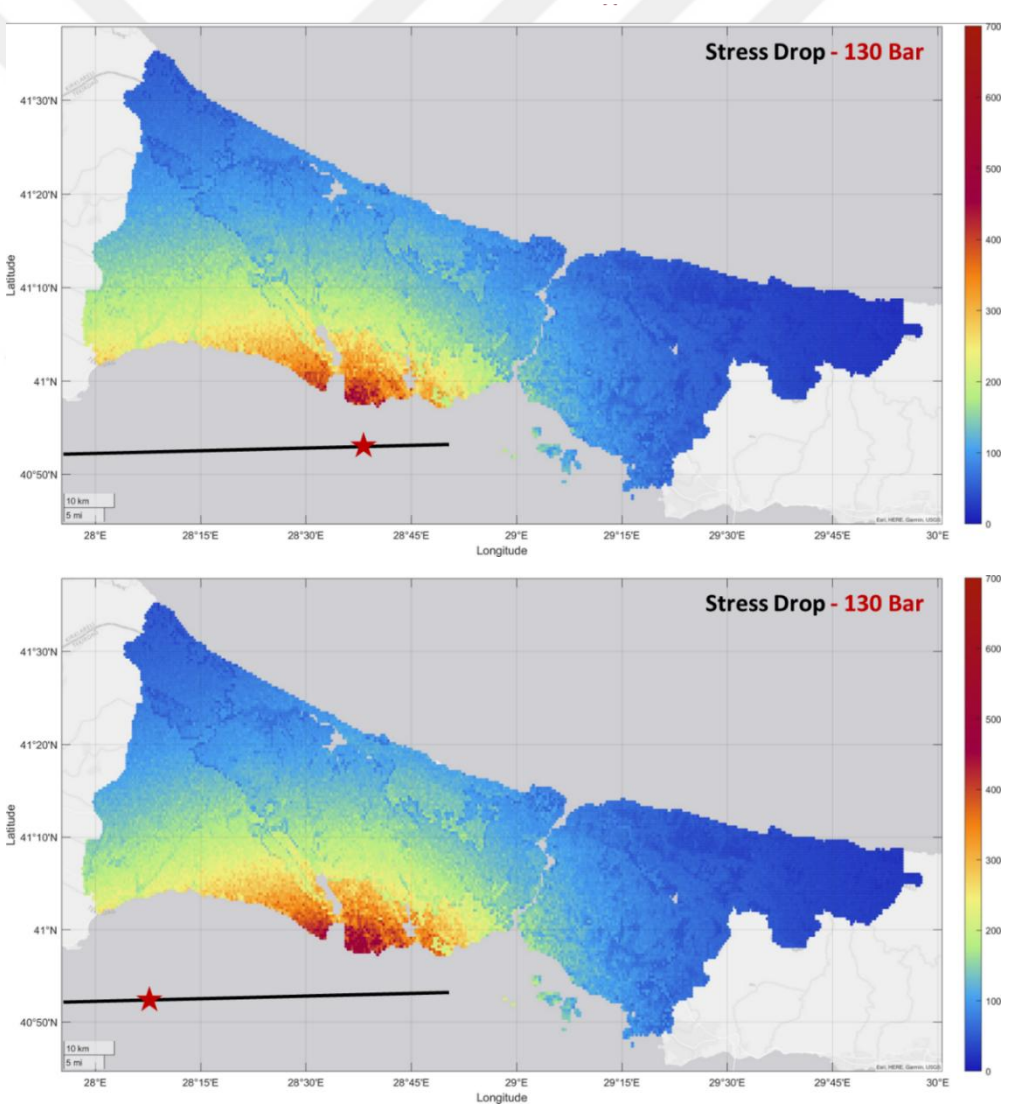

Figure 4.9. PGA distributions of M7.4 scenario, when hypocenter is located on east end of the rupture (a) and on the west of the rupture.

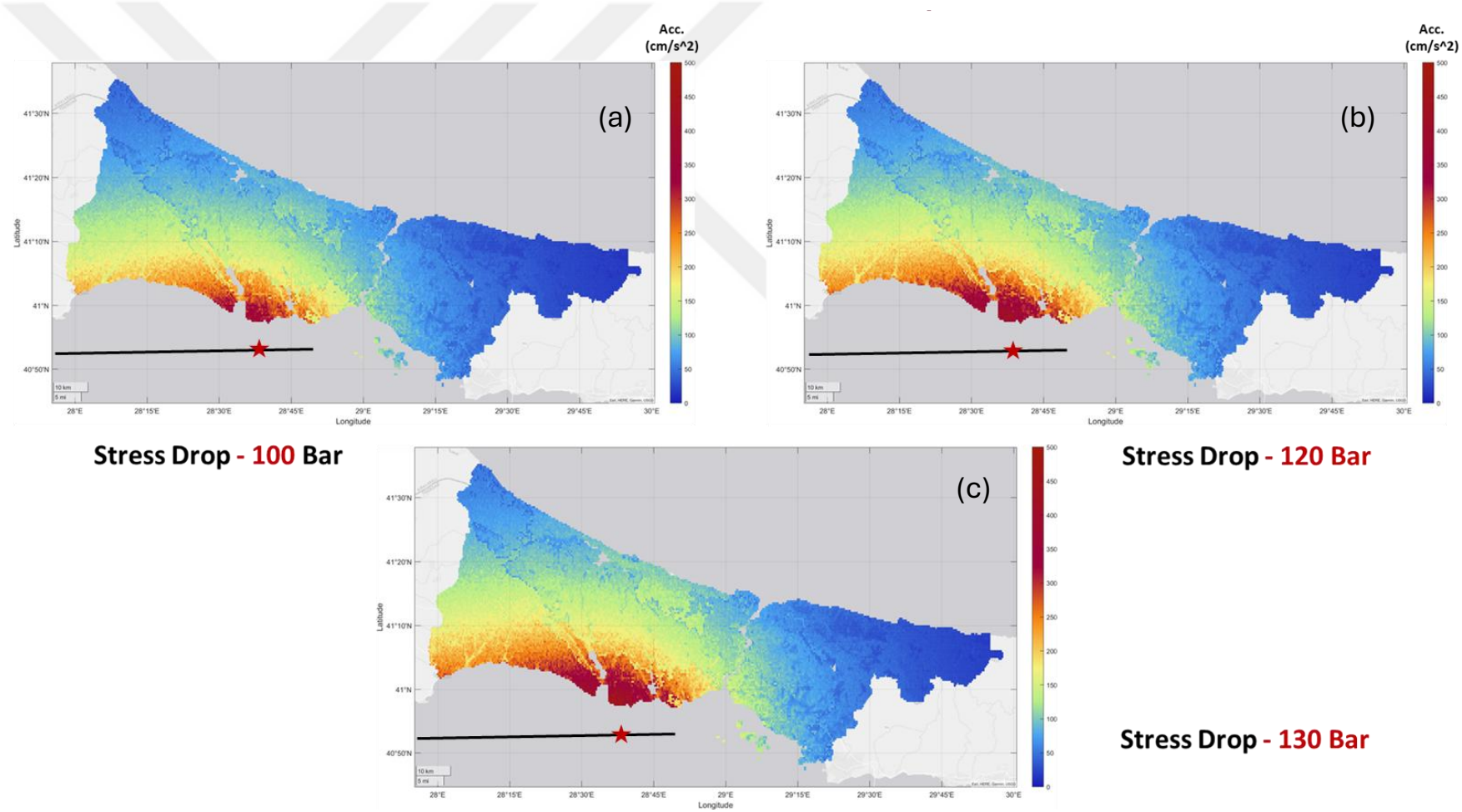

Figure 4.10. PGA distributions of M7.4 scenarios, considering stress parameter of (a) 100 bars, (b) 120 bars and (c) 130 bars.

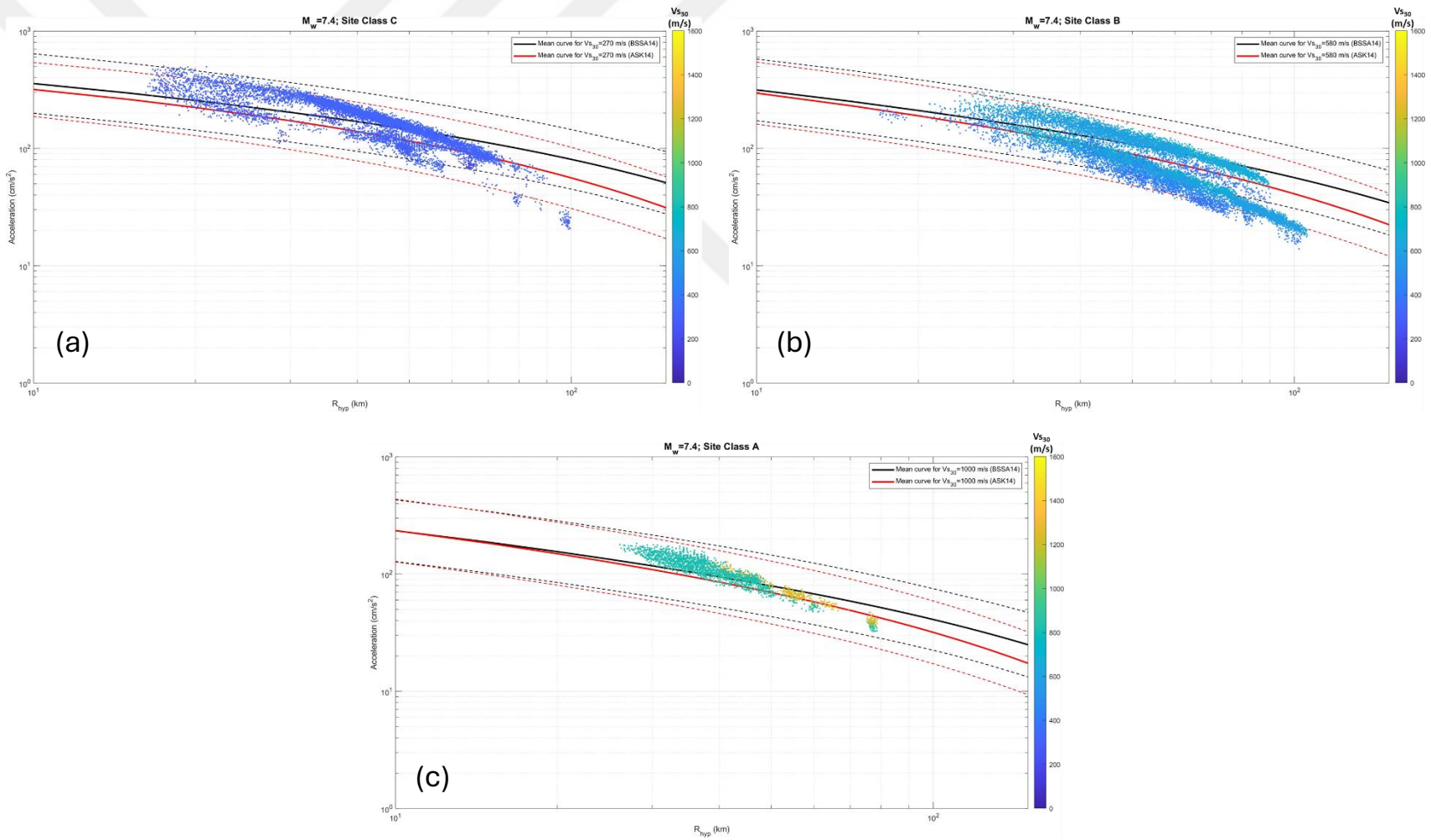

Figure 4.11. PGA distributions of M7.4 scenarios versus hypocentral distance, categorized in (a) site class C, (b) site class B and (c) site class A.

4.4.2. Simulations of Historical Istanbul Earthquakes

In this phase, simulations of destructive historical earthquakes that occurred near Istanbul were carried out. The earthquakes evaluated in the study by Yenihayat (2022) were considered for these simulations. In that study, the source parameters of the September 10, 1509; May 22, 1766; and July 10, 1894 Istanbul earthquakes were examined regionally using damage observations and information collected from various sources spread over a wide area.

Table 4.2. Adapted source parameters used in the ground motion simulations.

	1509	**1766**	**1766**	**1894**	**1894**
Magnitude	7.6	7.0	7.1	6.8	6.9
Num. of planes	Two planes	Single plane	Single plane	Single plane	Two planes
Stress drop (bar)	120	240	210	90	150
Plane 1					
L (km)	80	60	60	40	35
dL (km)	4	5	5	5	5
W (km)	16	12	12	12	12
dW (km)	4	3	3	3	3
Upper corner	27.9329, 40.8284	28.88, 40.87	28.88, 40.87	28.88, 40.87	28.88, 40.87
Depth of upper	3	3	3	3	3
Epicenter	28.88, 40.87	28.88, 40.87	28.43, 40.86	28.88, 40.87	29.2586, 40.7412
Focal depth (km)	5	5	5	5	5
Dip (degrees)	90	90	90	90	90
Strike (degrees)	87	267	267	111	114
Plane 2					
L (km)	40	—	—	—	25
dL (km)	4	—	—	—	5
W (km)	16	—	—	—	12
dW (km)	4	—	—	—	3
Upper corner	28.88, 40.87	—	—	—	29.2586, 40.7412
Depth of upper	3	—	—	—	3
Dip (degrees)	90	—	—	—	90
Strike (degrees)	111	—	—	—	91

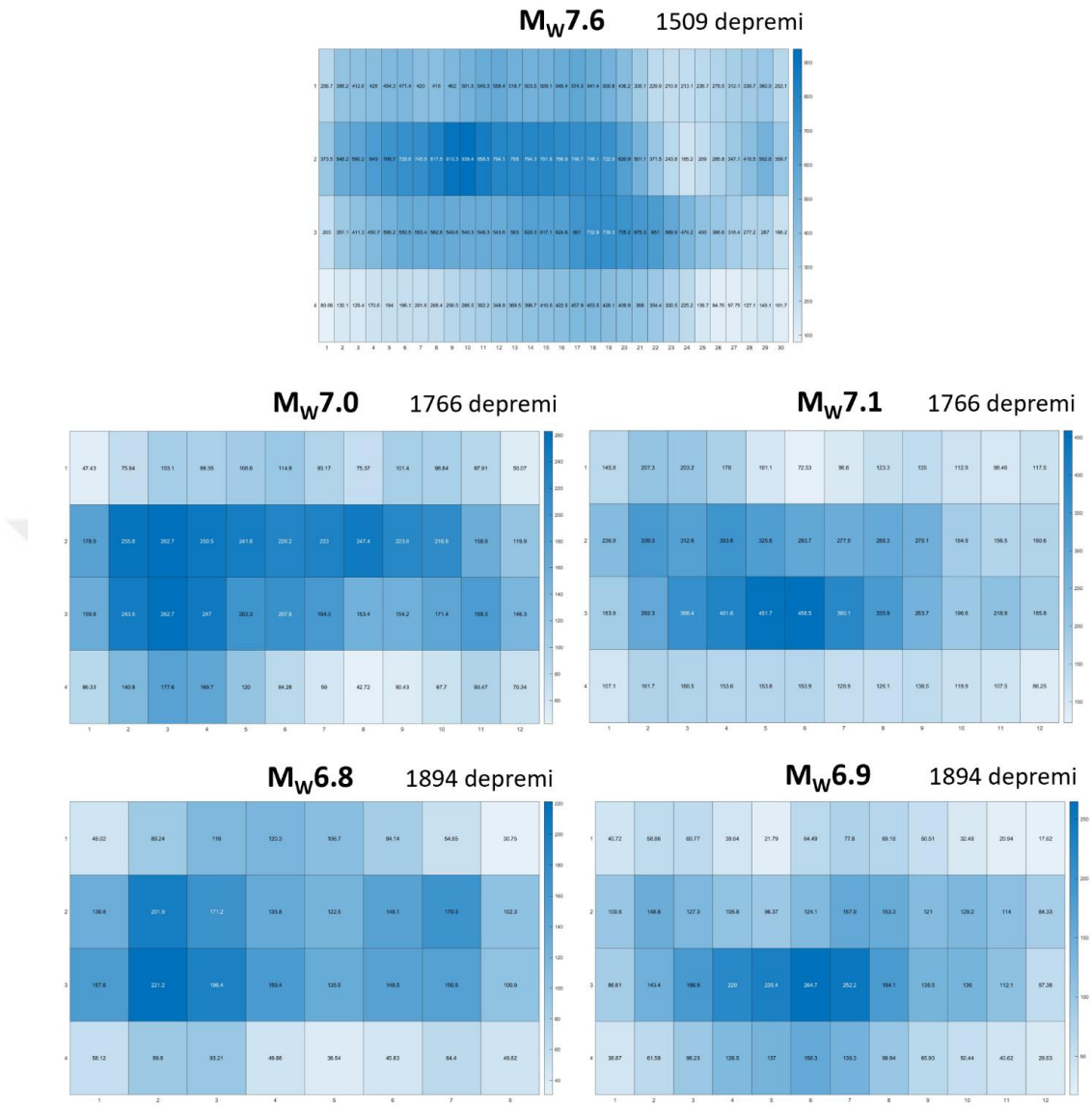

Figure 4.12. Two-dimensional displacement models in centimeters, generated using the Rupgen MATLAB routine.

Following the findings from Yenihayat (2022), the source parameters were adapted for use in stochastic ground motion simulations. Five different scenarios were considered for these three historical earthquakes. All the source parameters used in the simulations are compiled in Table 4.2. As seen in the table, a single-plane rupture assumption was made for some of these earthquakes, while a two-plane rupture was assumed for others. For the largest earthquake, the 1509 event, the total rupture length was determined to be 120 km, and for the smallest, the M_W 6.8 scenario of the 1894 earthquake, it was 40 km. The rupture widths were evaluated between 12–16 km. For each plane considered, small sub-rupture segments

with side lengths between 3–5 km were defined and modeled by assembling them. Each of these segments has a different displacement value. The modeling of these multi-segment sub-rupture planes using the aforementioned source parameters was carried out using the Rupgen (2000) MATLAB routine. Visualizations of the obtained displacement files are presented in Figure 4.12. In M_W 7.6 scenario, the maximum displacement value is 9.4 meters, and in the M_W 6.8 scenario, it is 2.2 meters. The stress drop parameter was taken to be in the range of 90–240 bars for all earthquakes.

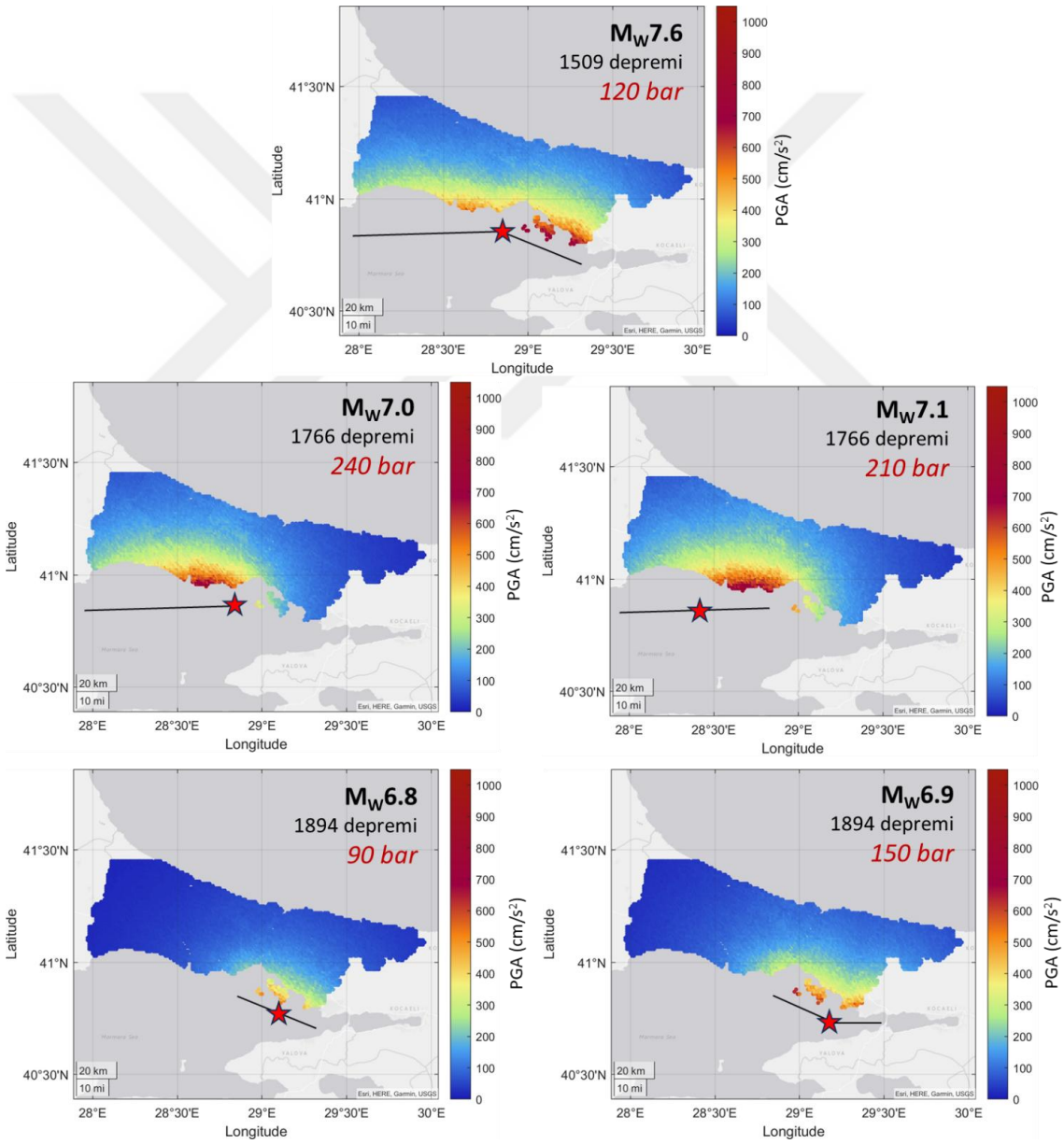

Figure 4.13. Distribution of PGA values obtained using the stochastic simulation method for five historical earthquakes.

Simulations were generated for the five scenario earthquakes at each point on the V_{S30} map. As expected, the highest intensity parameters were observed in the M_W 7.6 earthquake scenario. In this scenario, both the European and Asian sides of Istanbul's Marmara coast are exposed to acceleration values exceeding 1 g. In the M_W 7.0 and M_W 7.1 scenarios, the southern parts of the European side experience high acceleration values, while in the M_W 6.8 and M_W 6.9 scenarios, predominantly the southern part of the Asian side is affected. The distribution of acceleration values on the map can be seen in Figure 4.13. The obtained synthetic earthquake records and intensity parameters help address a significant gap for Istanbul and the Marmara region.

4.4.3. Simulations of Adapted Global Earthquakes

Research was conducted on the SRCMOD database to identify finite-fault rupture models suitable as earthquake scenarios for the NAF. From this research, we selected 13 strike-slip models with rupture dimensions comparable to the seismic gap in the Sea of Marmara (Beroza and Spudich, 1988; Wald et al., 1990; Wald and Heaton, 1994; Horikawa et al., 1996; Wald, 1996; Hernandez et al., 1999; Reilinger et al., 2000; Yagi and Kikuchi, 2000; Salichon et al., 2004; Dreger et al., 2005; Semmane et al., 2005; Mendoza and Hartzell, 2013; Hayes, 2017). Due to the limitations of the EXSIM algorithm, which only supports planar finite-fault models, we simplified and adjusted irregularly shaped finite-fault rupture models from the literature into either planar single-segment or double-segment configurations. Additionally, for rupture models with high number of subfaults, we reduced the number of subfaults through interpolation to optimize computational efficiency. The source parameters considered in the ground motion simulations can be found in Table 4.3.

The stochastic ground motion simulations of these finite-fault models were successfully finalized. In parallel, 3D physics-based simulations of the same finite-fault models were also realized (Çaktı, 2021-2025). Upon the completion of these simulations, the stochastically generated simulations are merged with physics-based simulations to generate synthetic broadband waveforms.

Table 4.3. Finite-fault models adjusted to NAF for ground motion simulations.

Event Name	Date	Finite-Fault Model Source	Magnitude	Segment	1. Corner Longitude	1. Corner Latitude	2. Corner Longitude	2. Corner Latitude	Stress Drop (bars)	Strike	Rupt. Length	Rupt. Width	Subfault Length	Subfault Width
Izmit (Turkey)	17-Aug-1999	Reilinger et al. (2000)	7.35	1/2	29.3198	40.7136	28.8652	40.8692	130	289	42	16	4.20	2.67
				2/2	28.8597	40.8711	28.0108	40.8375	130	268	71.5	16	7.15	2.67
Izmit (Turkey)	17-Aug-1999	Yagi and Kikuchi (2000)	7.34	1/2	29.3440	40.7146	28.8893	40.8701	130	289	42	16.5	4.20	2.75
				2/2	28.8800	40.8733	28.3202	40.8511	130	268	47.1	16.5	4.71	2.75
El Mayor-Cucapah (Mexico)	4-Apr-2010	Mendoza and Hartzell (2013)	7.27	1/2	29.3414	40.7062	28.8652	40.8692	130	289	44	14	5.50	2.80
				2/2	28.8597	40.8711	28.0108	40.8375	130	268	71.5	14	7.15	2.33
Landers (Calif.)	28-Jun-1992	Wald and Heaton (1994)	7.22	1/2	29.3440	40.7146	28.8893	40.8701	130	289	42	13.5	4.20	2.25
				2/2	28.8800	40.8733	28.4983	40.8581	130	268	32.1	13.5	3.21	2.25
Landers (Calif.)	28-Jun-1992	Hernandez et al. (1999)	7.15	1/2	28.9061	40.8564	28.8736	40.8675	130	289	3	13.5	0.60	4.50
				2/2	28.8626	40.8712	28.0019	40.8372	130	268	72.5	13.5	7.25	2.25
Hector Mine (Calif.)	16-Oct-1999	Salichon et al. (2004)	7.09	1/1	28.8624	40.8747	28.2390	40.8500	130	268	52.5	16.5	5.25	3.30
Ascension Island	29-Aug-2016	Hayes (2017)	7.02	1/2	29.2333	40.7433	28.8652	40.8692	130	289	34	14	4.25	2.80
				2/2	28.8597	40.8711	28.0108	40.8375	130	268	71.5	14	8.94	2.80
Kobe (Japan)	17-Jan-1995	Horikawa et al. (1996)	6.91	1/1	28.8624	40.8747	28.2746	40.8514	130	268	49.5	13.5	6.19	2.70
Kobe (Japan)	17-Jan-1995	Wald (1996)	6.86	1/2	29.3467	40.7137	28.8812	40.8729	100	289	43	17	5.38	3.40
				2/2	28.8773	40.8742	28.7034	40.8673	100	268	14.6	17	1.83	3.40
Tottori (Japan)	6-Oct-2000	Semmane et al. (2005)	6.61	1/1	29.3467	40.7137	29.0112	40.8285	100	289	31	17	3.88	3.40
Superstition Hills (Calif.)	24-Nov-1987	Wald et al. (1990)	6.45	1/1	29.3467	40.7137	29.1412	40.7840	100	289	19	10	2.38	2.00
Morgan Hill (Calif.)	24-Apr-1984	Beroza and Spudich (1988)	6.21	1/1	29.1934	40.7649	28.8740	40.8742	100	289	29.5	9	3.69	1.80
Parkfield (Calif.)	28-Sep-2004	Dreger et al. (2005)	6.05	1/1	29.3467	40.7137	28.9896	40.8359	100	289	33	14	4.13	2.80

**Length and width values are in km.*

4.5. Broadband Ground Motion Simulations

In a parallel study, the same scenarios with the same source parameters were simulated through 3D physics-based deterministic simulations by utilizing the open-source algorithm SPECFEM3D (Komatitsch and Tromp, 1999) to determine the low frequency content of the motion (Çaktı, 2021–2025). This methodology addresses the limitations of deterministic simulations, which are generally restricted to lower frequencies due to computational constraints. In this study, a 3D velocity model was developed for Istanbul and neighboring region. The simulations were successfully generated for the 0.05-1.5 Hz range. In our study, these simulations were used to develop broadband simulated waveforms by merging them with moderate-to-high frequency rich stochastic ground motion simulations, in frequency domain.

The generation of broadband ground motions involves combining low-frequency deterministic simulations with high-frequency components to achieve realistic waveform representations across a wide frequency spectrum. To apply this process, we followed the approach introduced by Smerzini and Villani (2012). The merging process involves synchronizing the low-frequency and high-frequency components in the time domain based on a normalized measure of Arias intensity, ensuring temporal alignment. Subsequently, the low-frequency and high-frequency motions are combined in the frequency domain using a weighted cosine-shaped matching filter. This filter smoothly transitions between the low-frequency and high-frequency contributions within a predefined overlap range, ensuring a seamless spectrum that covers both low and high frequencies. In this study, the simulation methods used were validated for specific frequency ranges: stochastic simulations perform reliably at 1.5 Hz and above, while three-dimensional physics-based simulations are reliable below about 1–1.5 Hz. Based on this, the optimal crossover range was chosen as 1.0–1.5 Hz. The visualization of the merging process for randomly selected waveforms is shown in Figure 4.14. More comparative waveforms from the merging process can be found in Figure A.1. In these examples—and in all other cases examined that are not presented here, the amplitudes within the frequency-domain transition band are nearly identical in the synthetics produced by both simulation methods, indicating a smooth handoff between them. The suitability of the selected crossover range is clearly visible in the figures. In the time domain, the synthetic records from the two methods are largely consistent in duration; however,

differences in frequency content led to acceleration amplitudes at different levels. The resulting broadband waveforms bridge the gap between deterministic and stochastic simulations, providing a comprehensive representation of seismic ground motions.

To obtain broadband ground motions, the steps of the procedure proposed by Smerzini and Villani (2012) are outlined below in sequence.

(i). Computation of Arias Intensity Values: For every location within the study area, the Arias Intensity of the waveforms obtained from the stochastic and deterministic simulations was calculated using

$$I_A = \frac{\pi}{2g}\int_0^{T_d} a(t)^2 dt \quad (m/s).$$

(ii). Determination of the 5% Arias Intensity Time: To synchronize the waveforms produced by the stochastic and deterministic simulations, the time at which the normalized Arias Intensity reaches 5% was identified.

(iii). Time Alignment and Signal-Length Consistency: To ensure that the normalized Arias Intensity values from both approaches (stochastic and deterministic) correspond to the same instant, zero-padding was applied at the beginning of the required record. Additionally, zeros were appended to the ends of the necessary ground motions to equalize record lengths.

(iv). Frequency-Domain Processing via the Fourier Transform: The time-aligned waveforms were transformed to the frequency domain using the Fourier Transform. The Fourier spectra of the synthetic time series were convolved with a prescribed weighting function, and the resulting sum was transformed back to the time domain using the Inverse Fourier Transform.

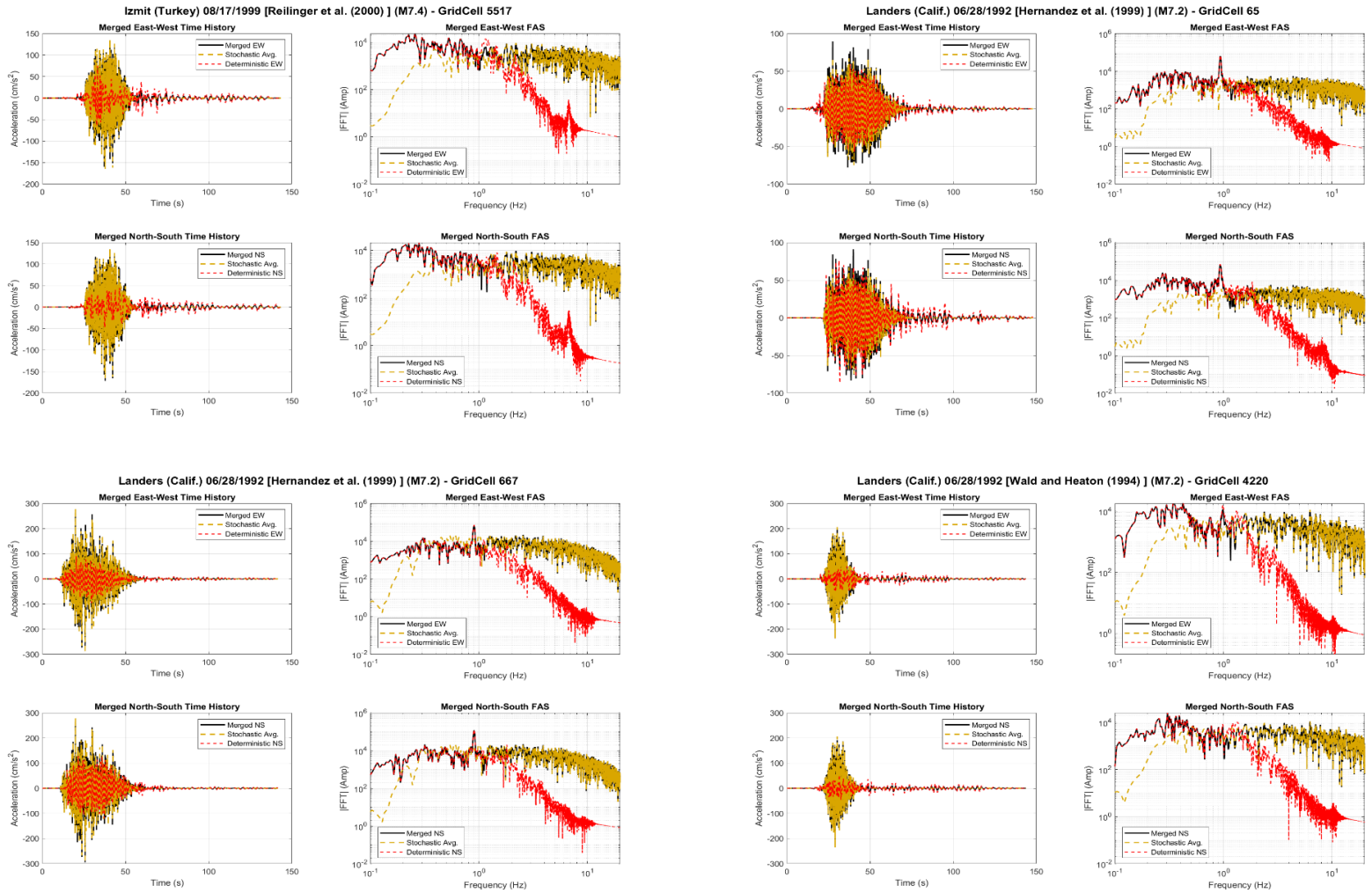

Figure 4.14. Merged waveforms at four selected grid cells, in time domain and frequency domain.

Figure 4.15 maps PGA, and Figure 4.16 maps RotD50 PSA at 0.3, 1, and 3 s for the 1894 (M_W 6.8–6.9) and 1766 (M_W 7.0–7.1) earthquakes. Overall, in these maps, PGA and PSA at 0.3 s are largely driven by the synthetic motions generated with the stochastic EXSIM simulations. Figure 4.15 shows the PGA distributions in the east-west and north-south directions. It can be said that the difference between the PGA values in both directions is relatively small. This is mainly due to the fact that the EXSIM algorithm outputs a single record in the horizontal direction.

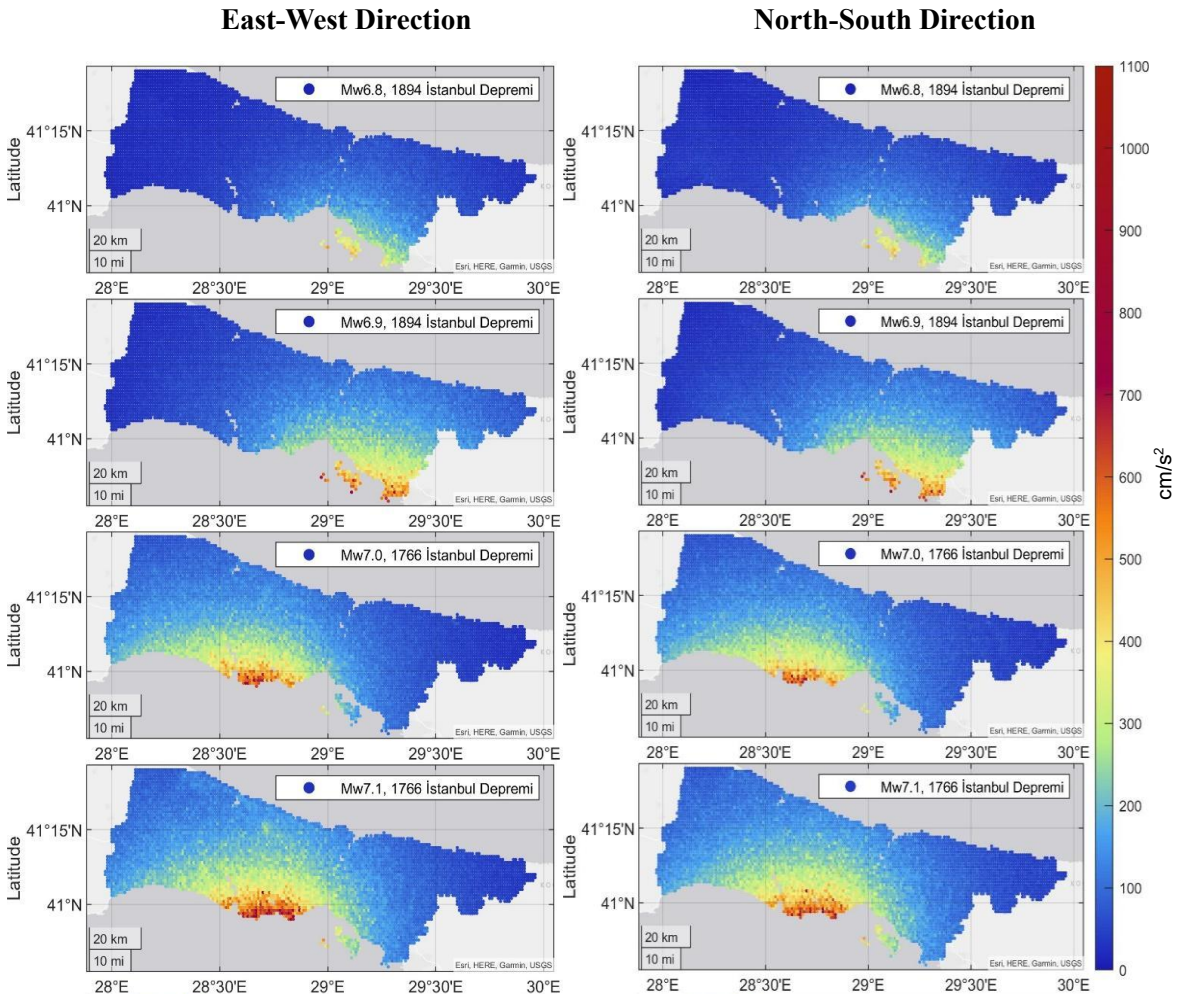

Figure 4.15. Distribution of PGA values obtained from broadband simulations for the 1894 (M_W 6.8 and M_W 6.9) and 1766 (M_W 7.0 and M_W 7.1) Istanbul earthquakes on the map.

Figure 4.16 maps RotD50 PSA from the broadband simulations at 0.3, 1, and 3 s. The period dependence is clear: PSA at 0.3 s is dominated by the stochastic EXSIM outputs, whereas PSA at 1 and 3 s is dominated by the 3D physics-based deterministic simulations. For the 1894 scenarios (M_W 6.8 and 6.9), larger PSA values appear on Istanbul's Asian side at 0.3 and 3 s, but shift to the European side at 1 s. For the 1766 scenarios (M_W 7.0 and 7.1), the European side shows higher PSA at all three periods.

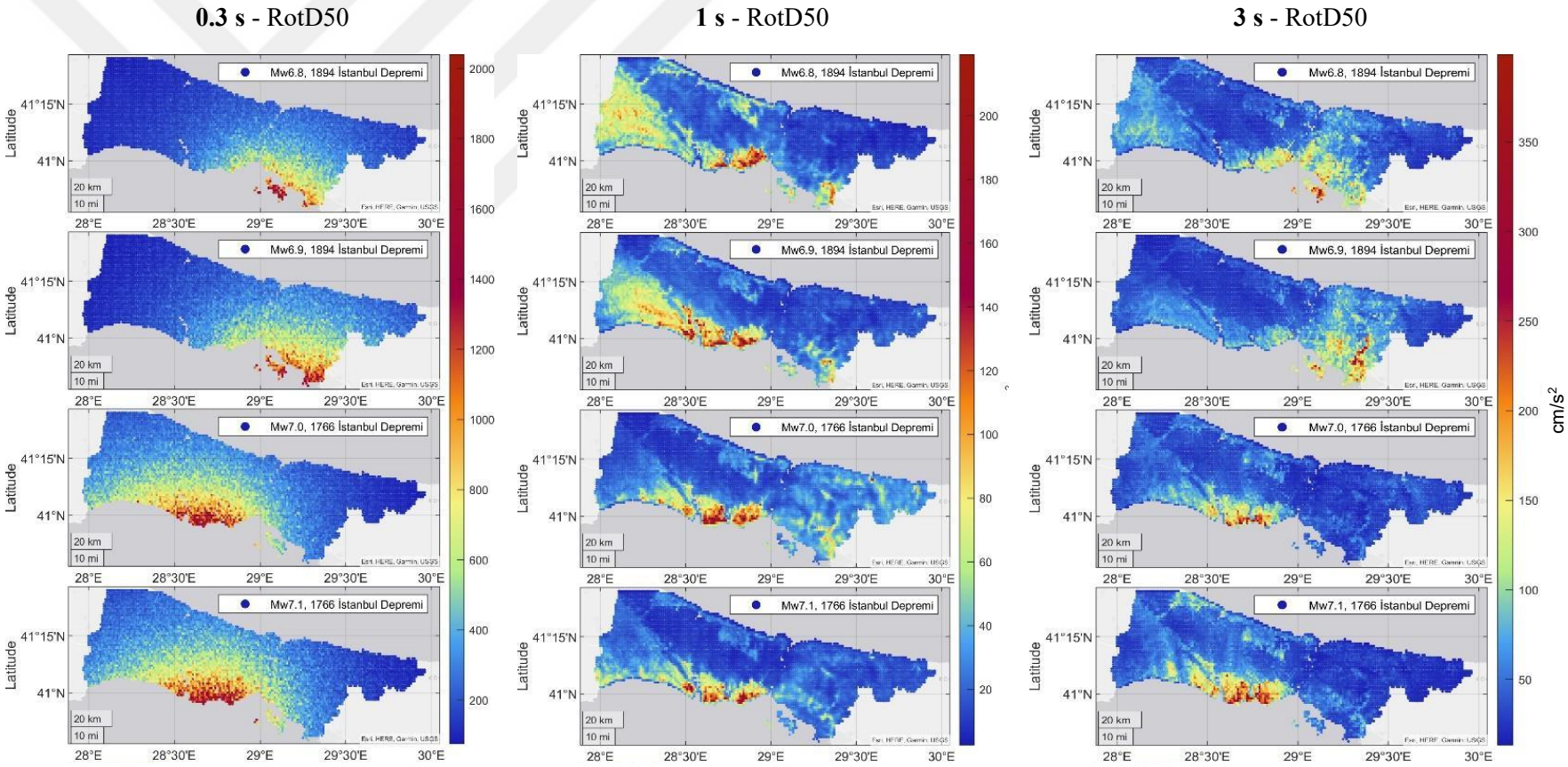

Figure 4.16. Distributions of RotD50 PSA at 0.3, 1 and 3 seconds obtained from broadband simulations for 1894 (M_W 6.8 and M_W 6.9) and 1766 (M_W 7.0 and M_W 7.1) Istanbul earthquakes on the map.

5. GMPE DEVELOPMENT

In this study, two distinct datasets were utilized to construct and calibrate ground motion prediction models. The first dataset comprises real, observed ground motion recordings from earthquakes with M_W ranging from 4.0 to 6.1, offering valuable constraints for moderate events. The second dataset consists of densely organized synthetic ground motions covering a magnitude range of M 6.05–7.6, allowing for model extension to larger, less frequently recorded magnitudes. By leveraging both real and simulated data, the resulting models aim to provide improved predictive capability across a broad spectrum of magnitudes. This section outlines the methodology employed in model formulation and parameter estimation. Additionally, it discusses the validation procedures for the developed models.

5.1. GMPEs Developed Using Real Ground Motions

The conceptual framework is based on the approach of Boore and Atkinson (2008), which offers a robust and physically interpretable structure by decoupling the ground-motion prediction into three components: distance attenuation, magnitude scaling, and site amplification. This model is particularly well-suited for our dataset, which includes moderate-magnitude earthquakes (M_W 4.0–6.1) with hypocentral distances ranging from 9 to 200 km. These ranges align well with the empirical constraints and validity domain of the Boore and Atkinson (2008) approach. Moreover, the flexible, piecewise formulation allows for careful modeling of near- and far-field attenuation behavior. While the final GMPE is presented at the end of this section, multiple models for distance and magnitude were explored prior to settling on the final piecewise formulations.

5.1.1. Data Selection and Filtering

5.1.1.1. Preliminary Data Filtering. The initial dataset contained recordings of both mainshocks and aftershocks. To ensure consistency and to avoid contamination by aftershock events, the aftershocks were eliminated due to their characteristically different

physical properties compared to mainshock events. The magnitude range was capped at M_W 6.1 because the 4.0–6.1 magnitude range provides a richer distribution of recordings at both near-field and far-field distances. Beyond M_W 6.1, the dataset's coverage becomes sparse. The selection of 200 km as the cutoff distance is based on the observation that recordings beyond this distance might be contaminated by surface waves, which are not the focus of this study.

5.1.1.2. RotD50 Calculation for GMPE Development. RotD50 is a statistically stable method used to define ground motion values reliably, particularly in GMPE development. It refers to the 50^{th}-percentile (or median) PSA obtained by rotating two orthogonal horizontal components of a ground motion and taking the median value at each spectral period (Boore, 2010). Because it considers ground motion across a continuum of directions, RotD50 is less sensitive to the arbitrary orientation of ground motion recordings compared to traditional measures such as the geometric mean. This orientation-independence makes RotD50 a more robust parameter for ground motion selection, hazard analysis, and structural design, as it helps capture the full range of potential shaking a structure might experience. Therefore, this parameter is calculated for each eligible recording accordingly and used in the GMPE development process.

5.1.1.3. Final Dataset. After filtering and processing, the dataset was prepared for GMPE development with the following key parameters as M_W, R_{hyp}, V_{S30}, RotD50 PGA, RotD50 PGV, and RotD50 PSA at multiple periods.

5.1.1.4. Partitioning the Dataset into Training and Test Sets. To ensure unbiased model evaluation, the dataset was partitioned into a training set (85%) and a test set (15%). The training set was used to estimate the model parameters, and the test set was withheld for performance validation. This partitioning approach is standard practice in GMPE development to prevent overfitting and to assess the model's predictive capability on unseen data.

5.1.2. Development of a Conventional GMPE Model

Boore and Atkinson (2008) developed a set of GMPEs designed to estimate PGA, PGV, and 5%-damped PSA for periods ranging from 0.01 to 10 seconds. Their work was part of the Next Generation Attenuation (NGA) project, which drew on an extensive database of strong-motion recordings primarily from active tectonic regions in western North America. In addition to covering a wide range of magnitudes, fault styles, and distances, these GMPEs focus on the geometric mean of the two horizontal components of recorded ground motions, aligning with the standard practice at the time (Boore and Atkinson, 2008).

The Boore and Atkinson (2008) GMPEs employ a logarithmic prediction model, in which the natural logarithm of the ground-motion parameter Y is expressed as a sum of terms representing magnitude scaling, distance attenuation, site amplification, and other factors (e.g., hanging-wall effects). The general form can be expressed as

$$\ln(Y) = f_{mag}(M) + f_{dist}(R, M) + f_{site}(V_{S30}) + f_{style}(\text{Faulting}) + \epsilon\sigma \,, \qquad (5.1)$$

where M is the moment magnitude, R is a distance metric (Joyner–Boore distance, R_{JB}), and ϵ is a normally distributed random variable capturing the aleatory variability σ of the model.

Boore and Atkinson's approach separates the GMPE into three core functional relationships: magnitude scaling, distance attenuation, and site amplification. This approach is isolating the influence of each variable on the predicted ground-motion level.

5.1.2.1. Magnitude Scaling Function, $f_{mag}(M)$. The magnitude term usually includes both linear and quadratic components, centered around a "hinge" magnitude (M_h). This hinge magnitude allows the slope of the magnitude-scaling curve to change beyond certain threshold magnitudes. A simplified representation is

$$f_{mag}(M) = c_1 + c_2\,(M - M_h) + c_3\,(M - M_h)^2, \qquad (5.2)$$

where c_1, c_2, c_3, and M_h are empirically derived coefficients.

5.1.2.2. Distance Attenuation Function, $f_{dist}(R, M)$. Ground-motion amplitudes generally decrease with distance due to geometric spreading and anelastic attenuation. GMPE models such as Boore and Atkinson (2008) incorporate both a logarithmic decay term

(to represent saturation at short distances) and a term to represent the rate of amplitude decay at larger distances. A simplified distance function may be written as

$$f_{dist}(R, M) = c_4 \ln\left(\sqrt{R^2 + h^2}\right) + c_5 \sqrt{R^2 + z^2}\ , \tag{5.3}$$

where R is typically R_{JB}, z is a depth or distance-saturation parameter, and c_4, c_5 are regression-derived constants. Some variations include magnitude-dependent terms to refine how distance decay behaves at different magnitudes.

5.1.2.3. Site Amplification Function, $f_{site}(V_{S30})$. To represent site-specific effects, Boore and Atkinson use a function of V_{S30}. The model incorporates a reference velocity (V_{ref}), often around 760 m/s (the NEHRP B/C boundary), against which site conditions are compared. A typical site function might be

$$f_{site}(V_{S30}) = b_1 \ln\left(\frac{V_{S30}}{V_{ref}}\right) + b_2\ , \tag{5.4}$$

with b_1 and b_2 determined by regression, and additional adjustments for very soft or very stiff sites as required.

By treating magnitude, distance, and site amplification as separate functions, this methodology allows the model to flexibly accommodate physical processes influencing ground motion. The regression analysis on thousands of recording data points yields the coefficients for each parameter, thereby enabling robust predictions over a broad range of magnitudes, distances, and site conditions. As a result, the Boore and Atkinson (2008) GMPEs have been widely adopted in seismic hazard evaluations, building code development, and risk assessments, providing a practical balance between model simplicity and alignment with observed data.

5.1.3. Exploration of Functional Forms

5.1.3.1. Distance Attenuation Models. A key objective was to capture the decay of ground-motion amplitude with distance. Modern GMPEs typically adopt either purely logarithmic or piecewise expressions to accommodate different attenuation behaviors at near-source and far-source distances (Atkinson and Boore, 1995; Abrahamson et al., 2014). In this study, multiple distance formulations were tested. In the following part, the testing approach is explained.

One important step was the choice of “hinge” or “switch” distance. We systematically tested hinge values from 30 km to 180 km, in increments of 10 km. For each candidate hinge distance, we fit the GMPE’s distance coefficients to the training data and evaluated the model’s R^2 performance across multiple spectral periods, including PGA and PGV. The hinge distance yielding the highest overall R^2 was selected for the final model.

During this process, various functional forms were fitted to test their suitability on the dataset. Below, those models are explained.

(i) Piecewise Log-Linear

- Near-field ($R \leq R_h$): A linear dependence on $ln(R)$.
- Far-field ($R > R_h$): Maintains a log-linear slope but with a shifted intercept or possibly additional terms.

(ii) Log-Linear + Quadratic or Exponential Tail

- Various attempts were made at modeling far-field decay with polynomial or exponential functions. However, the simpler piecewise log-linear approach ultimately provided a stable and interpretable solution for the magnitude–distance range of interest.

(iii) Power-Law Decay

- Another family of models replaced the far-field ln(R) dependence with a negative power law. Though conceptually appealing for large distances, this approach did not significantly improve predictive performance relative to the simpler piecewise log-linear.

In the final chosen distance model, we used a two-part log-linear form with a hinge distance of $R_h = 80$ km (obtained by scanning hinge values from 30–180 km). This piecewise formulation adequately captured near-source and far-source attenuation observed in the dataset. Malcıoğlu et al. (2022) have observed the abrupt change in ground motions at around 60 km of distance, for the M_W 4.5 and M_W 5.8 Silivri earthquakes that occurred in 2019, near Istanbul.

5.1.3.2. Magnitude Scaling Models. Alongside distance attenuation, the magnitude-scaling function describes how ground motion amplitude changes with event size. Numerous

functional forms exist in literature, from purely linear terms to more complex polynomials or hinge-based piecewise expressions (Boore and Atkinson, 2008; Campbell and Bozorgnia, 2008).

Similar to distance modeling, we adopted a piecewise magnitude function with a hinge value (M_h). To locate the optimum hinge, we systematically tested M_W values from 4.4 to 5.8 in increments of 0.1. For each candidate M_h, we refit the GMPE parameters to the training data and computed the overall R^2 across the entire spectral range (including PGA and PGV). The hinge value that maximized the average R^2 was selected for the final model.

The following points describe the models evaluated in this study.

(i) Linear–Quadratic Piecewise

- In this case, events below M_h fit a linear or quadratic model; while events above M_h assume a different polynomial or exponential component.

(ii) Hybrid Polynomial-Exponential

- Lower magnitudes might follow a simple polynomial, whereas the high-magnitude side might include exponential attenuation to reflect saturation of ground motion at large magnitudes. Particularly, saturation is more apparent for the $M_W > 6$ events. In our case, saturation is very limited.

(iii) Piecewise Linear

- This model was chosen for simplicity and robust performance. Specifically, for $M < M_h$ a linear slope was applied, and for $M > M_h$, a shifted linear slope was used to reflect a different rate of amplitude increase.

In practice, the simplest piecewise linear approach (with a single hinge) provided a balance between interpretability and fit quality for the magnitude range 4.0–6.1. The final selected hinge was $M_h = 4.9$, determined via the systematic scan from 4.4 to 5.8 in 0.1 increments.

5.1.4. Two-Stage Regression Procedure

Following the methodology of Boore and Atkinson (2008) and similar studies (Campbell and Bozorgnia, 2008; Chiou and Youngs, 2008; Boore et al., 2014), a two-stage regression procedure was employed to decouple the distance and magnitude effects:

Stage 1: Distance Regression; The model's distance coefficients were estimated by regressing the natural log of the observed ground motion on the chosen distance function alone. This produced a partial residual that removed distance effects from the data.

Stage 2: Magnitude Regression; The partial residual from Stage 1 was then regressed on the magnitude function, yielding the magnitude-scaling coefficients.

This staged approach allows each component (distance vs. magnitude) to be fit in a more tractable manner, minimizing inter-dependences during optimization.

5.1.5. Site Amplification

5.1.5.1. Role of V_{S30} and Rock PGA. To account for local site effects, the GMPE includes amplification terms dependent on V_{S30}. Many authors introduce additional nonlinearity whereby the site term depends not only on V_{S30} but also on the predicted rock PGA level (e.g., Boore and Atkinson, 2008). Lower-velocity sites tend to exhibit stronger amplification at higher levels of shaking, leading to saturation or other complexities.

In this study, a generic non-linear amplification function was tested, calibrated such that rock PGA is estimated by evaluating the distance and magnitude terms at $V_{S30} = V_{ref}$. A site amplification component is then added to the predicted log ground motion, reflecting additional gains for soft soils and minimal gains for rock sites.

5.1.5.2. Best-Fit Nonlinear Site Terms. After removing distance and magnitude trends, the remaining residuals were used to fit coefficients describing how site response changes with increasing input motion (i.e., the predicted rock PGA). These coefficients were optimized to minimize residual variance for the training dataset, thereby providing an additional layer of physical realism for soft sites.

5.1.6. Final GMPE Formulation

The final GMPE structure can be summarized as:

Distance function: Piecewise log-linear function with a hinge at R_h = 80 km as

$$f(R) = \begin{cases} c_1 + c_2 \ln\left(\frac{R}{R_{\text{ref}}}\right), & R \le R_{\text{h}} \\ c_3 + c_4 \ln\left(\frac{R}{R_{\text{ref}}}\right), & R > R_{\text{h}} \end{cases}, \tag{5.5}$$

- c_1, c_2: Coefficients for the near-field attenuation model.
- c_3, c_4: Coefficients for the far-field attenuation model.
- R: Hypocentral distance (in km or other units).
- R_{ref}: Reference distance, used for normalization, taken as 1 km.
- R_h: Threshold distance separating near-field and far-field regions.

Magnitude function: Piecewise linear function with a hinge at M_h = 4.9 as

$$f(M) = \begin{cases} e_1 + e_2 M, & M \le M_{\text{h}} \\ e_3 + e_4 (M - M_{\text{h}}), & M > M_{\text{h}} \end{cases} \tag{5.6}$$

- e_1, e_2: Coefficients for the low-magnitude model.
- e_3, e_4: Coefficients for the high-magnitude model.
- M: Earthquake magnitude.
- M_h: Threshold magnitude separating low and high magnitude regions.

Site amplification function: Non-linear amplification based on V_{S30} and predicted rock PGA.

The nonlinear amplification factor, F_{NL}, accounts for site-specific effects based on the V_{S30} and PGA. To compute this parameter, fixed constants (a_1, a_2, V_1, V_2, V_{ref}, PGA_{low} and refPGA) as defined by Boore and Atkinson (2008) are utilized. F_{NL} is computed using a piecewise approach as

$$F_{NL} = \begin{cases} b_{nl} \ln\left(\frac{\text{PGA}_{\text{low}}}{\text{refPGA}}\right), & PGA_{rock} \le a_1 \\ b_{nl} \ln\left(\frac{\text{PGA}_{\text{low}}}{\text{refPGA}}\right) + c' \ln\left(\frac{\text{PGA}_{\text{rock}}}{a_1}\right)^2 + d' \, l\, n\left(\frac{\text{PGA}_{\text{rock}}}{a_1}\right)^3, & a_1 < PGA_{rock} \le a_2 \\ b_{nl} \ln\left(\frac{\text{PGA}_{\text{rock}}}{\text{refPGA}}\right), & PGA_{rock} > a_2 \end{cases} \tag{5.7}$$

- a_1, a_2: Peak ground acceleration thresholds (a_1 = 29.43 cm/s^2, a_2 = 88.29 cm/s^2).
- PGA_{low}: Lower bound PGA value for nonlinear amplification (58.86 cm/s^2).
- refPGA: Reference PGA value (98.1 cm/s^2).
- PGA_{low}: PGA calculated at rock level, using the sum of the magnitude and distance scaling equations.

Coefficients for Middle Region ($a_1 < PGA_{rock} \leq a_2$) are formed as

$$\Delta x = \ln\left(\frac{a_2}{a_1}\right), \quad \Delta y = b_{nl} \ln\left(\frac{a_2}{PGA_{low}}\right),$$
$$c' = \frac{3\,\Delta y - b_{nl}\,\Delta x}{\Delta x^2}, \quad d' = \frac{-2\,\Delta y - b_{nl}\,\Delta x}{\Delta x^3}. \tag{5.8}$$

- Δx, Δy: Differences in log space for defining the polynomial coefficients.
- c', d': Coefficients for the quadratic and cubic terms in the middle region.

b_{nl} parameter in the above equations can be expressed as

$$b_{nl} = \begin{cases} b_1, & V_{S30} \leq V_1 \\ (b_1 - b_2) \cdot \frac{ln\left(\frac{V_{S30}}{V_2}\right)}{ln\left(\frac{V_1}{V_2}\right)} + b_2, & V_1 < V_{S30} \leq V_2 \\ b_2 \cdot \frac{ln\left(\frac{V_{S30}}{V_{ref}}\right)}{ln\left(\frac{V_2}{V_{ref}}\right)}, & V_2 < V_{S30} < V_{ref} \\ 0, & V_{S30} \geq V_{ref} \end{cases} \tag{5.9}$$

- b_{nl}: Nonlinear slope, dependent on V_{S30}.
- b_1, b_2: Nonlinear slope parameters for specific V_{S30} ranges.
- V_1, V_2, V_{ref}: Shear wave velocity thresholds (V_1 = 180 m/s, V_2 = 300 m/s, V_{ref} = 760 m/s).

Symbolically, the final log of PSA (or PGA, or PGV) can be expressed as

$$\ln(\mathrm{IM}) = f_{dist}(R;\, \boldsymbol{c},\, R_h) + f_{mag}(M;\, \boldsymbol{e},\, M_h) + f_{site}(V_{S30},\, PGA_{rock};\, \mathbf{b}). \tag{5.10}$$

The final model includes all the three functions developed in this study, namely, distance-scaling, magnitude-scaling and nonlinear amplification models. The coefficient of all three functions can be found in Table 5.1.

Table 5.1. Coefficients of the prediction model.

	Distance-scaling coefficients				Magnitude-scaling coefficients				Site-amplification coefficients	
T(s)	**c_1**	**c_2**	**c_3**	**c_4**	**e_1**	**e_2**	**e_3**	**e_4**	**b_1**	**b_2**
PGV	2.964	-1.408	2.878	-1.311	0.145	-0.251	-0.723	2.326	-1.961	-0.511
PGA	6.122	-1.397	8.713	-1.896	5.763	-1.577	-0.585	1.882	-1.336	-0.328
0.02	6.151	-1.396	8.810	-1.911	6.208	-1.684	-0.582	1.872	-1.328	-0.316
0.04	6.253	-1.385	9.008	-1.933	8.288	-2.187	-0.569	1.830	-1.291	-0.255
0.06	6.363	-1.342	10.145	-2.127	10.887	-2.812	-0.550	1.765	-1.164	-0.170
0.08	6.230	-1.252	10.950	-2.249	12.151	-3.107	-0.557	1.733	-1.154	-0.154
0.1	6.193	-1.211	11.194	-2.265	11.331	-2.904	-0.546	1.696	-1.084	-0.178
0.12	6.437	-1.255	11.437	-2.294	8.806	-2.294	-0.541	1.702	-1.187	-0.228
0.14	6.692	-1.311	11.245	-2.239	7.646	-2.014	-0.539	1.704	-1.228	-0.250
0.16	6.878	-1.356	11.056	-2.190	0.511	-0.287	-0.520	1.696	-1.130	-0.279
0.18	7.019	-1.394	10.583	-2.083	-0.054	-0.152	-0.531	1.728	-0.850	-0.350
0.2	7.068	-1.416	10.247	-2.014	0.422	-0.267	-0.555	1.779	-0.812	-0.405
0.22	7.021	-1.420	9.790	-1.924	0.523	-0.293	-0.579	1.832	-0.892	-0.460
0.24	6.935	-1.415	9.399	-1.853	0.739	-0.349	-0.598	1.889	-1.078	-0.499
0.26	6.847	-1.410	9.094	-1.804	-3.221	0.607	-0.609	1.940	-1.268	-0.527
0.28	6.735	-1.399	8.683	-1.734	-5.043	1.043	-0.624	1.997	-1.440	-0.525
0.3	6.699	-1.407	8.237	-1.656	-6.391	1.366	-0.641	2.050	-1.529	-0.542
0.35	6.480	-1.400	7.150	-1.464	-8.065	1.766	-0.677	2.154	-2.062	-0.559
0.4	6.177	-1.376	6.129	-1.283	-8.634	1.895	-0.688	2.210	-2.487	-0.572
0.45	6.021	-1.389	5.426	-1.164	-9.118	2.006	-0.694	2.248	-2.768	-0.585
0.5	5.826	-1.387	4.960	-1.095	-9.506	2.096	-0.701	2.282	-2.694	-0.631
0.6	5.514	-1.391	3.872	-0.925	-8.091	1.735	-0.713	2.368	-2.765	-0.695
0.7	5.233	-1.392	2.792	-0.757	-6.537	1.344	-0.726	2.446	-2.829	-0.731
0.8	4.891	-1.364	2.175	-0.679	-7.111	1.474	-0.742	2.517	-3.067	-0.736
0.9	4.565	-1.335	1.792	-0.643	-8.673	1.851	-0.754	2.551	-2.936	-0.771
1	4.192	-1.289	1.783	-0.675	-10.720	2.348	-0.780	2.611	-2.868	-0.792
1.2	3.663	-1.246	1.353	-0.657	-10.352	2.249	-0.835	2.760	-2.894	-0.766
1.4	3.425	-1.263	0.822	-0.613	-10.829	2.366	-0.875	2.840	-2.847	-0.749
1.6	3.072	-1.240	0.548	-0.614	-9.869	2.132	-0.894	2.881	-2.682	-0.743
1.8	2.807	-1.233	0.232	-0.599	-9.655	2.078	-0.912	2.925	-2.476	-0.720
2	2.557	-1.223	-0.030	-0.593	-9.771	2.107	-0.926	2.955	-2.319	-0.687
2.5	1.903	-1.161	-0.655	-0.563	-8.144	1.721	-0.945	2.956	-2.103	-0.613
3	1.231	-1.066	-0.682	-0.632	1.589	-0.645	-0.966	2.996	-1.884	-0.593
3.5	0.267	-0.905	-1.077	-0.616	-4.694	0.892	-0.974	2.982	-1.903	-0.539
4	0.716	-1.085	-1.535	-0.581	-3.924	0.708	-0.962	2.939	-1.876	-0.521
4.5	0.526	-1.100	-1.544	-0.632	1.896	-0.705	-0.955	2.913	-1.835	-0.503
5	0.398	-1.125	-1.512	-0.685	-2.013	0.248	-0.934	2.863	-1.842	-0.496

5.1.7. Variability Analysis

5.1.7.1. Intra-Event and Inter-Event Residuals. To assess the model's performance, residuals were decomposed into:

- Between-event (inter-event) term, eta: Captures systematic shifts in ground-motion for a given event.
- Within-event (intra-event) term, epsilon: Captures station-to-station and record-to-record variability after controlling for event-specific effects.

The standard deviations of these residual terms are:

- $\tau = \text{StdDev}(\eta)$
- $\phi = \text{StdDev}(\varepsilon)$
- $\sigma = \sqrt{\tau^2 + \phi^2}$, the total standard deviation of the model.

5.1.7.2. Model Comparison. For each combination of hinge distances (30–180 km) and hinge magnitudes (4.4–5.8), the total residual variance and the corresponding R^2 on the test set were evaluated. The hinges that maximized the average R^2 across all spectral periods (including PGA and PGV) were chosen for the final GMPE.

The above process was repeated for a cross-validation check. The 85% training data set and 15% test dataset were redefined by randomly reselecting the recordings and to approve the consistency of the chosen model. However, due to the limited data between magnitudes M_W 5.2-6.1, this wasn't purely randomized. Therefore, it was needed to ensure that training and testing datasets include similar proportions of data from the same magnitudes. With this adjustment, the cross-validation process was subjectively biased, to ensure even distribution of the magnitudes in both datasets. After this adjustment, the performance across all sets of redefined training-test datasets yielded very similar results. As a result, the set yielding the highest R^2 results was chosen as the final set of data to train and test our model.

The residual analysis was performed against hypocentral distance. As can be seen from the resulting plots for PGA and PGV in Figure 5.1, and for all spectral periods in Figure B.1

in Appendix B, the data points remain nearly equally scattered on both sides of the unity line, which can also be confirmed by the mean values placed on the top left corner of the plots. The one-sigma estimations of the residuals remain around 0.8, while it gets lower at 3-5 s PSA estimates.

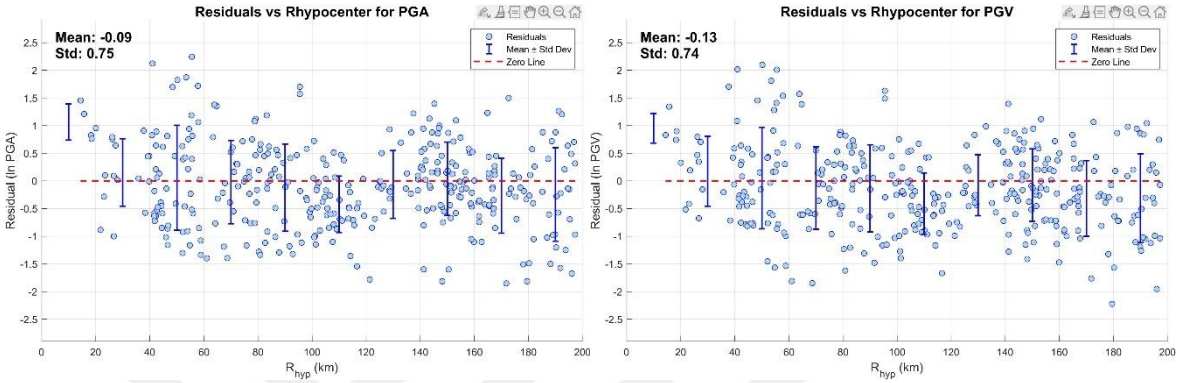

Figure 5.1. Residuals versus hypocentral distance for PGA and PGV.

The following Figure 5.2 shows the observed versus predicted data and the R^2 estimations, for PGA and PGV; while for spectral accelerations at all periods considered are presented in Figure B.2. For an easier comparison, logarithmic scale is used in these figures.

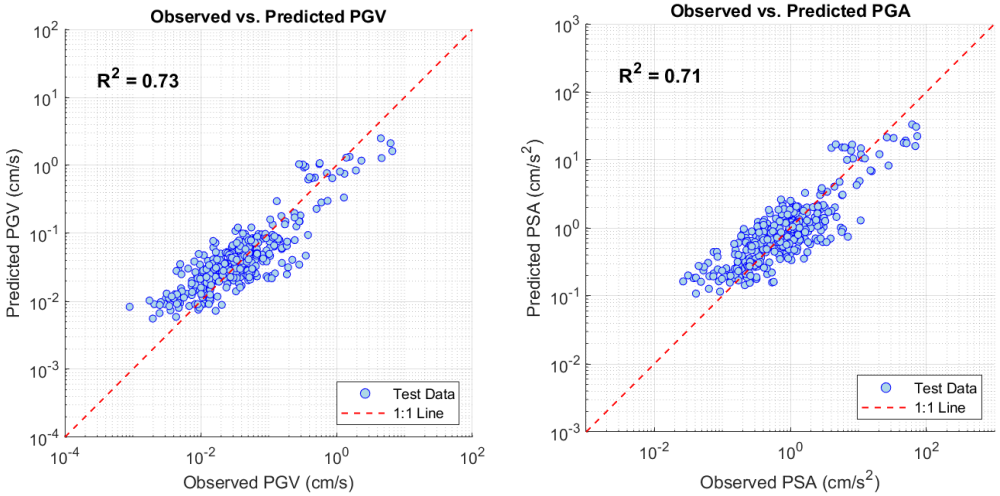

Figure 5.2. Predicted versus observed PGA, PSAs at 0.02-5 seconds and PGV comparisons.

5.1.8. Machine-Learning–Enhanced GMPE

Although the piecewise log-linear GMPE furnishes a physically transparent baseline and reproduces the principal trends in the data, a complementary machine-learning (ML) residual model was trained to determine whether any remaining variance could be further reduced without altering the underlying functional forms. To preserve the explanatory power of the classical coefficients yet exploit data-driven flexibility, a gradient-boosted regression tree (GBRT) model was trained to predict the natural-log residual $\Delta\ln(Y) = \ln(Y_{observed}) - \ln(Y_{classical\ GMPE})$. The target residual therefore already incorporates the two-stage distance–magnitude regression and site term described in previous subsections.

5.1.8.1. Gradient-Boosted Regression Trees. Gradient-boosted regression trees construct an ensemble of shallow decision trees in a stage-wise fashion, where each successive tree is fitted to the residual error of the aggregate of all previous trees. At each iteration, the algorithm identifies regions of the feature space (here defined by magnitude, distance, VS_{30}, predicted rock-PGA, etc.) where the current ensemble systematically under- or over-predicts, and then fits a new tree to correct those errors. By adding together many such "weak learners," each with limited depth and regularization, GBRT achieves high predictive accuracy while controlling over-fitting through shrinkage (small learning rates) and tree complexity constraints (maximum depth, minimum samples per leaf).

This approach is particularly well suited to our GMPE residual problem because it can flexibly model nonlinear interactions (such as subtle magnitude–distance–site couplings) that are difficult to encode in closed-form equations, yet still retains interpretability via feature-importance metrics. The use of decision trees accommodates both continuous and categorical predictors without requiring data transformation, and the boost-and-regularize framework ensures that corrections remain modest relative to the physically motivated baseline. As our goal is to enhance, not replace, the classical GMPE, GBRT provides a transparent, data-adaptive layer that refines prediction residuals without compromising the functional structure developed in previous subsections.

5.1.8.2. Integrating GBRT to GMPE model. The parameter vector supplied to the GBRT consisted of moment magnitude, hypocentral distance, V_{S30} and the classical GMPE's

predicted rock-level PGA (as a proxy for expected non-linearity). The same 85 % - 15 % split was retained to ensure the ML training set matched the classical regression set, and five-fold cross-validation inside the training portion was used for parameter tuning (such as, 100-tree learning rate). Least-squares boosting approach is applied to the regression to minimize the mean-squared error, to avoid over-fitting the relatively small number of $M_W > 5$ recordings.

After optimization, the GBRT reduced the total residual standard deviation σ for over 10% in average, when compared in natural-log units over the full period range. It also improved the average test-set R^2 to above 0.8 (see Table 5.2) at most periods. Our ML-enhanced GMPE model mainly corrects subtle magnitude-distance-site interactions rather than replacing the physics-based core. For transparency, the final ML-enhanced prediction is expressed as

$$\ln Y_{\text{ML-enhanced MPE}}(T) = \ln Y_{\text{classical MPE}}(T) + \Delta_{\text{GBRT}}(M, R, V_{S30}), \quad (5.11)$$

where Δ_{GBRT} is the ML-derived residual at the spectral period T.

5.1.9. Model Comparison

The modeling of the empirical dataset covering the M_W 4.0–6.1 range was conducted using an 85% training set and a 15% test set, defined by random resampling of the records. Residual analyses for both the classical model and the machine-learning model are compared with respect to hypocentral distance. As shown in Figure 5.3, the data points in the PGA and PGV plots are distributed evenly on both sides of the fit line. This is also confirmed by the mean values placed in the lower-right corner of the plots. The same pattern is observed at all other periods (Figure B.3). While the one-sigma estimates of the residuals for the classical GMPE remain around 0.7, those for the machine-learning–enhanced model are around 0.6. In other words, the parameters of the machine-learning–enhanced model lie closer to the zero line, indicating more stable predictions.

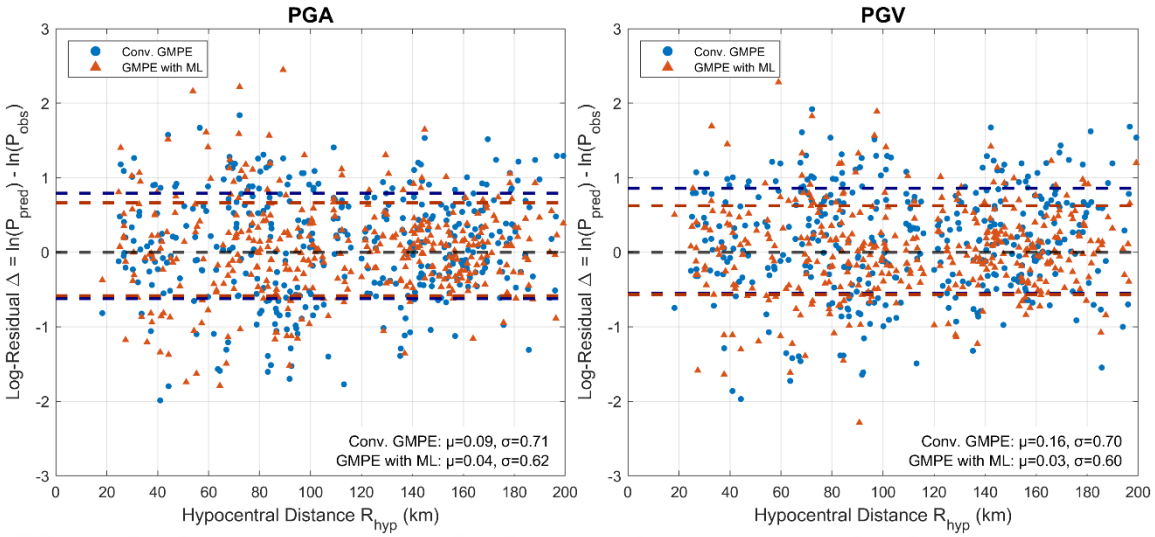

Figure 5.3. Residual analysis versus hypocentral distance for PGA and PGV.

For PGA and PGV, comparisons of ground-motion predictions from both models against the observational data are presented in Figure 5.4. Blue data points show predictions from the classical GMPE, and orange data points show predictions from the machine-learning–enhanced GMPE. These plots likewise indicate that the machine-learning–enhanced model performs better in prediction. A mean (μ) close to zero indicates the model does not exhibit systematic bias, while a smaller standard deviation (σ) implies a lower error margin and, therefore, reduced predictive uncertainty. The same analysis for all periods is provided in Figure B.4.

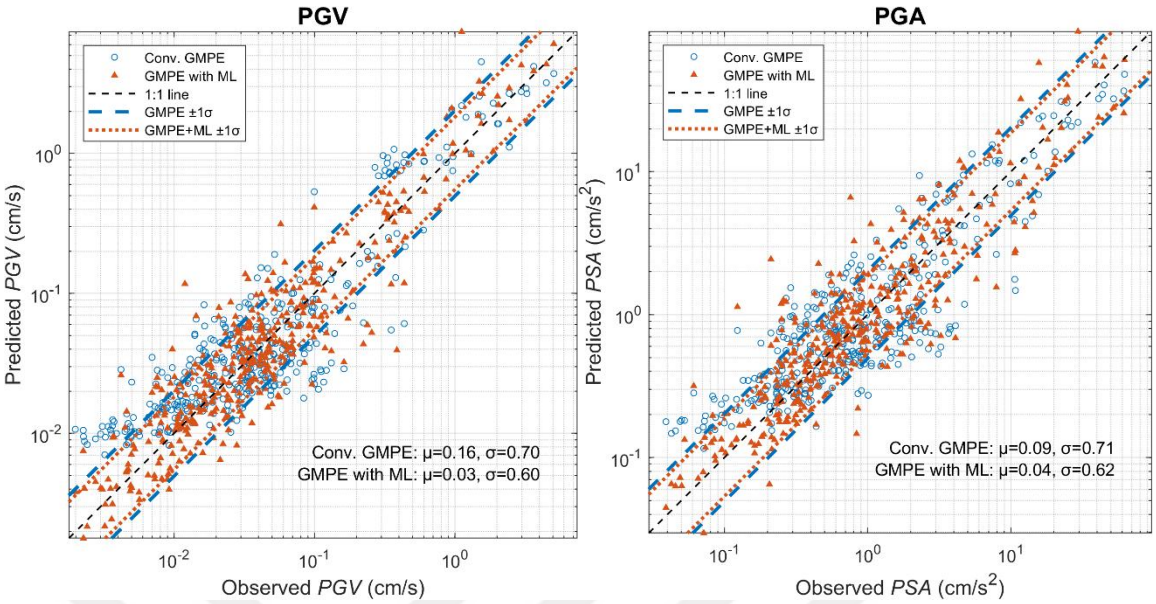

Figure 5.4. Comparisons of predicted and observed PGA and PGV.

5.1.10. Comparing the GMPE Models with Existing GMPEs

Final ground motion prediction models were evaluated against eleven established GMPEs to benchmark both the classical regression model and its ML-enhanced variant. The chosen models - Özbey et al. (2004), Boore and Atkinson (2008), Chiou and Youngs (2008), Akkar and Bommer (2010), Akkar and Çağnan (2010), Akkar et al. (2014), Boore et al. (2014), Campbell and Bozorgnia (2014), Kale et al. (2015), Kotha et al. (2020) and Sandıkkaya et al. (2023) were selected for their use of Turkish or analogous strike-slip regional datasets. Using the same 15 % test subset of RotD50 PGA, RotD50 PGV, and RotD50 PSA at 0.2, 0.5, 1, 2, and 4 s as before, we generated observed-versus-predicted plots. While Figure 5.5 and Figure 5.6 show the comparative plots for PGA and PGV, plots for the PSA can be found in Figure B.5, Figure B.6, Figure B.7, Figure B.8 and Figure B.9. Computed R^2 values for each model are presented in Table 5.2.

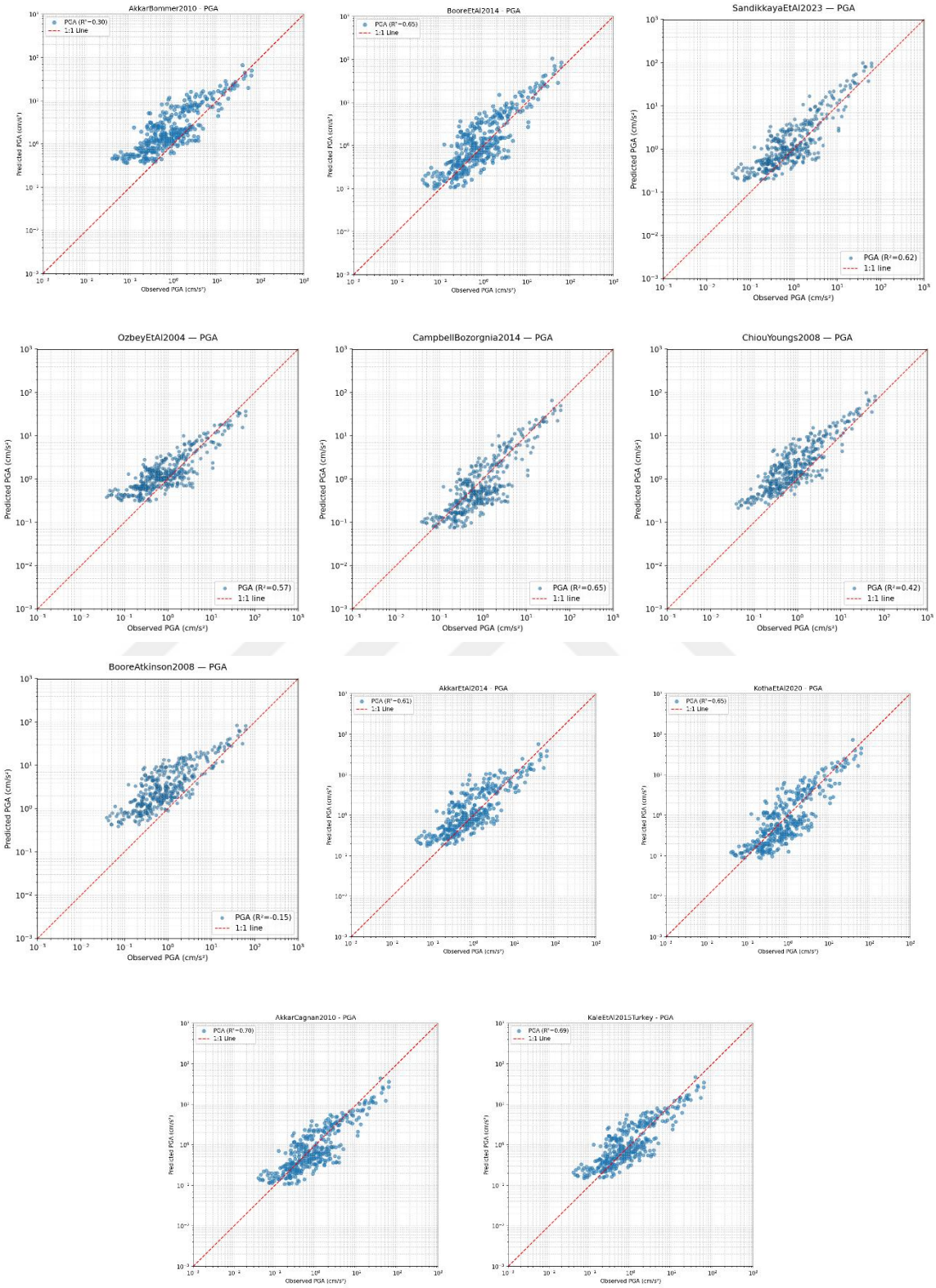

Figure 5.5. Predicted versus observed PGA, considering the GMPE model developed in this study and different GMPEs.

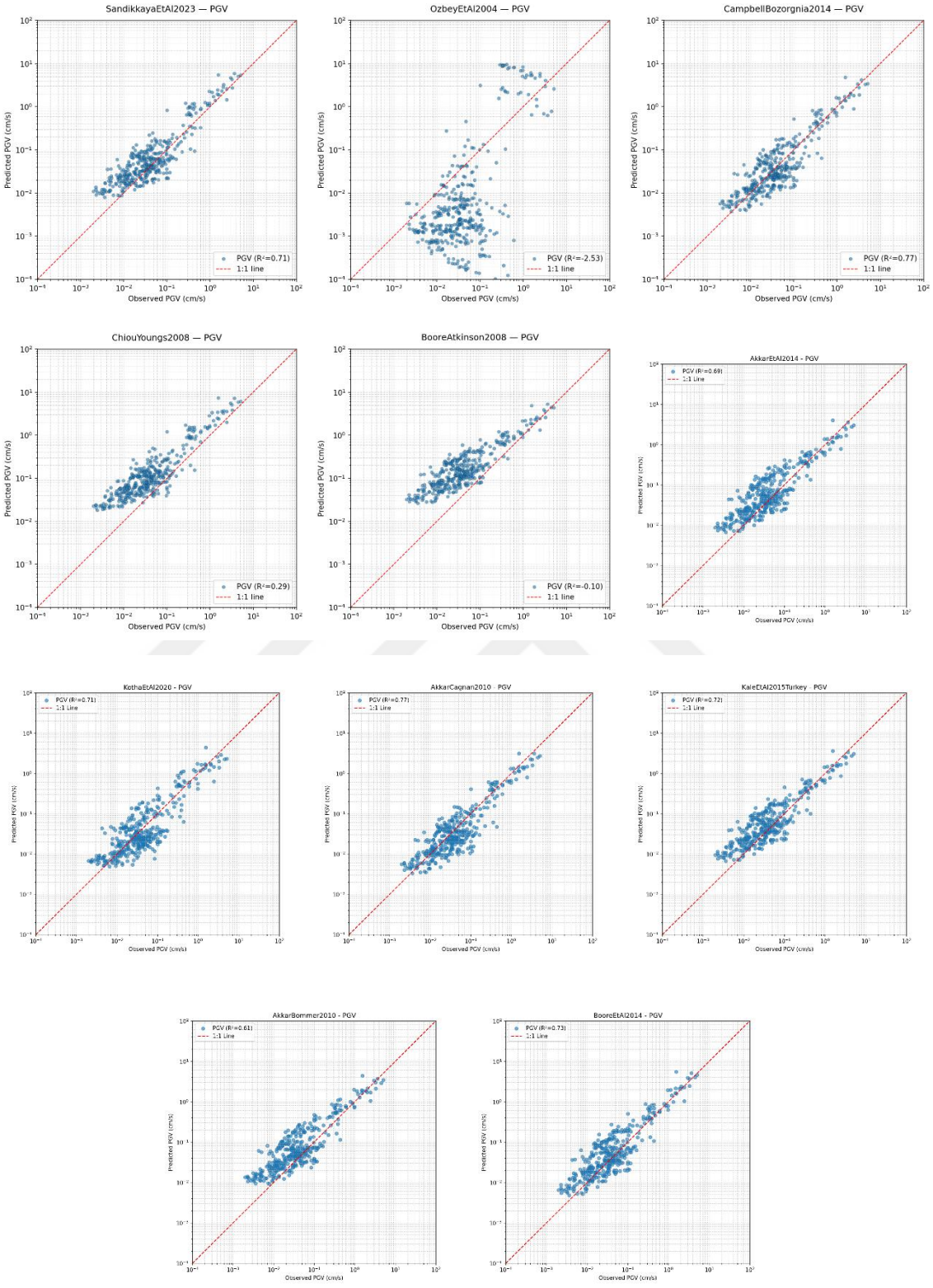

Figure 5.6. Predicted versus observed PGV, considering the GMPE model developed in this study and different GMPEs.

Table 5.2. R^2 estimations for observed versus predicted PGA, selected PSA and PGV values.

	PGV	PGA	SA at 0.2 s	SA at 0.5 s	SA at 1 s	SA at 2 s	SA at 4 s	Avg. R^2 score
This Study - Conventional GMPE with ML	**0.85**	**0.81**	**0.84**	**0.83**	**0.87**	**0.9**	**0.89**	**0.86**
This Study – Conventional GMPE	**0.78**	**0.75**	**0.72**	**0.74**	**0.77**	**0.81**	**0.84**	**0.77**
Akkar and Çağnan (2010)	0.77	0.7	0.67	0.75	0.78	0.84	-	0.75
Kale et al. (2015)	0.77	0.65	0.61	0.71	0.73	0.79	0.82	0.73
Cambell and Bozorgnia (2008)	0.73	0.65	0.64	0.7	0.74	0.78	0.76	0.71
Kotha et al (2020)	0.72	0.69	0.66	0.69	0.67	0.72	0.77	0.70
Boore et al. (2014)	0.71	0.62	0.66	0.68	0.71	0.76	0.76	0.70
Sandıkkaya et al. (2023)	0.67	0.61	0.64	0.68	0.68	0.71	0.78	0.68
Akkar et al. (2014)	0.71	0.65	0.62	0.64	0.66	0.72	0.76	0.68
Özbey et al. (2004)	-	0.57	0.67	0.66	0.65	0.32	0.54	0.57
Chiou and Youngs (2008)	0.61	0.3	0.38	0.6	0.72	0.71	0.37	0.53
Akkar and Bommer (2010)	0.29	0.42	0.47	0.54	0.56	0.6	0.72	0.51
Boore and Atkinson (2008)	-0.1	-0.15	-0.2	-0.33	-0.01	0.18	0.43	-0.03

The hybrid GMPE + ML model consistently outperformed its purely regression-based counterpart and most existing GMPEs across all spectral periods. For PGA and PGV, the ML-corrected model achieved R^2 values of 0.81 and 0.85 respectively, compared to 0.75 and 0.78 for the classical form. Up to 2 s, the Akkar and Çağnan (2010) model remained competitive with the pure GMPE ($R^2 \simeq 0.75$), but could not be extended beyond its 0.03–2 s range. In contrast, our ML-enhanced model not only maintains high accuracy to 5 s ($R^2 \approx$ 0.90 at 2 s and 0.89 at 4 s) but also delivers the best overall performance when averaged across all periods (avg. $R^2 = 0.86$). Among the other established GMPEs, Campbell and Bozorgnia (2014) retained strong predictive power (avg. $R^2 = 0.71$), while the Akkar and Bommer (2010) and Chiou and Youngs (2008) models lagged behind (avg. $R^2 = 0.51$ and 0.53, respectively). The Boore and Atkinson (2008) formulation proved unable to capture regional attenuation trends, registering negative R^2 values for several periods. These results underscore the benefit of augmenting a transparent, piecewise log-linear GMPE with a data-adaptive residual correction to achieve superior predictive capability over a broad spectral range.

5.1.11. Concluding Remarks

At this stage of the study, we have calibrated a piecewise log-linear GMPE by systematically scanning hinge distances (30–180 km) and hinge magnitudes (4.4–5.8) to maximize predictive accuracy. The two-stage regression decoupled distance and magnitude effects, and the nonlinear V_{S30} amplification term captured key soil behavior. This classical formulation provides a physically transparent model that reproduces the principal trends in observed ground motions across M_W 4.0–6.1 and hypocentral distances of 9–200 km.

To further reduce unexplained variance without altering the core functional structure, we trained a gradient-boosted regression-tree (GBRT) ensemble on the log-residuals of the classical GMPE, using only moment magnitude, logarithm of hypocentral distance, and V_{S30} as inputs. With 100 boosting iterations and a maximum of 20 splits per tree, the hybrid GMPE + ML model significantly increased the R^2 and lowered σ across all periods.

By combining a conventional GMPE with a data-adaptive residual correction, this hybrid approach offers both interpretability and enhanced predictive power. It therefore constitutes a robust framework for ground motion prediction across the target magnitude and distance ranges, and may readily accommodate new recordings through retraining of the residual ensemble without revisiting the underlying functional forms.

5.2. GMPE Modeling with Synthetic Ground-Motion Data

The ground-motion prediction equation developed using the synthetic dataset is based on broadband ground-motion simulations calibrated with region-specific physical parameters. Although the stochastic simulation method employed to build the synthetic dataset follow standard approaches described in the literature, they were comprehensively validated against real records from past earthquakes in the study area. During this validation, numerous physical parameters were optimized to maximize agreement between the simulation outputs and regional observational data. Consequently, the resulting synthetic dataset was designed to capture the regional physical variability of earthquakes together with site effects.

The constructed synthetic ground-motion dataset comprises more than one hundred thousand two-dimensional synthetic waveforms generated for a total of 18 earthquake scenarios spanning M_W 6.05–7.6. This dataset provides substantial diversity for GMPE development. The plot presented in Figure 5.7 shows the distributions of waveforms in both the real and synthetic ground-motion datasets with respect to magnitude and distance.

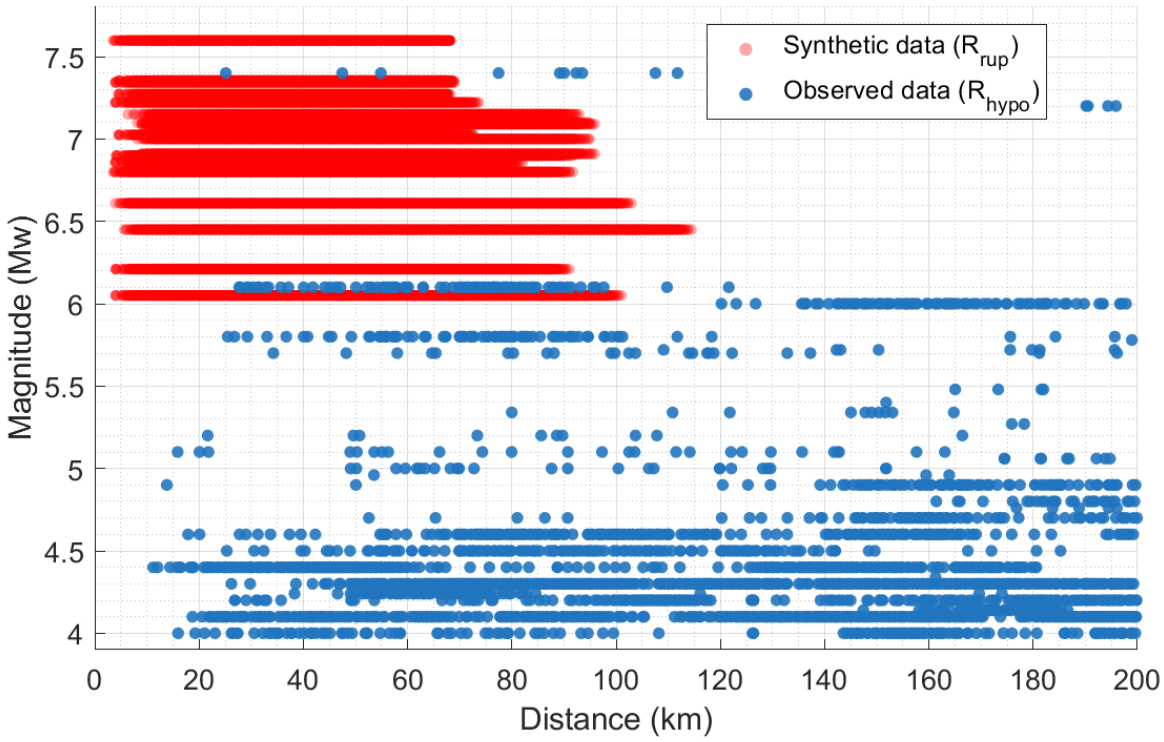

Figure 5.7. Comparison of magnitudes and distances in the synthetic and observational datasets.

Before proceeding with GMPE modeling, the consistency of the synthetic ground-motion parameters with the observed ground-motion parameters from real earthquakes was evaluated. Using the limited number of available records for events of $M_W \geq 6.0$ as a reference, a quantitative comparison was performed by examining the agreement between the synthetic and observational data. As can be seen in Figure 5.8, the distribution of the observational ground-motion data is relatively consistent with the synthetic dataset. These visuals also show greater scatter in the observational data; however, the observational and synthetic datasets appear to lie almost as continuations of one another.

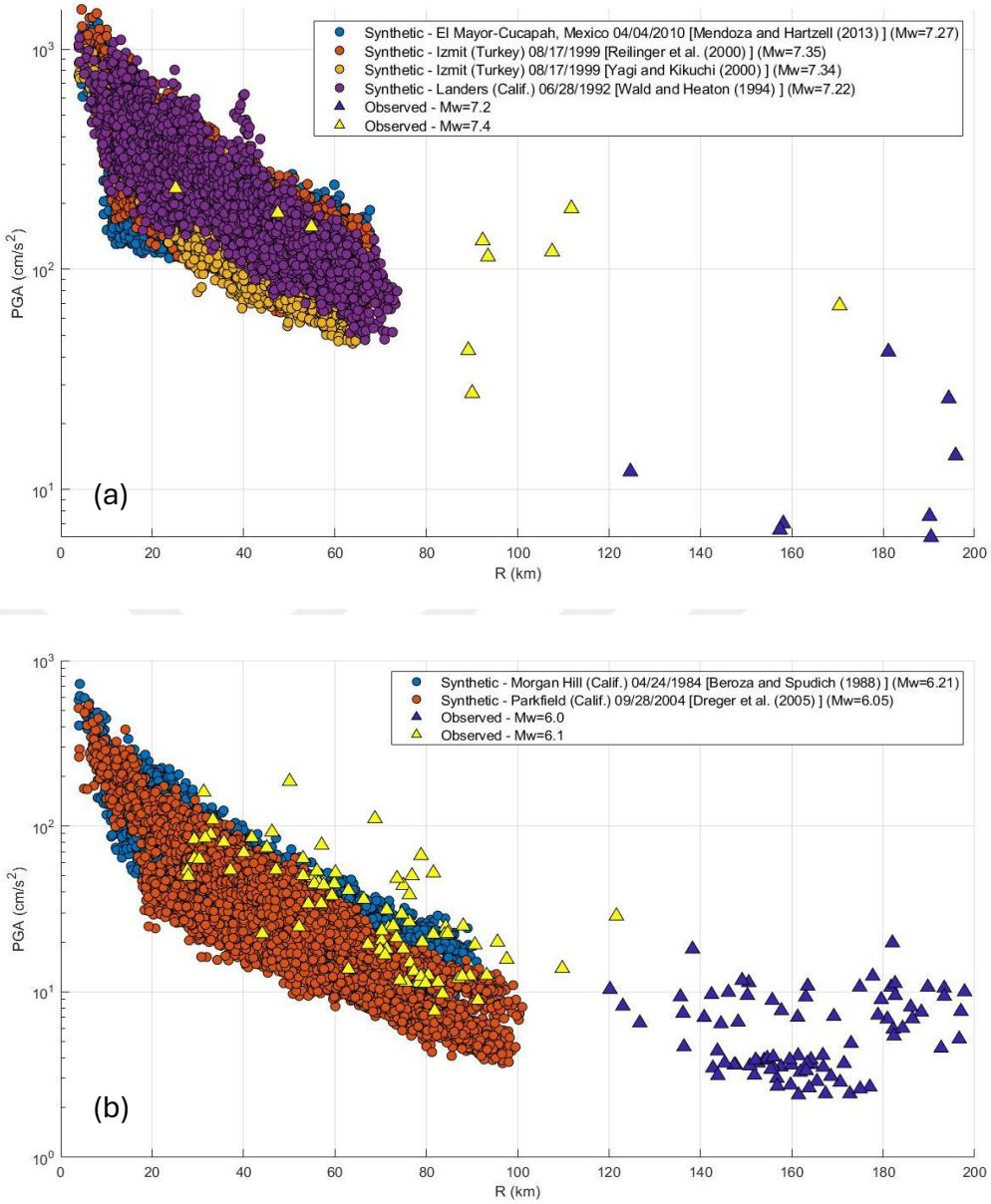

Figure 5.8. Comparison of (a) observational and synthetic data for M_W 7.2–7.4 range; (b) comparison for M_W 6.0–6.21 range.

In this study, the GMPE developed from real ground-motion records covers earthquakes in the M_W 4.0–6.1 range. The model constructed from the synthetic dataset spans M_W 6.05–7.6. The predictive domains of both models were constrained with respect to their covered magnitude and distance ranges. Accordingly, for the GMPE based on real data, the reliable prediction range was set to R_{hyp} = 10–200 km. For the model based on synthetic data, the applicable distance range is R_{rup} = 7–100 km for M_W 6.1–7.2 and R_{rup} =

7–60 km for M_W 7.2–7.6. Thus, the application domains of both models were optimized in line with data coverage and physical validity.

At the modeling stage, functional forms similar to those used for the real-data model were adopted. Because the distances in the synthetic data model are shorter, a single distance regression was used instead of the two-segment regression applied previously; therefore, the c_3 and c_4 coefficients were omitted. In addition, while R_{hyp} was used as the distance metric in the real-data model, R_{rup} is used here. The primary reason for using R_{rup} is that this dataset includes large earthquakes that produce extensive fault ruptures. M_W is set to M_W 6.3, that is an optimal value to produce the best-fit on the training dataset.

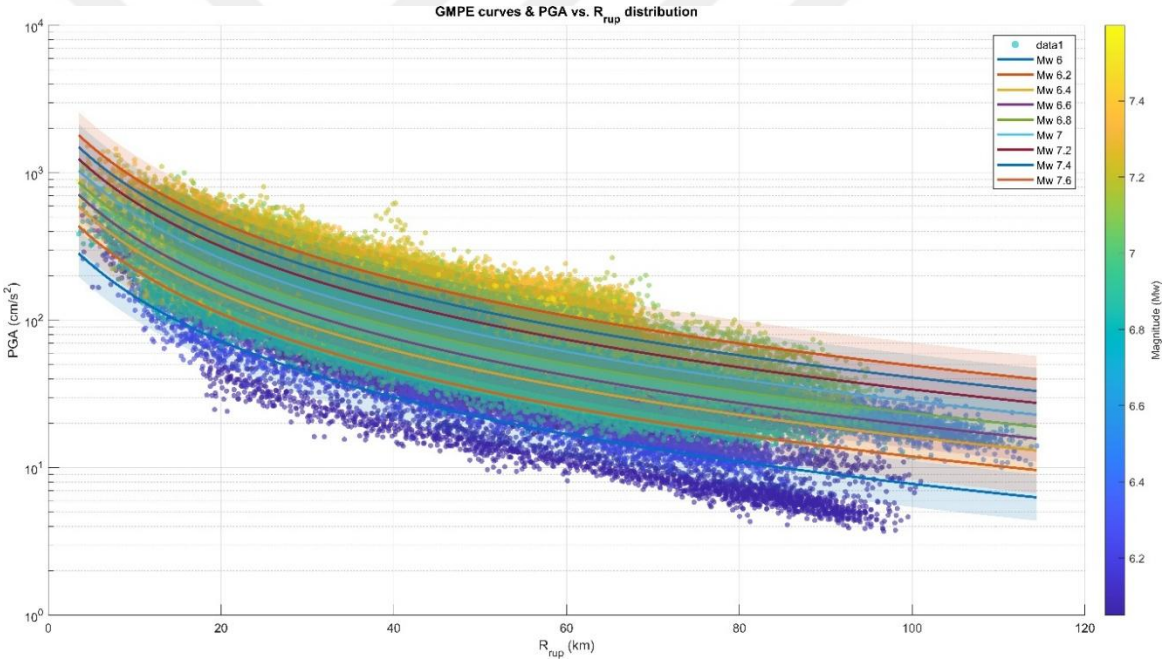

Figure 5.9. Distribution of the training dataset versus R_{rup} for PGA and selected PSA values; curves denote mean predictions for selected M_W values, shaded regions indicate the ±1-sigma range, and points represent individual records in the dataset.

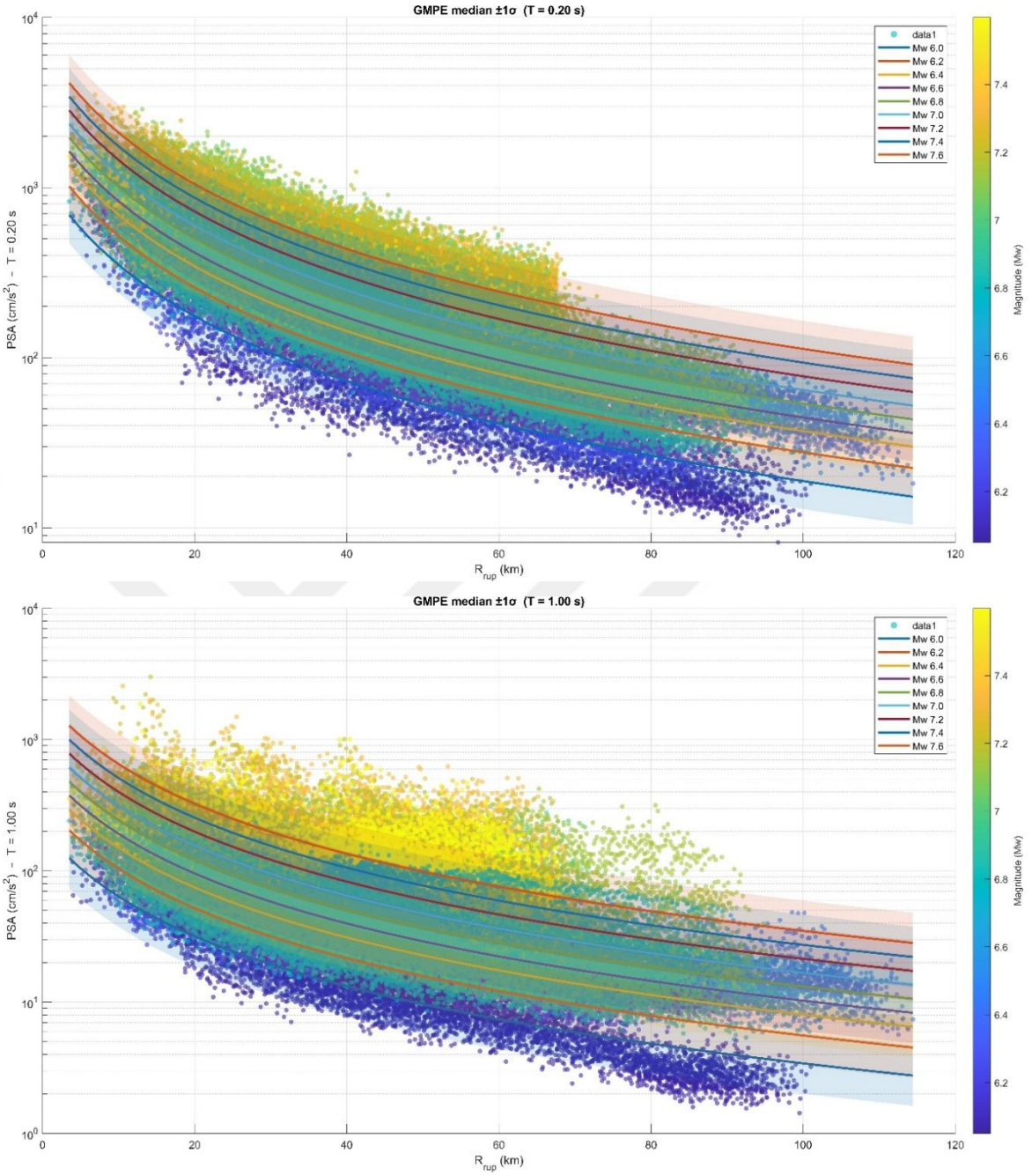

Figure 5.9. Distribution of the training dataset versus R_{rup} for PGA and selected PSA values; curves denote mean predictions for selected M_W values, shaded regions indicate the ±1-sigma range, and points represent individual records in the dataset (cont.).

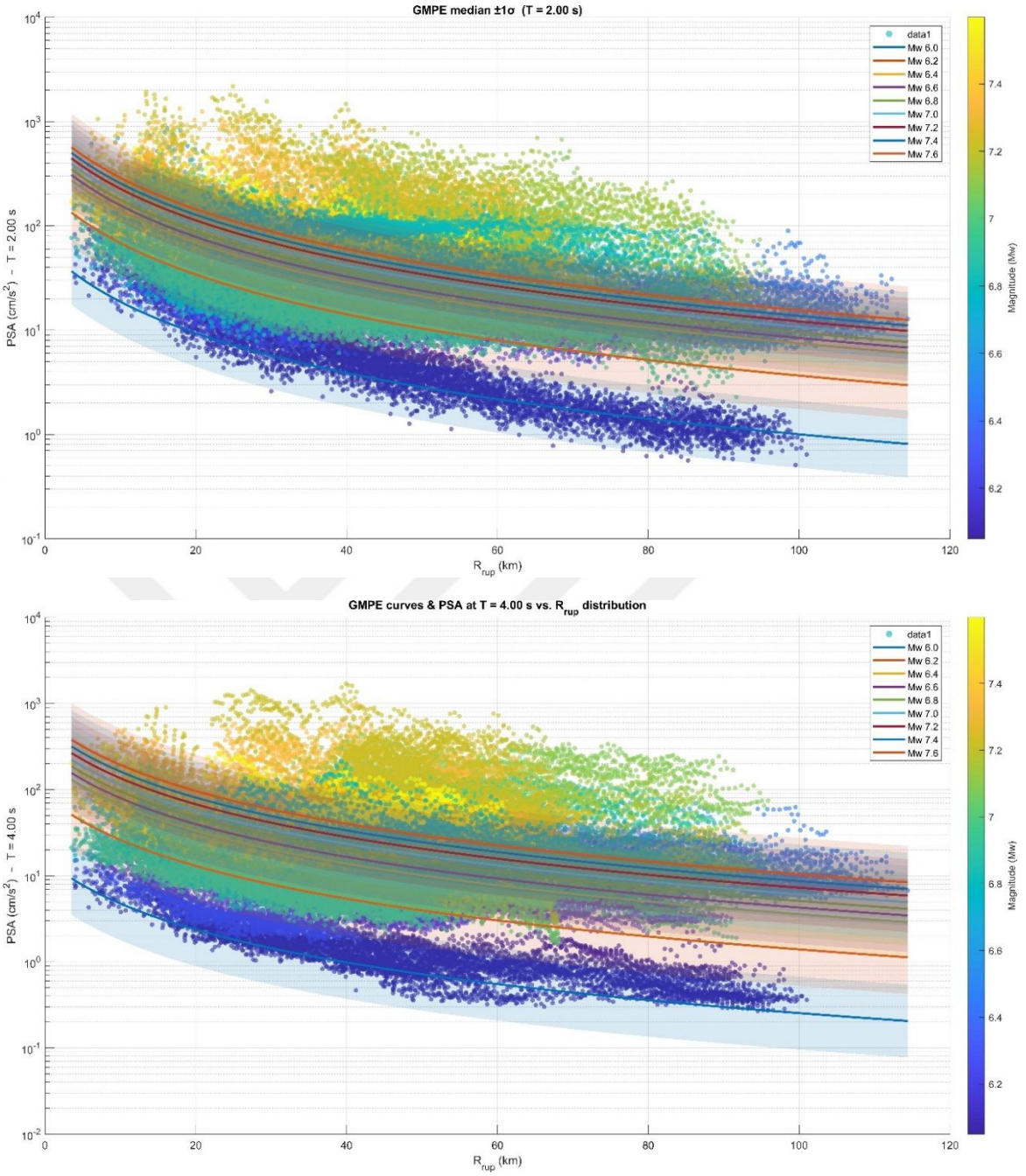

Figure 5.9. Distribution of the training dataset versus R_{rup} for PGA and selected PSA values; curves denote mean predictions for selected M_W values, shaded regions indicate the ±1-sigma range, and points represent individual records in the dataset (cont.).

Figure 5.9 presents the distribution of PGA and selected spectral accelerations versus R_{rup} in this dataset. The model's mean curves and the ±1-sigma bands (shown with semi-transparent shading) track the data consistently across all selected spectral accelerations. Each curve represents a different magnitude and is computed for the entire dataset's average

V_{S30} of 576 m/s. Similarly, the distribution of PGA and selected spectral accelerations versus M_W were also checked for visual confirmation of the data distribution compared to the GMPE curves (Figure 5.10). Both figures show good agreement between the model curves and the data distribution.

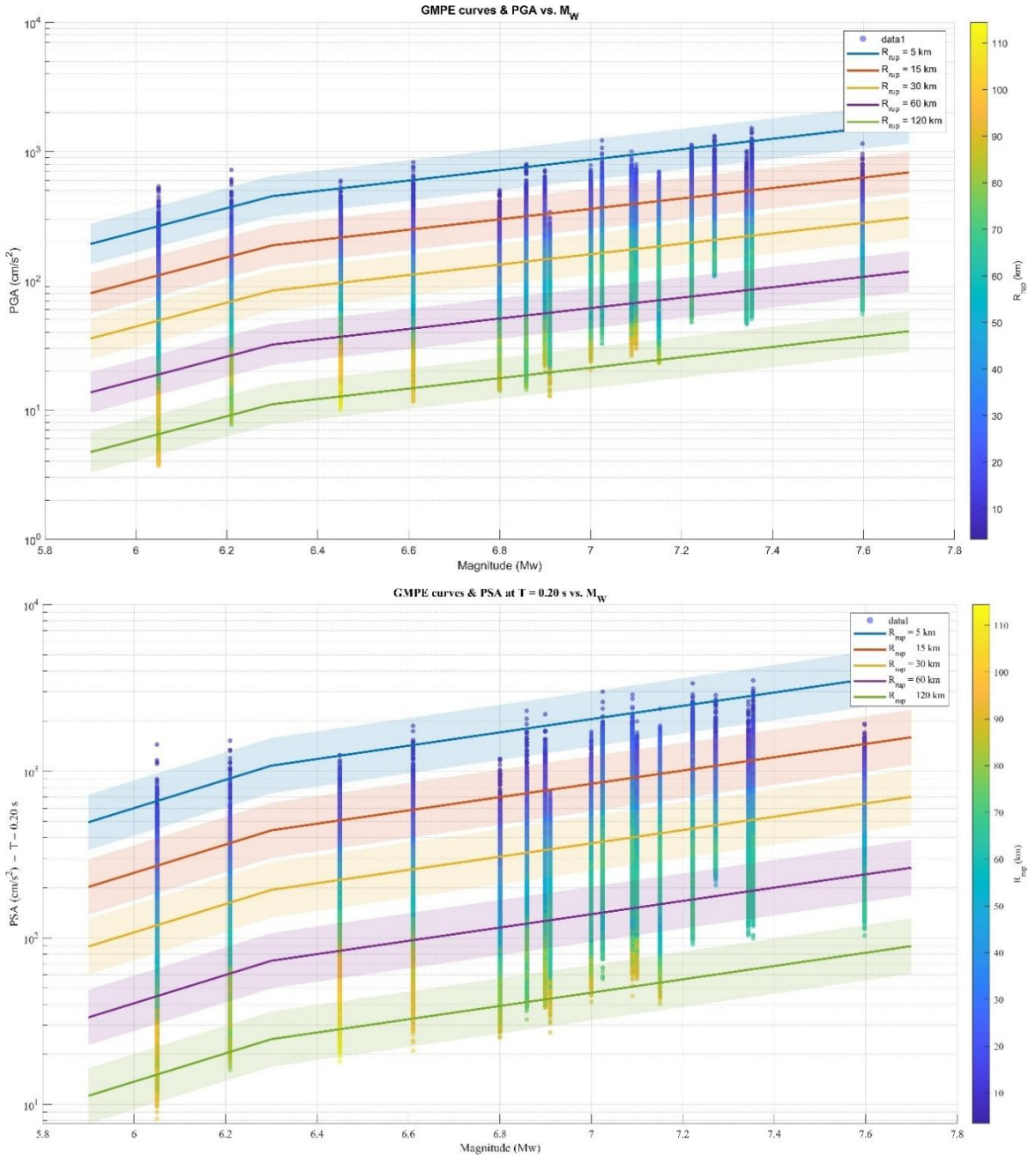

Figure 5.10. Distribution of the training dataset versus M_W for PGA and selected PSA values; curves denote mean predictions for selected R_{rup} values, shaded regions indicate the ±1-sigma range, and points represent individual records in the dataset.

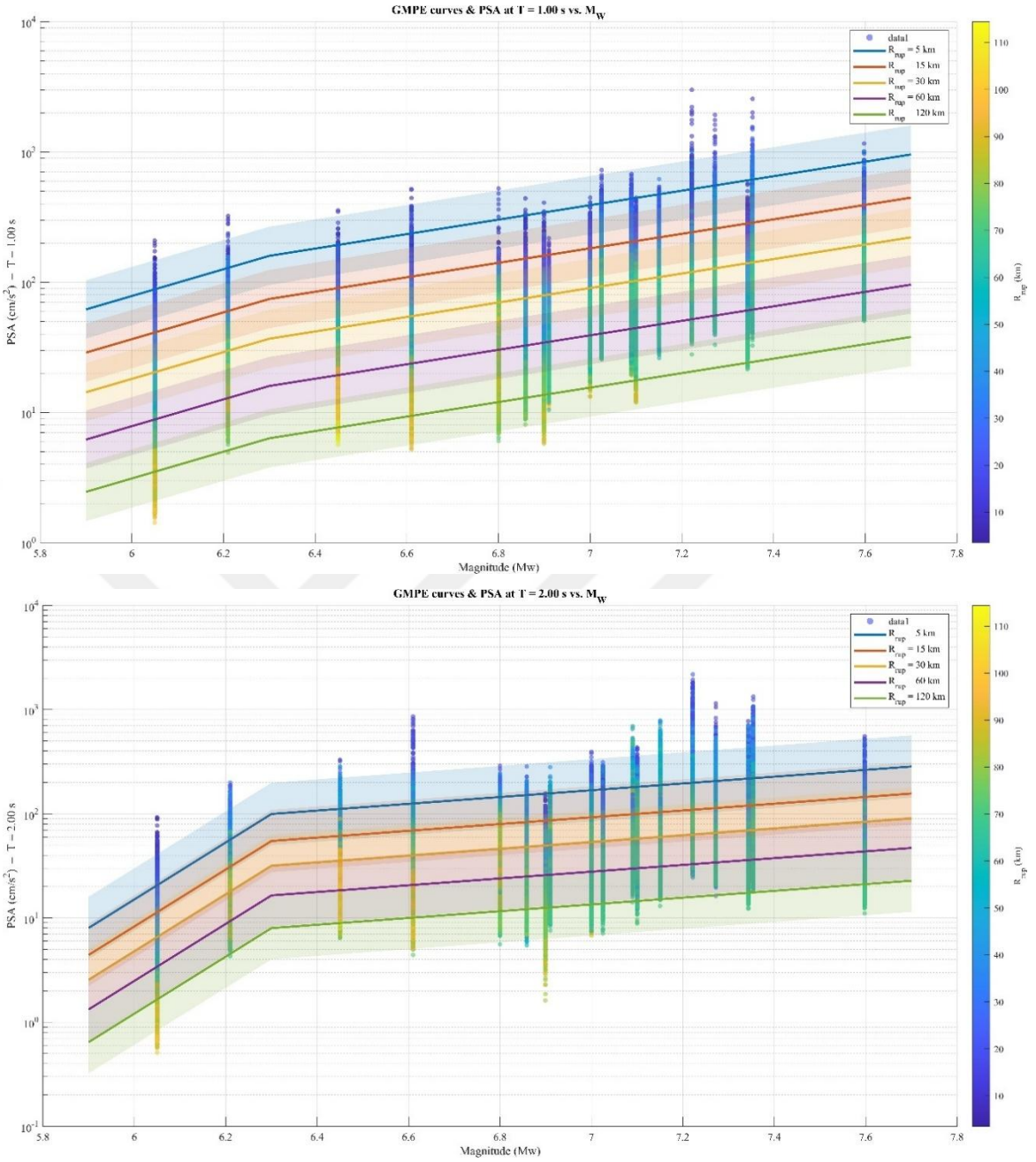

Figure 5.10. Distribution of the training dataset versus M_W for PGA and selected PSA values; curves denote mean predictions for selected R_{rup} values, shaded regions indicate the ±1-sigma range, and points represent individual records in the dataset (cont.).

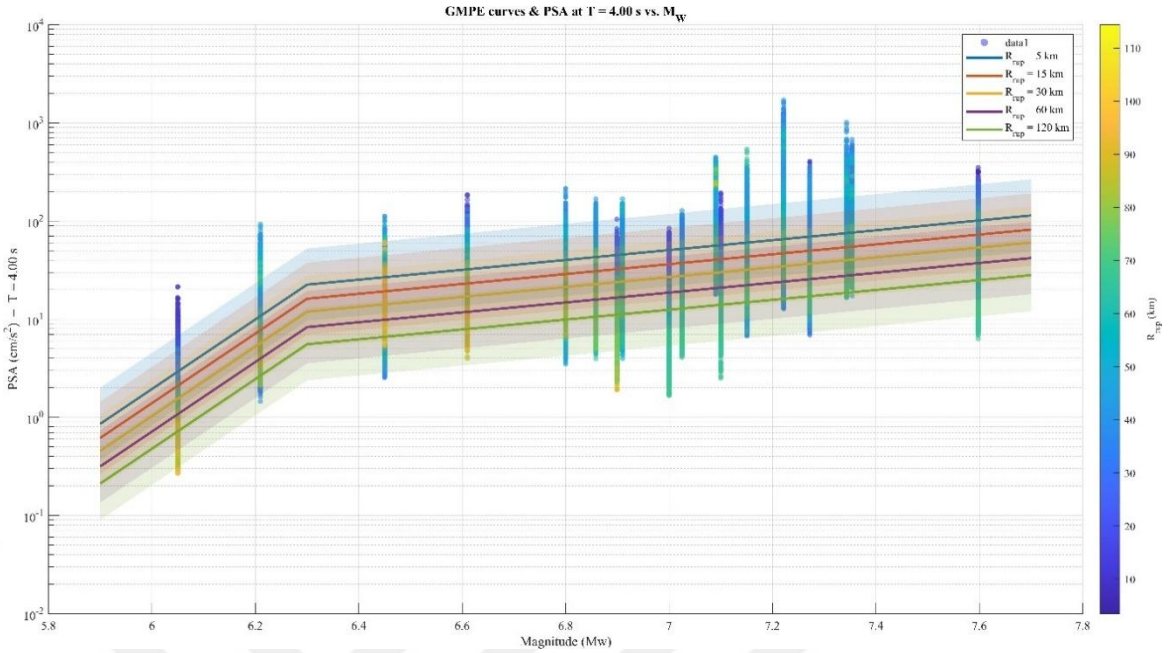

Figure 5.10. Distribution of the training dataset versus M_W for PGA and selected PSA values; curves denote mean predictions for selected R_{rup} values, shaded regions indicate the ±1-sigma range, and points represent individual records in the dataset (cont.).

Using the training set and NEHRP site classes (B: V_{S30}≥760, C: 360–760, D: 180–360 m/s), the model attains strong agreement in log-space at short periods, especially for classes C and D. At PGA, R^2 is 0.74 (B), 0.81 (C), and 0.82 (D) based on large and stable sample sizes (N=12,078 / 59,958 / 37,533). Across the short-period PSA range the fit remains high, with B and C peaking around T≈0.22–0.26 s (R^2≈0.74-75 for B and R^2 ≈0.82 for C), while D peaks near T≈0–0.1 s (R^2≈0.8-0.82). Performance diminishes with increasing period: by T=1 s, R^2drops to ~0.51–0.28 (B), ~0.64–0.42 (C), and ~0.78–0.63 (D), indicating that long-period scaling (magnitude/distance or nonlinear/site terms) leaves more unexplained variance, particularly for stiffer sites (B). At very long periods (T=3–5 s) the fits partially recover for B and C (e.g., B≈0.33–0.48, C≈0.41–0.49), and D remains comparatively robust (≈0.63–0.66). For PGV, the model explains less variance for B and C (0.46, 0.54) but remains strong for D (0.78). Overall, the model captures most of short-period variability, with systematic degradation toward longer periods that highlights targets for refinement. R^2 estimations for all periods, PGA and PGV can be seen in Table 5.3. Finally, the coefficients of the developed model are given in Table 5.4.

Table 5.3. Model agreement with training dataset quantified by R^2 estimations regarding NEHRP site classes.

T (s)	Site Class B	Site Class C	Site Class D
PGV	0.46	0.54	0.78
PGA	0.74	0.81	0.82
0.02	0.71	0.80	0.82
0.04	0.63	0.75	0.81
0.06	0.66	0.74	0.80
0.08	0.70	0.77	0.81
0.1	0.73	0.79	0.81
0.12	0.74	0.80	0.80
0.14	0.75	0.81	0.80
0.16	0.74	0.81	0.79
0.18	0.74	0.81	0.80
0.2	0.74	0.81	0.80
0.22	0.75	0.82	0.80
0.24	0.74	0.82	0.80
0.26	0.74	0.82	0.80
0.28	0.73	0.82	0.80
0.3	0.72	0.81	0.80
0.35	0.73	0.81	0.80
0.4	0.72	0.81	0.79
0.45	0.69	0.81	0.78
0.5	0.69	0.81	0.78
0.6	0.68	0.80	0.78
0.7	0.66	0.79	0.78
0.8	0.62	0.75	0.79
0.9	0.57	0.70	0.79
1	0.51	0.65	0.78
1.2	0.47	0.58	0.75
1.4	0.39	0.51	0.74
1.6	0.33	0.47	0.71
1.8	0.30	0.45	0.69
2	0.28	0.44	0.68
2.5	0.28	0.42	0.66
3	0.34	0.41	0.65
3.5	0.38	0.42	0.63
4	0.41	0.44	0.63
4.5	0.45	0.47	0.63
5	0.48	0.49	0.66

Table 5.4. Coefficients of the ground-motion prediction model.

	Distance-scaling coefficients		Magnitude-scaling coefficients				Site-amplification coefficients	
T(s)	**c_1**	**c_2**	**e_1**	**e_2**	**e_3**	**e_4**	**b_1**	**b_2**
PGV	6.847	-1.220	-27.988	4.353	0.974	46.228	-0.155	-0.027
PGA	11.341	-1.712	-14.004	2.131	0.931	17.255	-0.509	-0.076
0.02	11.450	-1.718	-14.207	2.163	0.934	12.456	-0.564	-0.103
0.04	11.779	-1.725	-14.553	2.216	0.952	10.889	-0.786	-0.178
0.06	12.070	-1.728	-14.303	2.176	0.954	15.569	-0.933	-0.176
0.08	12.216	-1.727	-13.465	2.042	0.962	8.505	-0.867	-0.131
0.1	12.294	-1.733	-13.641	2.074	0.929	12.664	-0.749	-0.098
0.12	12.337	-1.741	-13.915	2.119	0.911	13.220	-0.654	-0.072
0.14	12.361	-1.748	-13.958	2.127	0.905	14.326	-0.571	-0.052
0.16	12.345	-1.747	-13.313	2.023	0.915	13.386	-0.485	-0.036
0.18	12.343	-1.752	-12.910	1.958	0.918	5.875	-0.433	-0.023
0.2	12.304	-1.751	-12.898	1.957	0.919	10.378	-0.395	-0.016
0.22	12.251	-1.754	-13.205	2.006	0.908	11.134	-0.357	-0.012
0.24	12.241	-1.760	-13.454	2.046	0.908	4.662	-0.342	-0.007
0.26	12.215	-1.760	-12.900	1.958	0.910	4.839	-0.318	-0.003
0.28	12.186	-1.762	-12.262	1.857	0.899	8.252	-0.289	-0.002
0.3	12.168	-1.765	-11.813	1.784	0.915	10.439	-0.260	0.001
0.35	12.091	-1.771	-12.500	1.891	0.937	13.694	-0.246	0.009
0.4	11.978	-1.767	-12.581	1.904	0.940	14.134	-0.213	0.014
0.45	11.865	-1.758	-12.670	1.920	0.923	9.963	-0.188	0.019
0.5	11.758	-1.754	-12.490	1.889	0.943	7.781	-0.155	0.020
0.6	11.524	-1.743	-12.430	1.873	1.007	4.349	-0.122	0.023
0.7	11.244	-1.716	-13.239	1.998	1.044	11.945	-0.104	0.022
0.8	10.797	-1.651	-13.275	1.994	1.135	12.406	-0.088	0.018
0.9	10.392	-1.587	-13.833	2.071	1.245	-24.025	-0.090	0.018
1	9.915	-1.494	-15.729	2.369	1.280	14.248	-0.082	0.019
1.2	9.294	-1.364	-17.381	2.620	1.395	14.156	-0.047	0.015
1.4	8.935	-1.314	-25.155	3.890	1.093	30.739	-0.044	0.003
1.6	8.485	-1.226	-32.388	5.064	0.876	22.556	-0.035	0.002
1.8	8.282	-1.191	-36.440	5.718	0.795	-23.157	0.021	-0.002
2	8.145	-1.168	-40.070	6.301	0.749	29.159	0.075	-0.008
2.5	7.645	-1.070	-48.091	7.584	0.692	30.372	0.093	-0.021
3	7.008	-0.951	-53.939	8.508	0.752	-54.208	0.074	-0.036
3.5	6.240	-0.798	-53.800	8.465	0.951	35.945	0.059	-0.032
4	5.484	-0.648	-52.048	8.165	1.158	52.132	-0.003	-0.019
4.5	4.987	-0.566	-49.876	7.805	1.291	52.140	-0.061	-0.009
5	4.781	-0.566	-48.458	7.570	1.373	43.273	-0.064	0.002

At this stage, unlike the previous one, machine learning was not used. Although the synthetic dataset comprises records simulated at thousands of sites and provides broad coverage in terms of R_{rup}, V_{S30}, and M_W, such data are tightly bound to the same simulation algorithms and assumptions calibrated with shared physical parameters. As a result, a machine-learning model trained on this dataset is unlikely to demonstrate genuine generalization; these models are best suited to datasets that directly reflect real-world complexity. In the context of this study, evaluating a GMPE trained on synthetic data against a hold-out synthetic subset has limited evidential value: because both the training and validation sets are generated by the same physical model and parameter assumptions, such testing mainly quantifies self-consistency with the simulation rather than true generalization. The meaningful criterion is predictive skill for real earthquakes, which can be assessed only with independent observational records. However, the regional dataset contains few recordings from large events, preventing statistically robust validation. Consequently, the reliability and predictive capacity of this GMPE trained on synthetic data fundamentally rests on the previous regional validation of the simulation models.

6. SPATIAL CORRELATION MODEL DEVELOPMENT

The spatial correlation of ground-motion intensities is a fundamental aspect of seismic hazard analysis. It is necessary to quantify the relationship between ground-motion intensities at various locations during a single seismic event. The methodology employed here follows the framework established by Jayaram and Baker (2009) and builds on prior approaches for modeling spatial correlation in ground motions, such as those developed by Goda and Atkinson (2010) and Esposito and Iervolino (2012). The latter study investigated the spatial correlation of PSA values in European ground-motion data, emphasizing how regional differences in site conditions and seismic sources influence correlation structures. Their findings stress the importance of tailoring spatial correlation models to regional characteristics, a concept that is critical when applying these models to areas such as Istanbul.

6.1. Theoretical Framework of Spatial Correlation

Ground-motion prediction equations provide estimates of median ground-motion intensities at specific locations. These models decompose observed ground motions into three primary components as

$$\ln(Y_{ij}) = ln(\overline{Y_{ij}}) + \epsilon_{ij} + \eta_j. \tag{6.1}$$

In this equation, Y_{ij} represents the observed ground motion at site i during earthquake j, while $\overline{Y_{ij}}$ is the median ground motion predicted by the GMPE. The term ϵ_{ij} captures the intra-event residuals, which reflect site-specific deviations from the median, and η_j represents the inter-event residuals, which account for event-wide deviations. The focus of spatial correlation modeling is the intra-event residuals, ϵ_{ij}, treated as a spatially distributed random variable.

In this work we model the semivariogram of within-event residuals without variance normalization; therefore the sill is estimated from the data and need not equal 1.

6.1.1. Constructing the Semivariogram

The spatial correlation structure of normalized intra-event residuals is characterized using semivariograms. A semivariogram measures the dissimilarity between data points as a function of their separation distance h. The theoretical semivariogram is expressed as

$$\gamma(h) = \frac{1}{2} E\left[\left(Z(u) - Z(u+h)\right)^2\right], \tag{6.2}$$

where, Z(u) and Z(u+h) represent the random variables corresponding to normalized intra-event residuals at locations separated by distance h. Under the assumption of stationarity, γ(h) depends only on the separation distance and not on the absolute positions of the data points, ensuring consistency and reliability in subsequent analyses.

The experimental semivariogram is computed from observed data as

$$\hat{\gamma}(h) = \frac{1}{2N(h)} \sum_{\alpha=1}^{N(h)} \left(Z(u_\alpha) - Z(u_\alpha + h)\right)^2 , \tag{6.3}$$

where N(h) is the number of site pairs separated by a distance h. These experimental estimates provide discrete values of γ(h) for predefined distance bins.

6.1.2. Deriving the Spatial Correlation Function

The spatial correlation function $\rho(h)$ is derived directly from the semivariogram as

$$\rho(h) = 1 - \frac{\gamma(h)}{n+a} , \tag{6.4}$$

where *n* is the nugget and *a* is the partial sill. For the exponential model with range parameter L_{corr}, $\gamma(h)$ is

$$\gamma(h) \;=\; n + a\left(1 - e^{-\frac{3h}{L_{\text{corr}}}}\right). \tag{6.5}$$

This correlation function describes the relationship between intra-event residuals as a function of separation distance, forming the foundation for simulating spatially correlated ground-motion fields.

6.1.3. Predictive Models

Jayaram and Baker (2009) proposed predictive equations for the range L_{corr} of the exponential semivariogram, expressed as functions of spectral period T:

For short periods ($T < 1s$),

$$L_{\text{corr}} = 8.5 + 17.2T \quad \text{(Case 1)}\ , \tag{6.6}$$

$$L_{\text{corr}} = 40.7 - 15.0T \ \text{(Case 2)}\ . \tag{6.7}$$

For long periods ($T \geq 1s$)

$$L_{\text{corr}} = 22.0 + 3.7T\ . \tag{6.8}$$

Case 1 applies when the region exhibits significant variability in site conditions, such as non-clustered V_{S30} values, while Case 2 is used for areas with more homogeneous site conditions. In this study, the correlation range parameter L_{corr} is not expressed through a regression relationship with spectral period, as was done in some earlier works. Instead, L_{corr} is directly estimated for each individual period from the empirical semivariogram fits. This approach avoids imposing a functional form across periods and allows the data to reveal period-by-period variability in spatial correlation.

6.1.4. Assessing Isotropy

An isotropic semivariogram assumes that $\gamma(h)$ depends only on the separation distance h, irrespective of direction. To verify isotropy, directional semivariograms are computed for specific azimuths (e.g., 0°, 45°, 90°) and compared to the omni-directional semivariogram. Significant directional variations indicate anisotropy, necessitating adjustments to the model. We adopt an isotropic model in this study; directional semivariograms were not pursued due to uneven azimuthal coverage and are left as future work.

6.2. Analysis and Results

6.2.1. Empirical Semivariogram Analysis

The development of a spatial correlation model began with the calculation of the empirical semivariogram from aggregated station-level residuals. The semivariogram, a

geostatistical tool, quantifies spatial variability by measuring the dissimilarity of residuals as a function of station separation distance.

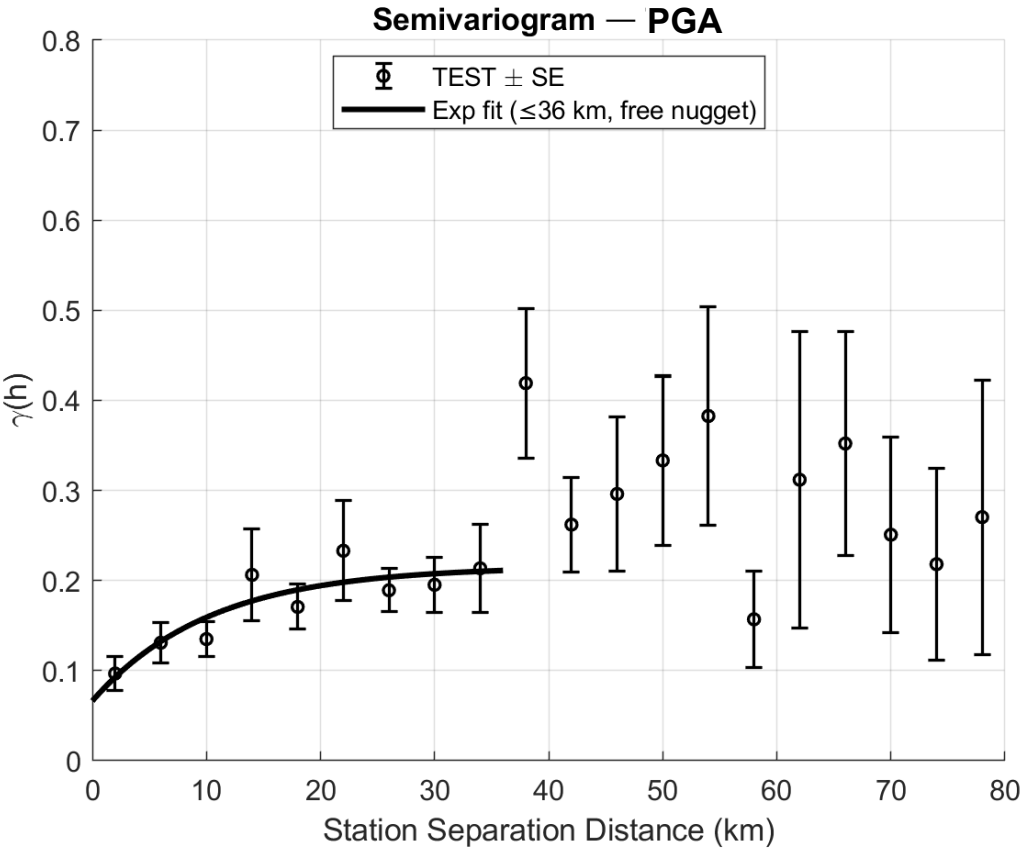

Figure 6.1. Empirical semivariogram for PGA; circles represent mean values, while error ranges show ±1 standard deviation at distance bins.

The empirical semivariogram, shown in Figure 6.1, was developed using the residuals calculated by utilizing the test-set portion of the observed ground motion dataset, against the real-data only GMPE calibrated separately on the training subset of the observed ground motions to avoid bias. Residuals were converted into within-event, site-centered residuals (δW) by removing the event term for each earthquake, ensuring that only intra-event variability was analyzed. For each event, unique stations coordinates were used to compute distances.

Station pairs were binned in intervals of 4 km, and the mean semivariogram value was calculated in each bin as the average of $0.5(\delta W_i - \delta W_j)^2$. Standard errors were also

estimated to quantify the uncertainty of each bin. To provide context, empirical semivariogram points are displayed for station separations up to 80 km. However, the subsequent theoretical model fitting is restricted to distances of 36 km or less, where data coverage is denser and variability estimates are more reliable.

6.2.2. Theoretical Model Fitting

To characterize the spatial dependence of residuals, an exponential semivariogram model was fitted to the empirical estimates. The fitting procedure was carried out using only station separations ≤ 36 km, reflecting the range of distances with sufficient data density and reduced scatter. At greater distances, especially beyond 40–50 km, the empirical semivariogram exhibited substantial irregularities due to fewer station pairs and increased uncertainty, and was therefore excluded from the model calibration.

The exponential form was selected in accordance with previous studies (Jayaram and Baker, 2009; Esposito and Iervolino, 2012), as it provides a physically interpretable representation of short-range correlations in ground-motion residuals as

$$\gamma(h) = n + a\left[1 - \exp\left(-\frac{3h}{L_{\text{corr}}}\right)\right], \tag{6.9}$$

where n denotes the nugget, a the sill, and L_{corr} the correlation range parameter. The current analysis treats the nugget as a free parameter, thereby accounting for uncorrelated short-range variability such as measurement noise and site-specific effects.

The current study adopts the exponential model exclusively. This decision is supported both by literature and by the improved stability of fits when applied consistently across periods. The model fitting was performed separately for PGA, PGV and all PSA, with the full set of coefficients (nugget, sill, range) reported in Table 6.1.

A representative semivariogram is shown in Figure 6.1, while semivariograms for all other periods and PGV are provided in the Appendix. As expected, the fitted range parameter b generally decreases with increasing frequency (shorter periods), indicating stronger short-distance correlation at high frequencies. Conversely, at longer periods the empirical data exhibit more scatter and weaker correlation.

Overall, the fitted exponential model demonstrates that the effective correlation distance in the study region is on the order of 30–35 km, broadly consistent with previous empirical findings for other regions (Jayaram and Baker, 2009; Goda and Atkinson, 2010; Esposito and Iervolino, 2012).

Table 6.1. Fitted model parameters for PGA, PGV and all PSA.

T (s)	n	a	L_{corr}
PGV	0.08	0.19	37.8
PGA	0.07	0.15	30.9
0.02	0.07	0.15	32.6
0.04	0.08	0.15	50.4
0.06	0.09	0.19	91.2
0.08	0.11	0.10	39.1
0.1	0.08	0.11	17.4
0.12	0.07	0.12	11.9
0.14	0.11	0.08	20.2
0.16	0.02	0.17	10.6
0.18	0.00	0.22	9.1
0.2	0.03	0.23	10.1
0.22	0.10	0.18	16.3
0.24	0.09	0.20	23.8
0.26	0.11	0.17	29.0
0.28	0.11	0.18	26.8
0.3	0.08	0.22	19.4
0.35	0.10	0.20	19.8
0.4	0.18	0.15	36.2
0.45	0.21	0.18	59.0
0.5	0.18	0.17	29.5
0.6	0.14	0.20	23.5
0.7	0.09	0.24	26.7
0.8	0.06	0.27	29.1
0.9	0.02	0.34	31.7
1	-0.11	0.39	39.2
1.2	-0.01	0.34	33.5
1.4	-0.17	0.39	48.8
1.6	-0.04	0.42	55.9
1.8	0.03	0.46	76.4
2	-	-	-
2.5	-	-	-
3	-	-	-
3.5	-	-	-
4	-	-	-
4.5	-	-	-
5	-	-	-

6.2.3. Interpretation of Results

The fitted exponential models provide new insights into the spatial correlation structure of ground-motion residuals in the study region. Table 6.1 summarizes the estimated coefficients (nugget, sill, and range) across all periods, while Figure 6.1 shows the representative semivariogram for PGA. Additional semivariograms for PGV and all spectral periods are presented in the Figure C.1.

A key outcome of this analysis is the recognition of period-dependent stability in the semivariogram structure. For short periods (up to approximately 1 s), the empirical semivariograms exhibit a relatively coherent trend up to 35 km, with exponential fits capturing both the initial rise and the approach toward the sill. Beyond 1 s, however, the semivariograms become more scattered even within the 0–35 km range, reducing confidence in the fitted parameters. Especially beyond ~1.8 s the empirical semivariograms are too scattered to constrain sill and range reliably. This observation suggests that while short-period motions exhibit consistent correlation patterns over the near-field scale, longer-period motions are subject to stronger variability, possibly linked to path effects in the heterogeneous crustal structure beneath the Marmara region.

The nugget terms are non-zero across most periods, reinforcing the presence of uncorrelated, small-scale variability that cannot be attributed to spatial distance. This may reflect station-specific effects, site-response irregularities, or residual noise in recordings. The sill values capture the overall variance of normalized residuals and remain stable across most periods under ~1 s, though with larger uncertainty for long periods. The range parameter is generally within 30–35 km, confirming that spatial correlation of intra-event residuals is significant up to this distance but decays rapidly thereafter.

Taken together, these findings align with previous regional and global studies (Jayaram and Baker, 2009; Esposito and Iervolino, 2012) but provide a tailored characterization for Istanbul and the Marmara region. The results highlight that while spatial correlation models developed elsewhere may offer broad guidance, region-specific calibration is essential.

7. CONCLUSIONS

This work developed and evaluated ground-motion prediction models for the Istanbul region using two complementary datasets of real and simulated ground motions and modeling strategies. For the observed recordings, a three-stage GMPE was built with explicit distance attenuation, magnitude scaling, and a nonlinear site term. On top of this baseline, a gradient-boosted ensemble was trained on residuals to capture systematic effects not explained by the parametric form. For the synthetic motions, a physics-informed GMPE was formulated. These frameworks were applied over the same period range of 0.02-5 s for RotD50 PSA, as well as for RotD50 PGA, and RotD50 PGV.

Across the majority of spectral periods, the ML-enhanced model reduced predictive error relative to the classical GMPE on held-out observed data, while preserving the interpretability of the baseline coefficients. The hybrid approach therefore offers a practical balance: a transparent physical backbone augmented by data-driven correction that is easy to retrain as new observations arrive.

The synthetic GMPE produced stable, physically plausible median curves and dispersion across the target magnitude–distance space. These attributes make the synthetic model a useful tool for supplementing observational gaps, particularly at large magnitudes and distances that are under-represented in the recordings.

Broadband mapping of ground-motion intensity illuminated period-dependent spatial patterns. At short periods around 0.3 s, higher amplitudes aligned with stochastic simulations, whereas at 1–3 s the 3D physics-based simulations better captured longer-period amplification. The regional contrast between the European and Asian sides of Istanbul varied with period and magnitude scenario, underscoring the importance of frequency-dependent path and site effects when translating hazard to risk metrics.

Spatial correlation was examined through semivariograms computed in consistent 4-km bins. These summaries showed reasonable short-range variability and ranges that are compatible with dense urban arrays, but they were not the main driver of model selection.

The combined results support several practical conclusions. First, a well-specified classical GMPE remains a strong baseline for the region; careful distance segmentation, magnitude breaking, and a calibrated nonlinear site term are crucial. Second, residual learning is a reliable way to capture remaining structure in observed data without sacrificing interpretability, provided that training and evaluation are separated and event de-meaning is enforced. Third, synthetic motions—when generated and filtered consistently—add real value by stabilizing trends and extending coverage, and their dedicated GMPE can be maintained alongside the observational model rather than merged prematurely.

Future refinements should prioritize better constraints on site conditions and path proxies that are known to be spatially structured, expanded out-of-fold or time-split validation to guard against drift, and tighter coupling between physics-based simulation parameters and the residual terms learned by the ML layer. Incorporating basin metrics, anisotropic correlation, and robust semivariogram estimators would further improve spatial consistency, but these should follow continued emphasis on predictive skill and transparent uncertainty quantification.

Overall, the study delivers a coherent, reproducible pipeline: high-quality data curation, GMPE development for observed and synthetic datasets, careful validation, and regionally relevant mapping of ground-motion intensity. This framework is immediately usable for hazard and risk studies in Istanbul, and it can be updated with minimal friction as new recordings and improved simulations become available.

REFERENCES

Abrahamson, N. A., Silva, W. J., and Kamai, R., 2014, Summary of the ASK14 ground-motion relation for active crustal regions. *Earthquake Spectra, 30*(3), 1025–1055.

Akinci, A., D'Amico, S., Malagnini, L., and Mercuri, A., 2013, Scaling earthquake ground motions in western Anatolia, Turkey. *Physics and Chemistry of the Earth, Parts A/B/C*, *63*, 124-135.

Akkar, S., and Bommer, J. J., 2010, Empirical equations for the prediction of PGA, PGV, and spectral accelerations in Europe, the Mediterranean region, and the Middle East. *Seismological Research Letters, 81*(2), 195-206.

Akkar, S., and Çağnan, Z., 2010, A local ground-motion predictive model for Turkey, and its comparison with other regional and global ground-motion models. *Bulletin of the Seismological Society of America, 100*(6), 2978-2995.

Akkar, S., Sandıkkaya, M. A., and Bommer, J. J., 2014, Empirical ground-motion models for point-and extended-source crustal earthquake scenarios in Europe and the Middle East. *Bulletin of Earthquake Engineering, 12*, 359-387.

Ambraseys, N. N., 2002, Seismic sea-waves in the Marmara Sea region during the last 20 centuries. *Journal of Seismology, 6*, 571-578.

Anderson, J. G., and Hough, S. E., 1984, A model for the shape of the Fourier amplitude spectrum of acceleration at high frequencies. *Bulletin of the Seismological Society of America, 74*(5), 1969-1993.

Armijo, R., Meyer, B., Navarro, S., King, G., and Barka, A., 2002, Asymmetric slip partitioning in the Sea of Marmara pull-apart: A clue to propagation processes of the North Anatolian fault? *Terra Nova, 14*(2), 80-86.

Assatourians, K., and Atkinson, G. M., 2007, Modeling variable-stress distribution with the stochastic finite-fault technique. *Bulletin of the Seismological Society of America, 97*(6), 1935-1949.

Atkinson, G. M., and Boore, D. M., 1995, Ground-motion relations for eastern North America. *Bulletin of the Seismological Society of America, 85*(1), 17–30.

Barka, A. A., 1997, Neotectonics of the Marmara region. In *Active Tectonics of Northwestern Anatolia-The Marmara Poly-Project* (pp. 55-87).

Beroza, G. C., and Spudich, P., 1988, Linearized inversion for fault rupture behavior: Application to the 1984 Morgan Hill, California, earthquake. *Journal of Geophysical Research, 93*, 6275–6296.

Beresnev, I. A., and Atkinson, G. M., 1997, Modeling finite-fault radiation from the ω n spectrum. *Bulletin of the Seismological Society of America, 87*(1), 67-84.

Bécel, A., Laigle, M., de Voogd, B., Hirn, A., Taymaz, T., Galvé, A., ... and Özalaybey, S., 2009, Moho, crustal architecture and deep deformation under the North Marmara Trough, from the SEISMARMARA Leg 1 offshore–onshore reflection–refraction survey. *Tectonophysics, 467*(1-4), 1-21.

Bécel, A., Laigle, M., de Voogd, B., Hirn, A., Taymaz, T., Yolsal-Cevikbilen, S., and Shimamura, H., 2010, North Marmara Trough architecture of basin infill, basement and faults, from PSDM reflection and OBS refraction seismics. *Tectonophysics, 490*(1-2), 1-14.

Boore, D. M., 2003, Simulation of ground motion using the stochastic method. *Pure and Applied Geophysics, 160*, 635-676.

Boore, D. M., 2005, SMSIM—Fortran programs for simulating ground motions from earthquakes: Version 2.3, a revision of OFR 96-80-A, Revised 15 August 2005, U.S. Geol. Surv. Open-File Rept. 00-509, 55 pp.

Boore, D. M., 2009, Comparing stochastic point-source and finite-source ground-motion simulations: SMSIM and EXSIM. *Bulletin of the Seismological Society of America, 99*, 3202–3216.

Boore, D. M., 2010, Orientation-independent, nongeometric-mean measures of seismic intensity from two horizontal components of motion. *Bulletin of the Seismological Society of America, 100*(4), 1830-1835.

Boore, D. M., and Atkinson, G. M., 2008, Ground-motion prediction equations for the average horizontal component of PGA, PGV, and 5% damped PSA at spectral periods between 0.01 s and 10.0 s. *Earthquake Spectra, 24*(1), 99–138.

Boore, D. M., Stewart, J. P., Seyhan, E., and Atkinson, G. M., 2014, NGA-West2 equations for predicting PGA, PGV, and 5% damped PSA for shallow crustal earthquakes. *Earthquake Spectra, 30*(3), 1057-1085.

Boore, D. M., and Thompson, E. M., 2014, Path durations for use in the stochastic-method simulation of ground motions. *Bulletin of the Seismological Society of America, 104*(5), 2541-2552.

Brune, J. N., 1970, Tectonic stress and the spectra of seismic shear waves from earthquakes. *Journal of Geophysical Research, 75*(26), 4997-5009.

Brune, J. N., 1971, Seismic sources, fault plane studies and tectonics. *Eos, Transactions American Geophysical Union, 52*(5), IUGG-178.

Butterworth, S., 1930, On the theory of filter amplifiers. *Wireless Engineer, 7*, 536–541.

Campbell, K. W., and Bozorgnia, Y., 2008, NGA ground motion model for the geometric mean horizontal component of PGA, PGV, PGD, and 5% damped linear elastic response spectra for periods ranging from 0.01 s to 10 s. *Earthquake Spectra, 24*(1), 139–171.

Chiou, B. S.-J., and Youngs, R. R., 2008, An NGA model for the average horizontal component of peak ground motion and response spectra. *Earthquake Spectra, 24*(1), 173–215.

Chiou, B. S. J., and Youngs, R. R., 2014, Update of the Chiou and Youngs NGA model for the average horizontal component of peak ground motion and response spectra. *Earthquake Spectra, 30*(3), 1117-1153.

Çaktı, E. (Project Manager)., 2021–2025, Determination of ground motion intensity parameters to be observed in Istanbul Province by using three-dimensional physics-based and stochastic simulation methods, creation of region-specific ground motion prediction and spatial correlation models (TÜBİTAK Project No. 121M733). Department of Earthquake Engineering, Kandilli Observatory and Earthquake Research Institute, TÜBİTAK, Program Code: 1001-Özel Çağrılar.

Disaster and Emergency Management Authority (AFAD)., 2025, Earthquake event data. Retrieved April 30, 2025, from https://www.afad.gov.tr/earthquake-data

Dreger, D. S., Gee, L., Lombard, P., Murray, M. H., and Romanowicz, B., 2005, Rapid finite-source analysis and near-fault strong ground motions: Application to the 2003 Mw 6.5 San Simeon and 2004 Mw 6.0 Parkfield earthquakes. *Seismological Research Letters, 76*, 40–48.

Engineering Strong-Motion Database (ESM)., 2025, Strong-motion waveform data [Data set]. Retrieved April 30, 2025, from https://esm-db.eu/

Ergintav, S., Reilinger, R. E., Çakmak, R., Floyd, M., Cakir, Z., Doğan, U., King, R. W., McClusky S., and Özener, H., 2014, Istanbul's earthquake hot spots: Geodetic constraints on strain accumulation along faults in the Marmara seismic gap. *Geophysical Research Letters, 41*(16), 5783-5788.

Esposito, S., and Iervolino, I., 2012, Spatial correlation of spectral acceleration in European data. *Bulletin of the Seismological Society of America, 102*(6), 2781-2788.

EXSIM., 2018, [Software]. https://www.daveboore.com/software_online.html

Goda, K., and Atkinson, G. M., 2010, Intraevent spatial correlation of ground-motion parameters using SK-net data. *Bulletin of the Seismological Society of America, 100*(6), 3055-3067.

Hayes, G. P., 2017, The finite, kinematic rupture properties of great-sized earthquakes since 1990. *Earth and Planetary Science Letters, 468*, 94–100. https://doi.org/10.1016/j.epsl.2017.04.003

Hernandez, B., Cotton, F., and Campillo, M., 1999, Contribution of radar interferometry to a two-step inversion of the kinematic process of the 1992 Landers earthquake. *Journal of Geophysical Research: Solid Earth, 104*(B6), 13083–13099.

Horasan, G., 1998, S-wave attenuation in the Marmara region, northwestern Turkey.

Horikawa, H., Hirahara, K., Umeda, Y., Hashimoto, M., and Kusano, F., 1996, Simultaneous inversion of geodetic and strong-motion data for the source process of the Hyogo-ken Nanbu, Japan, earthquake. *Journal of Physics of the Earth, 44*, 455–471.

Hirn, A., Singh, S., Charvis, P., Géli, L., Laigle, M., Lépine, J. C., ... and Sarıkavak, K., 2002, Seismarmara 2001: A Marine Seismic Survey and Offshore-onshore Artificial Source and Natural Earthquakes in the Seismogenic Region of the Sea of Marmara. In *EGS General Assembly Conference Abstracts* (p. 547).

Infantino, M., Mazzieri, I., Özcebe, A. G., Paolucci, R., and Stupazzini, M., 2020, 3D physics-based numerical simulations of ground motion in Istanbul from earthquakes along the Marmara segment of the north Anatolian fault. *Bulletin of the Seismological Society of America, 110*(5), 2559-2576.

Istanbul Earthquake Rapid Response and Early Warning System (IERREWS)., 2025, Earthquake waveform data [Unpublished dataset]. Department of Earthquake Engineering, Kandilli Observatory and Earthquake Research Institute.

Istanbul Metropolitan Municipality., 2007, Istanbul and Earthquake, European Side South Microzonation Project (online).

Istanbul Metropolitan Municipality., 2009, Istanbul and Earthquake, Anatolian Side Microzonation Project (online).

Jayaram, N., and Baker, J. W., 2009, Correlation model for spatially distributed ground-motion intensities. *Earthquake Engineering & Structural Dynamics, 38*(15), 1687-1708.

Jayaram, N., and Baker, J. W., 2010, Considering spatial correlation in mixed-effects regression and the impact on ground-motion models. *Bulletin of the Seismological Society of America*, *100*(6), 3295-3303.

Kadirioğlu, F. T., and Kartal, R. F., 2016, The new empirical magnitude conversion relations using an improved earthquake catalogue for Turkey and its near vicinity (1900-2012). *Turkish Journal of Earth Sciences, 25*(4), 300-310.

Karabulut, H., Özalaybey, S., Taymaz, T., Aktar, M., Selvi, O., and Kocaoğlu, A., 2003, A tomographic image of the shallow crustal structure in the Eastern Marmara. *Geophysical Research Letters, 30*(24).

Karabulut, H., Güvercin, S. E., Eskiköy, F., Konca, A. Ö., and Ergintav, S., 2021, The moderate size 2019 September M w 5.8 Silivri earthquake unveils the complexity of the Main Marmara Fault shear zone. *Geophysical Journal International, 224*(1), 377-388.

Karimzadeh, S., Askan, A., and Yakut, A., 2018, Assessment of simulated ground motions in earthquake engineering practice: A case study for Duzce (Turkey). In *Best Practices in Physics-based Fault Rupture Models for Seismic Hazard Assessment of Nuclear Installations* (pp. 265-283).

Le Pichon, X., Chamot-Rooke, N., Rangin, C., and Sengör, A. M. C., 2003, The North Anatolian fault in the Sea of Marmara. *Journal of Geophysical Research: Solid Earth, 108*(B4).

Loth, C., and Baker, J. W., 2013, A spatial cross-correlation model of spectral accelerations at multiple periods. *Earthquake Engineering & Structural Dynamics*, *42*(3), 397-417.

Malcıoğlu, F. S., Süleyman, H., and Çaktı, E., 2022, Seismological and engineering characteristics of strong motion data from 24 and 26 September 2019 Marmara Sea earthquakes. *Bulletin of Earthquake Engineering, 20*(11), 5567-5599.

Margaris, B. N., and Boore, D. M., 1998, Determination of Δσ and κ0 from response spectra of large earthquakes in Greece. *Bulletin of the Seismological Society of America, 88*(1), 170-182.

Mendoza, C., and Hartzell, S., 2013, Finite-fault source inversion using teleseismic P waves: Simple parameterization and rapid analysis. *Bulletin of the Seismological Society of America, 103*(2A), 834–844.

Motazedian, D., and Atkinson, G. M., 2005, Stochastic finite-fault modeling based on a dynamic corner frequency. *Bulletin of the Seismological Society of America, 95*, 995–1010.

MTA, General Directorate of Mineral Research and Exploration., 2004, 1/500,000 scale geological maps of Turkey. Retrieved from https://www.mta.gov.tr/v3.0/hizmetler/500cd

Murru, M., Akıncı, A., Falcone, G., Pucci, S., Console, R., and Parsons, T., 2016, M≥ 7 earthquake rupture forecast and time-dependent probability for the Sea of Marmara region, Turkey. *Journal of Geophysical Research: Solid Earth, 121*(4), 2679-2707.

Özbey, C., Sari, A., Manuel, L., Erdik, M., and Fahjan, Y., 2004, An empirical attenuation relationship for northwestern Turkey ground motion using a random effects approach. *Soil Dynamics and Earthquake Engineering*, *24*(2), 115-125.

Özmen, E., Karimzadeh, S., and Askan, A., 2020, Broadband ground motion simulation within the city of Düzce (Turkey) and building response simulation. *Pure and Applied Geophysics, 177*(5), 2353-2373.

Parsons, T., 2004, Recalculated probability of M≥ 7 earthquakes beneath the Sea of Marmara, Turkey. *Journal of Geophysical Research: Solid Earth, 109*(B5).

Pondard, N., Armijo, R., King, G. C., Meyer, B., and Flerit, F., 2007, Fault interactions in the Sea of Marmara pull-apart (North Anatolian Fault): earthquake clustering and propagating earthquake sequences. *Geophysical Journal International, 171*(3), 1185-1197.

Polat, G., Özel, N. M., and Koulakov, I., 2016, Investigating P- and S-wave velocity structure beneath the Marmara region (Turkey) and the surrounding area from local earthquake tomography. *Earth, Planets and Space, 68*(1), 1-14.

Reilinger, R. E., Ergintav, S., Burgmann, R., McClusky, S., Lenk, O., Barka, A., Gurkan, O., Hearn, L., Feigl, K. L., Cakmak, R., Aktug, B., Ozener, H., and Toksoz, M. N., 2000, Coseismic and postseismic fault slip for the 17 August 1999, M=7.5, Izmit, Turkey earthquake. *Science, 289*, 1519–1524.

Rupgen., 2000, MATLAB routine. Retrieved from http://equake-rc.info/cers-software/rupgen/

Salichon, J., Lundgren, P., Delouis, B., and Giardini, D., 2004, Slip history of the 16 October 1999 Mw 7.1 Hector Mine Earthquake (California) from the inversion of InSAR, GPS, and teleseismic data. *Bulletin of the Seismological Society of America, 94*, 2015–2027.

Sandıkkaya, M. A., Akkar, S., Kale, Ö., and Yenier, E., 2023, A simulation-based regional ground-motion model for Western Turkiye. *Bulletin of Earthquake Engineering*, *21*(7), 3221-3249.

Semmane, F., Cotton, F., and Campillo, M., 2005, The 2000 Tottori earthquake: A shallow earthquake with no surface rupture and slip properties controlled by depth. *Journal of Geophysical Research, 110*(B3), B03306. https://doi.org/10.1029/2004JB003194

Smerzini, C., and Villani, M., 2012, Broadband numerical simulations in complex near-field geological configurations: The case of the 2009 M w 6.3 L'Aquila earthquake. *Bulletin of the Seismological Society of America, 102*(6), 2436-2451.

Strong-Motion Virtual Data Center (VDC)., 2024, Retrieved January 24, 2024, from https://www.strongmotioncenter.org

Süleyman, H., and Çaktı, E., 2018, On the correlation between κ0 and VS30 [Poster presentation]. Orfeus 2018 Annual Observatory Coordination Meeting and Workshop, Athens, Greece. https://cutt.ly/XKXqaXu

Süleyman, H., and Çaktı, E., 2024, Assessing seismic hazard and uncertainty in Büyükçekmece using ground motion simulations. *Bulletin of Earthquake Engineering, 22*(10), 4873-4895.

Tarancıoğlu, A., Özalaybey, S., and Kocaoğlu, A. H., 2020, Three-dimensional seismic tomographic imaging beneath the Sea of Marmara: evidence for locked and creeping sections of the Main Marmara Fault. *Geophysical Journal International, 223*(2), 1172-1187.

Thingbaijam, K. K. S., Mai, P. M., and Goda, K., 2017, New empirical earthquake source-scaling laws. *Bulletin of the Seismological Society of America, 107*(5), 2225-2246.

Uğurhan, B., and Askan, A., 2010, Stochastic strong ground motion simulation of the 12 November 1999 Düzce (Turkey) earthquake using a dynamic corner frequency approach. *Bulletin of the Seismological Society of America, 100*(4), 1498-1512.

Wald, D. J., Helmberger, D. V., and Hartzell, S. H., 1990, Rupture process of the 1987 Superstition Hills Earthquake from the inversion of strong-motion data. *Bulletin of the Seismological Society of America, 80*, 1079–1098.

Wald, D. J., and Heaton, T. H., 1994, Spatial and temporal distribution of slip for the 1992 Landers, California, earthquake. *Bulletin of the Seismological Society of America, 84*, 668–691.

Wald, D. J., 1996, Slip history of the 1995 Kobe, Japan, earthquake determined from strong motion, teleseismic, and geodetic data. *Journal of Physics of the Earth, 44*, 489–503.

Wells, D. L., and Coppersmith, K. J., 1994, New empirical relationships among magnitude, rupture length, rupture width, rupture area, and surface displacement. *Bulletin of the Seismological Society of America, 84*(4), 974-1002.

Yagi, Y., and Kikuchi, M., 2000, Source rupture process of the Kocaeli, Turkey, earthquake of August 17, 1999, obtained by joint inversion of near-field data and teleseismic data. *Geophysical Research Letters, 27*, 1969–1972.

Yaltırak, C., 2002, Tectonic evolution of the Marmara Sea and its surroundings. *Marine Geology, 190*(1-2), 493-529.

Yenihayat, N., 2022, Constraining source properties of the 1509, 1766, and 1894 Istanbul earthquakes / 1509, 1766 ve 1894 İstanbul depremlerinin kaynak parametre özelliklerinin belirlenmesi (Doctoral dissertation). Boğaziçi University, Kandilli Observatory and Earthquake Research Institute, Department of Earthquake Engineering.

Yenihayat, N., Çaktı, E., and Şeşetyan, K., 2024, Stochastic ground motion simulation of the 26 September 2019 Mw 5.8 Silivri (Istanbul) earthquake. *Bulletin of Earthquake Engineering, 22*(4), 1605-1633.

Zengin, E., and Çaktı, E., 2012, Scenario based ground motion simulations for Istanbul, Turkey. In *Proceedings of 15th World Conference on Earthquake Engineering* (pp. 24557-24566). Lisbon, Portugal.

APPENDIX A: STOCHASTIC AND 3D PHYSICS-BASED SIMULATION COMPARISONS

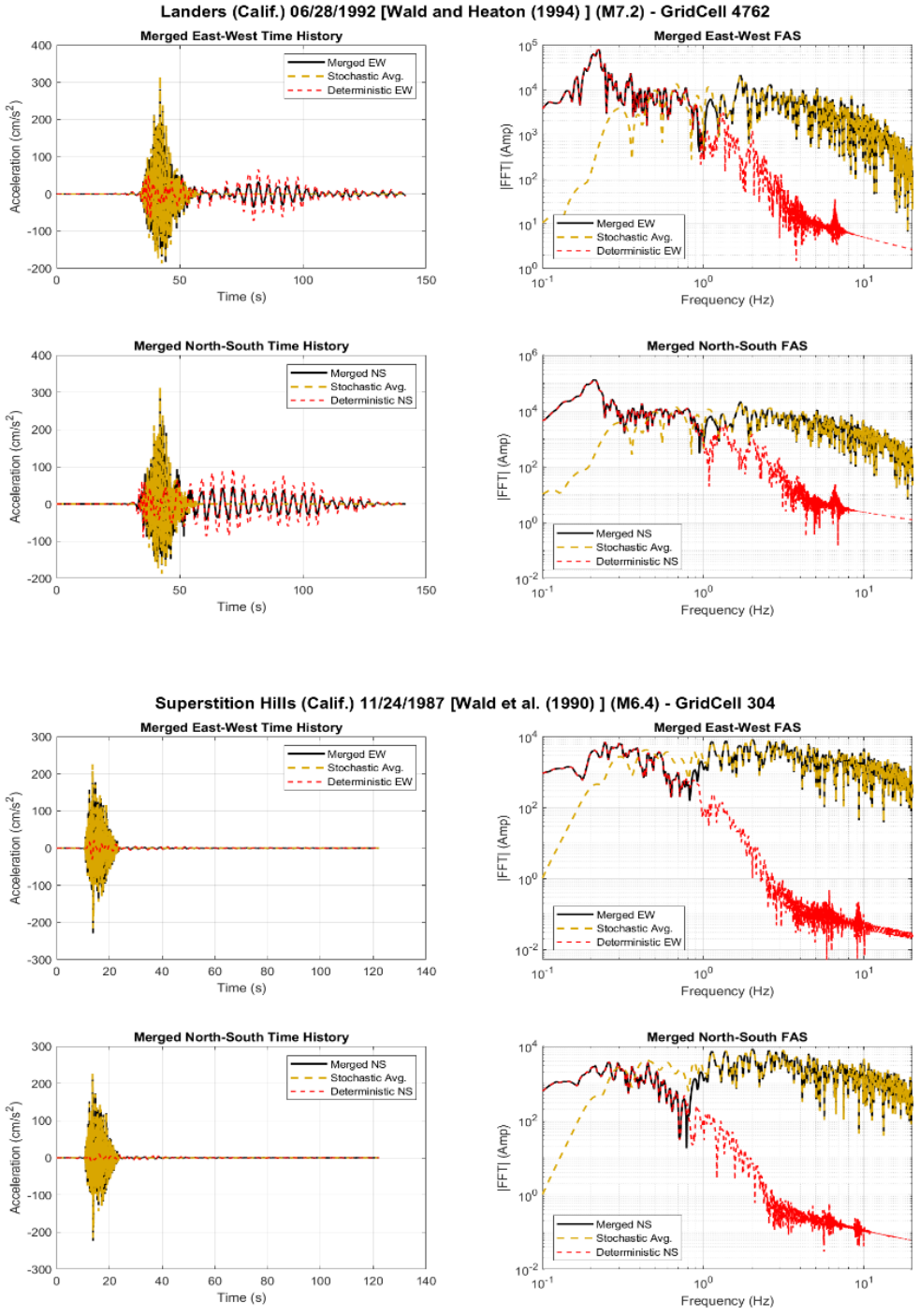

Figure A.1: Stochastic and 3D physics-based simulation comparisons in time domain; at selected grid cells.

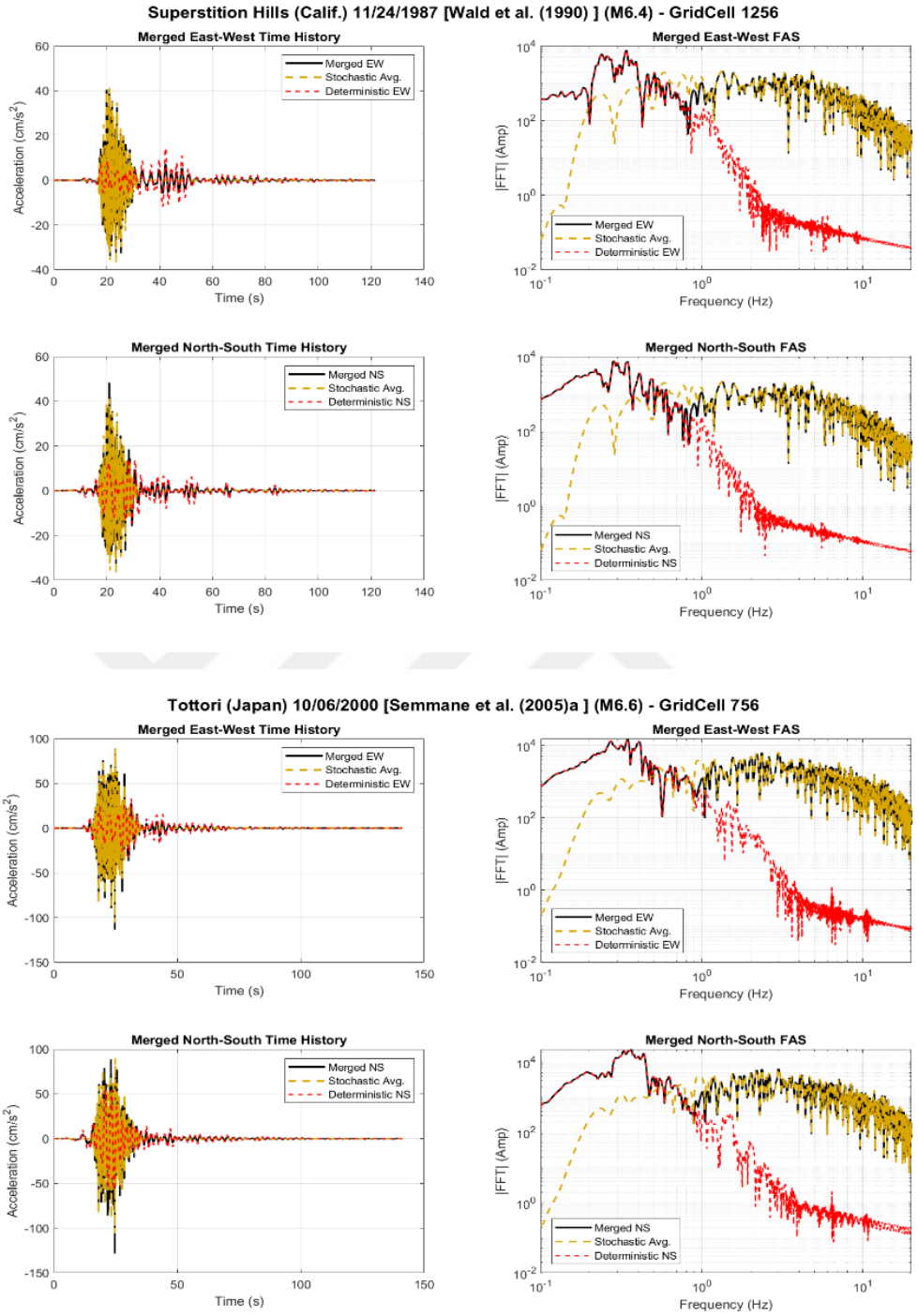

Figure A.1. Stochastic and 3D physics-based simulation comparisons in time domain; at selected grid cells (cont.).

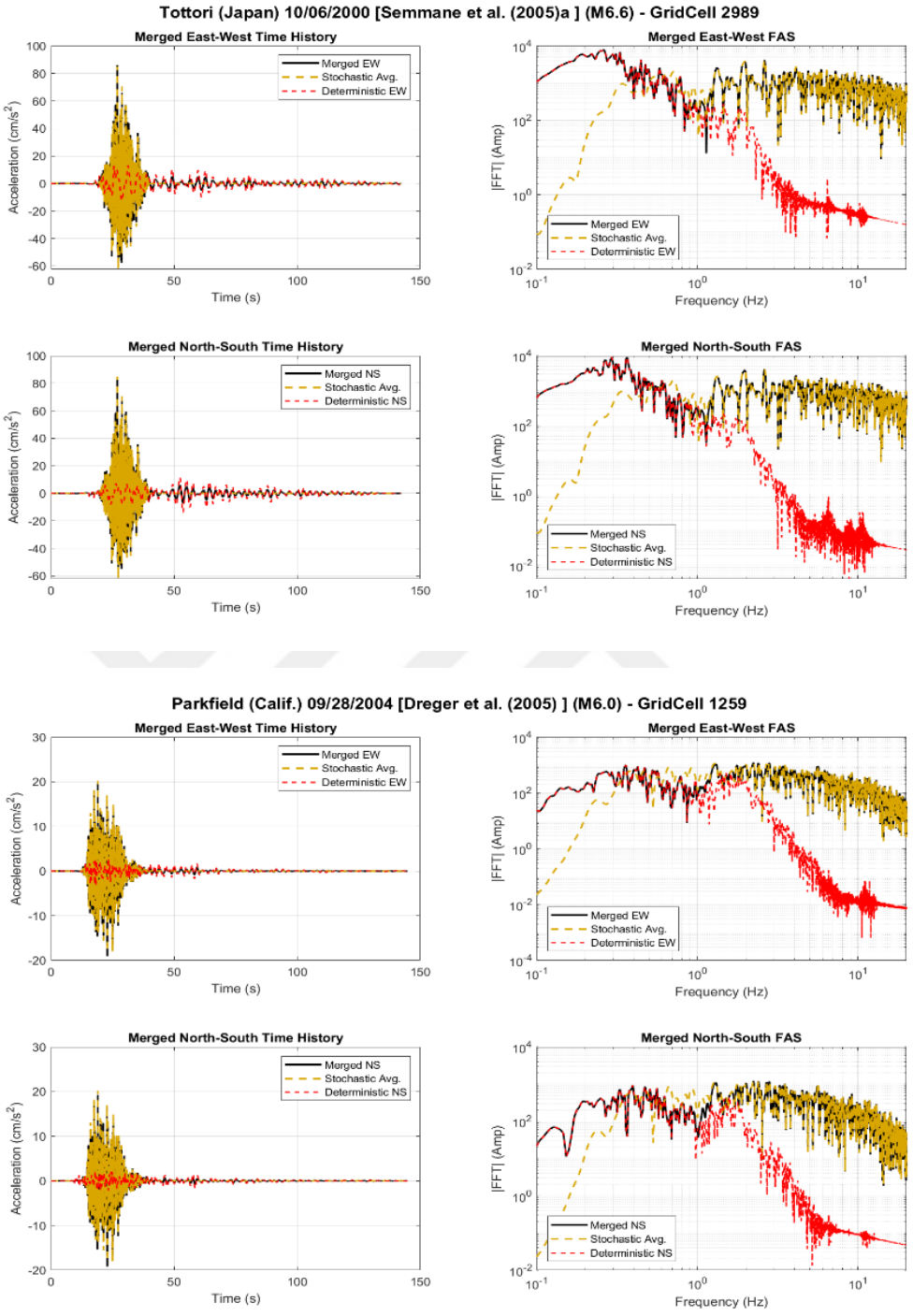

Figure A.1: Stochastic and 3D physics-based simulation comparisons in time domain; at selected grid cells (cont.).

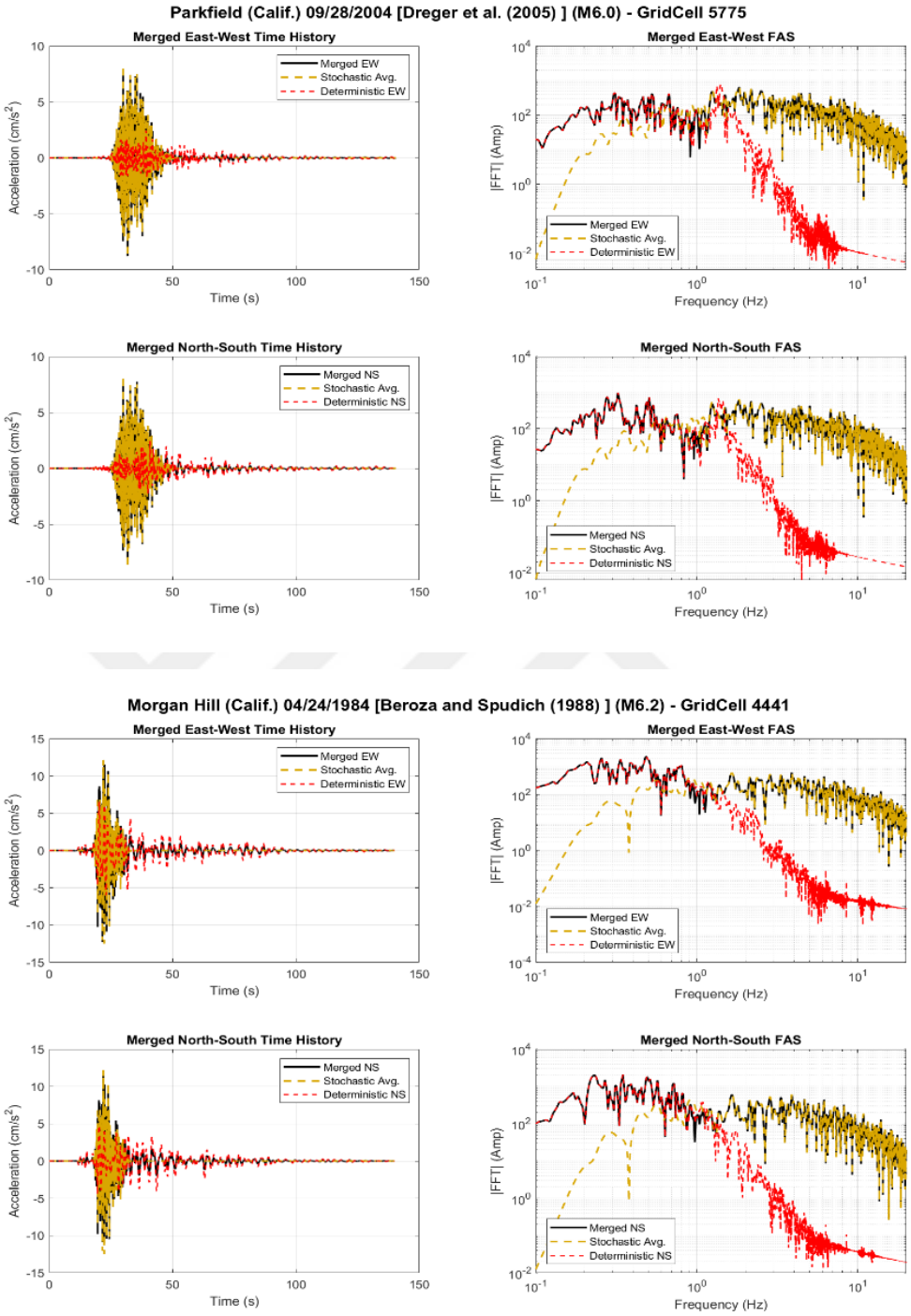

Figure A.1: Stochastic and 3D physics-based simulation comparisons in time domain; at selected grid cells (cont.).

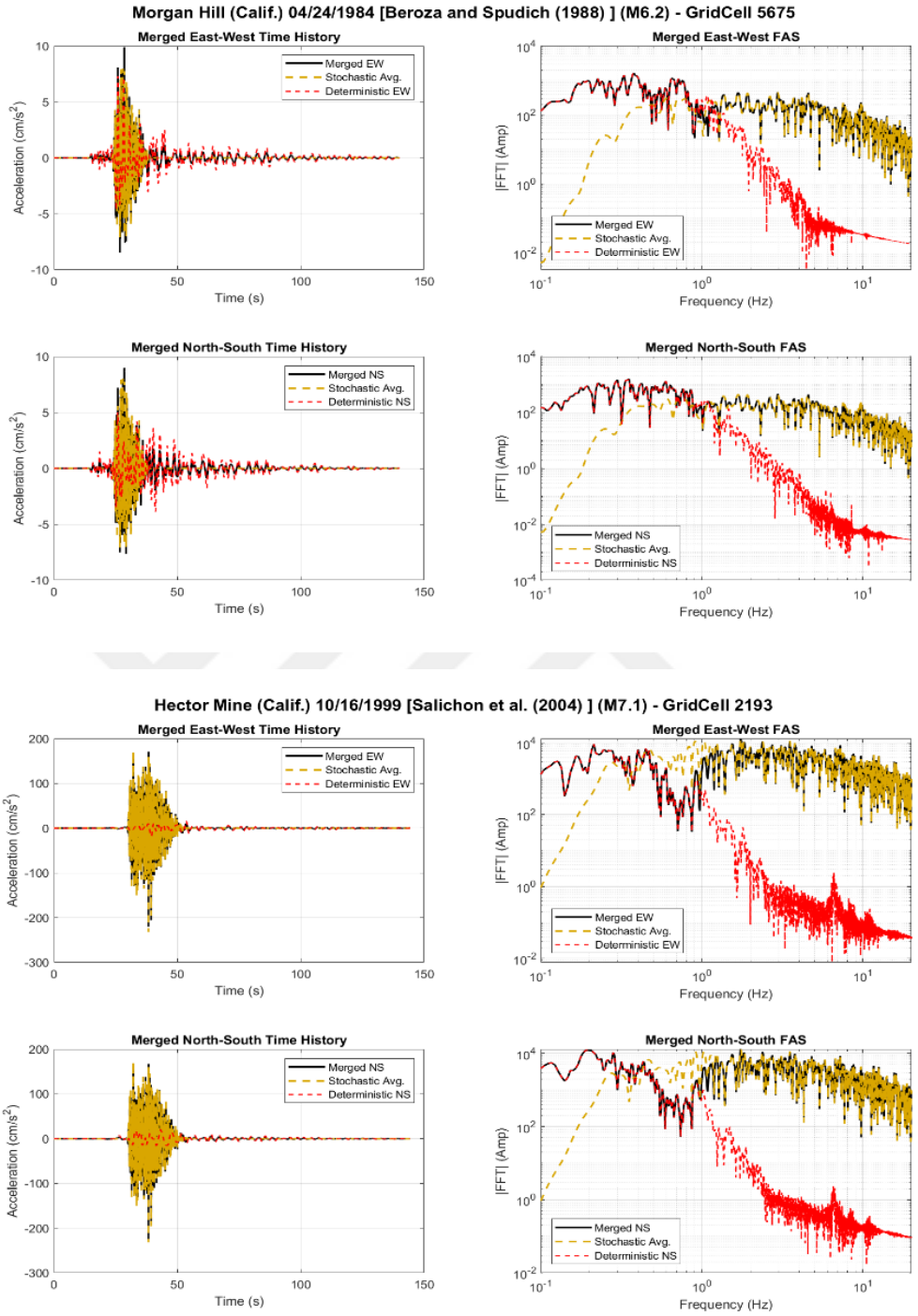

Figure A.1: Stochastic and 3D physics-based simulation comparisons in time domain; at selected grid cells (cont.).

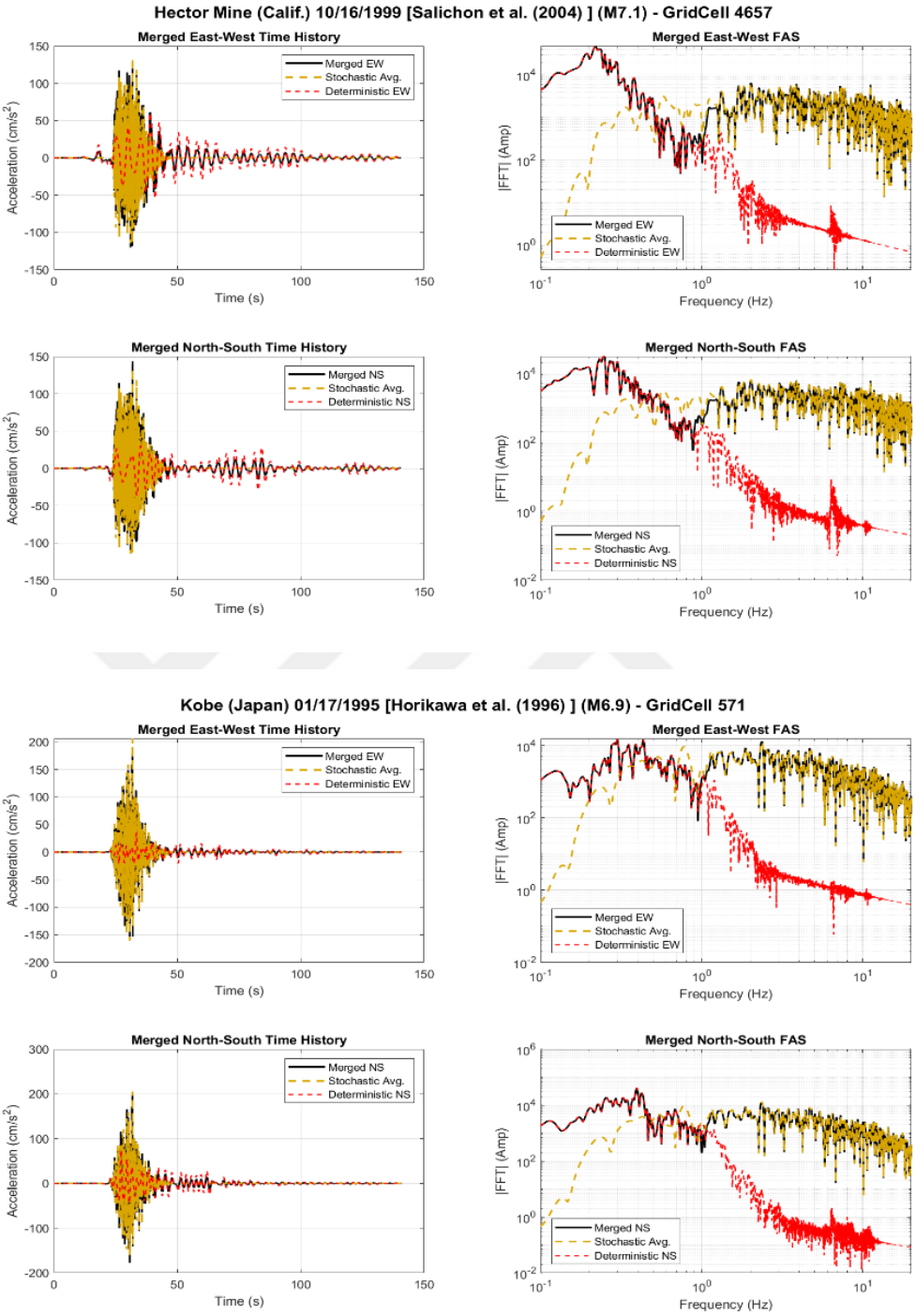

Figure A.1: Stochastic and 3D physics-based simulation comparisons in time domain; at selected grid cells (cont.).

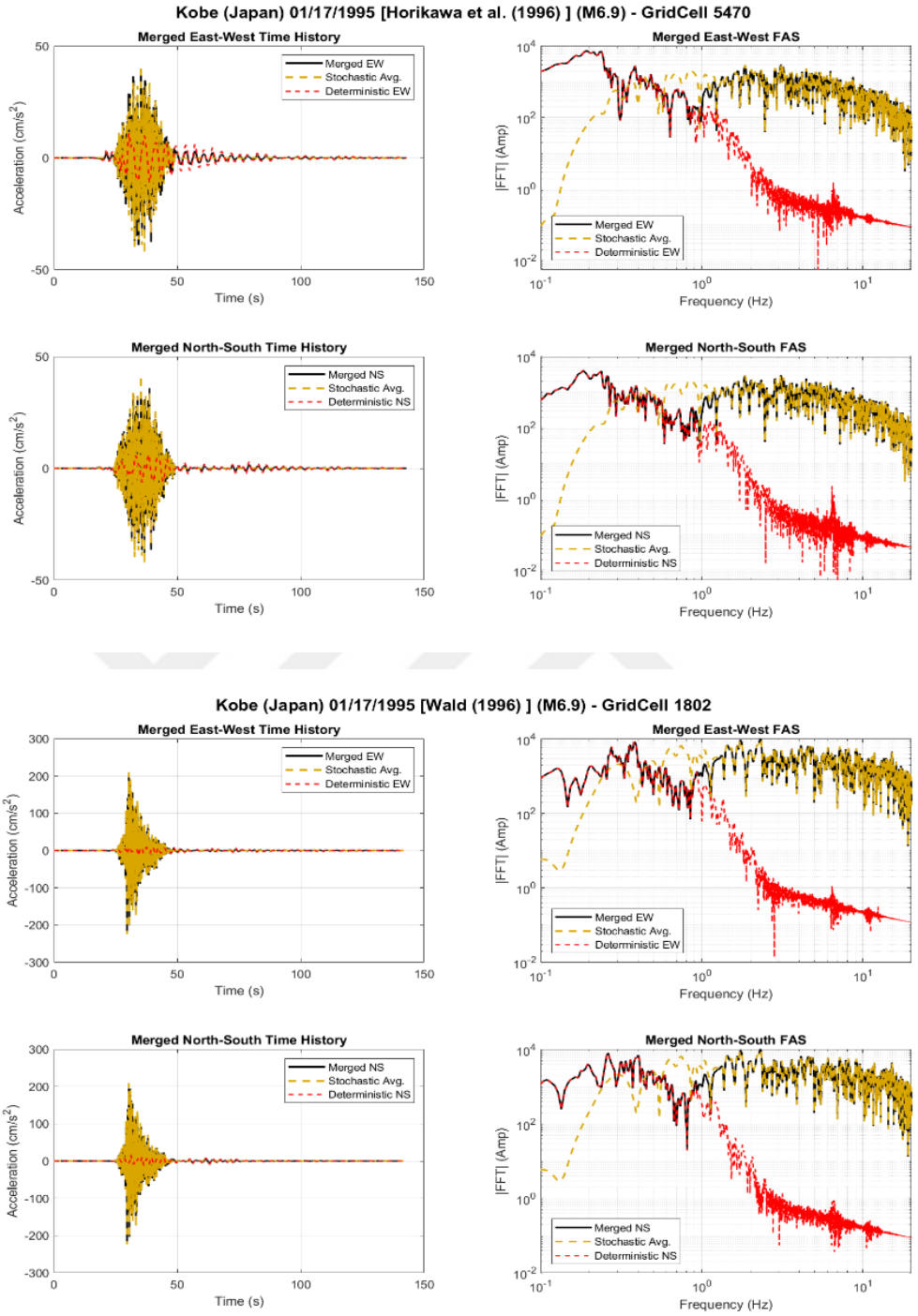

Figure A.1: Stochastic and 3D physics-based simulation comparisons in time domain; at selected grid cells (cont.).

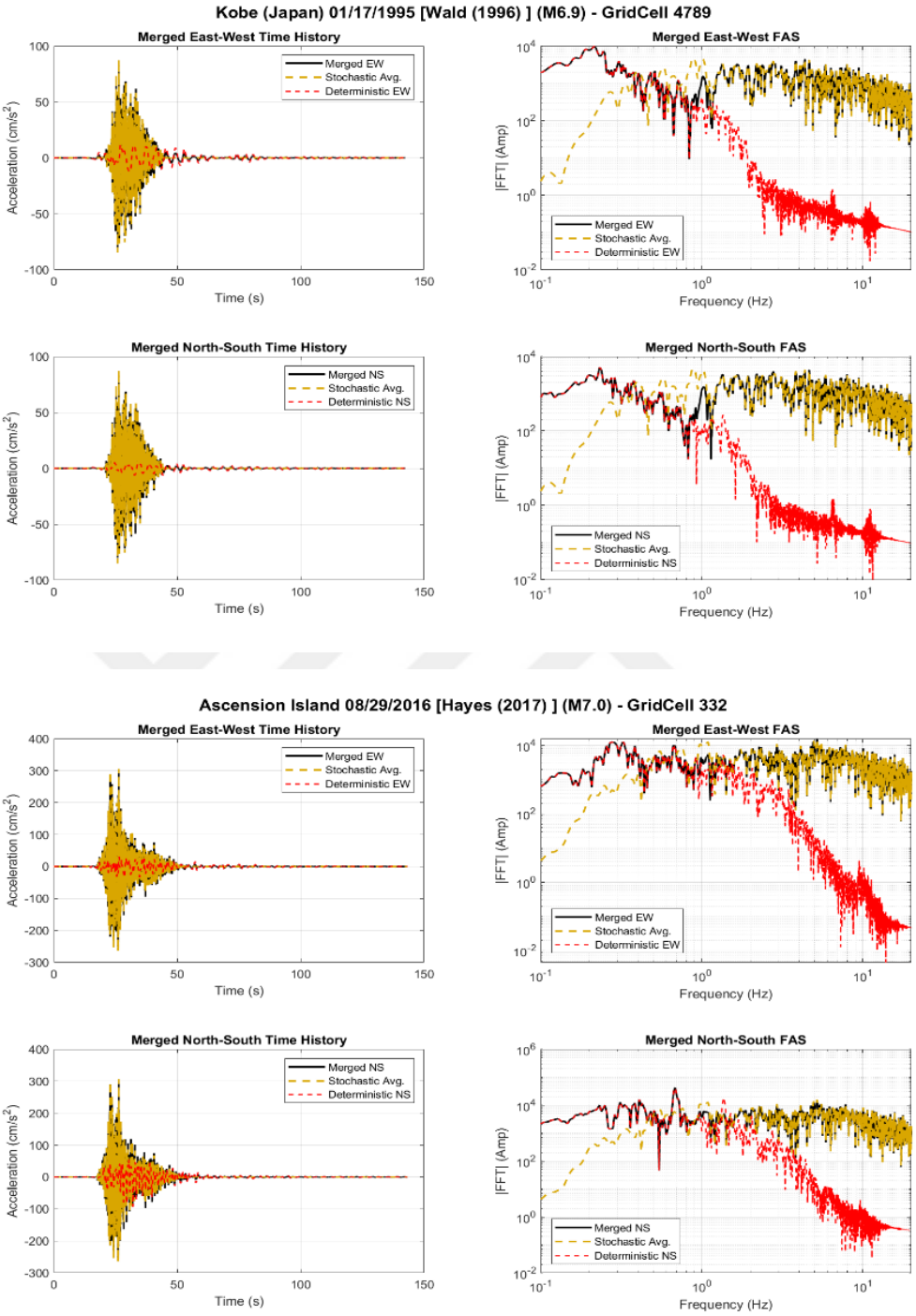

Figure A.1: Stochastic and 3D physics-based simulation comparisons in time domain; at selected grid cells (cont.).

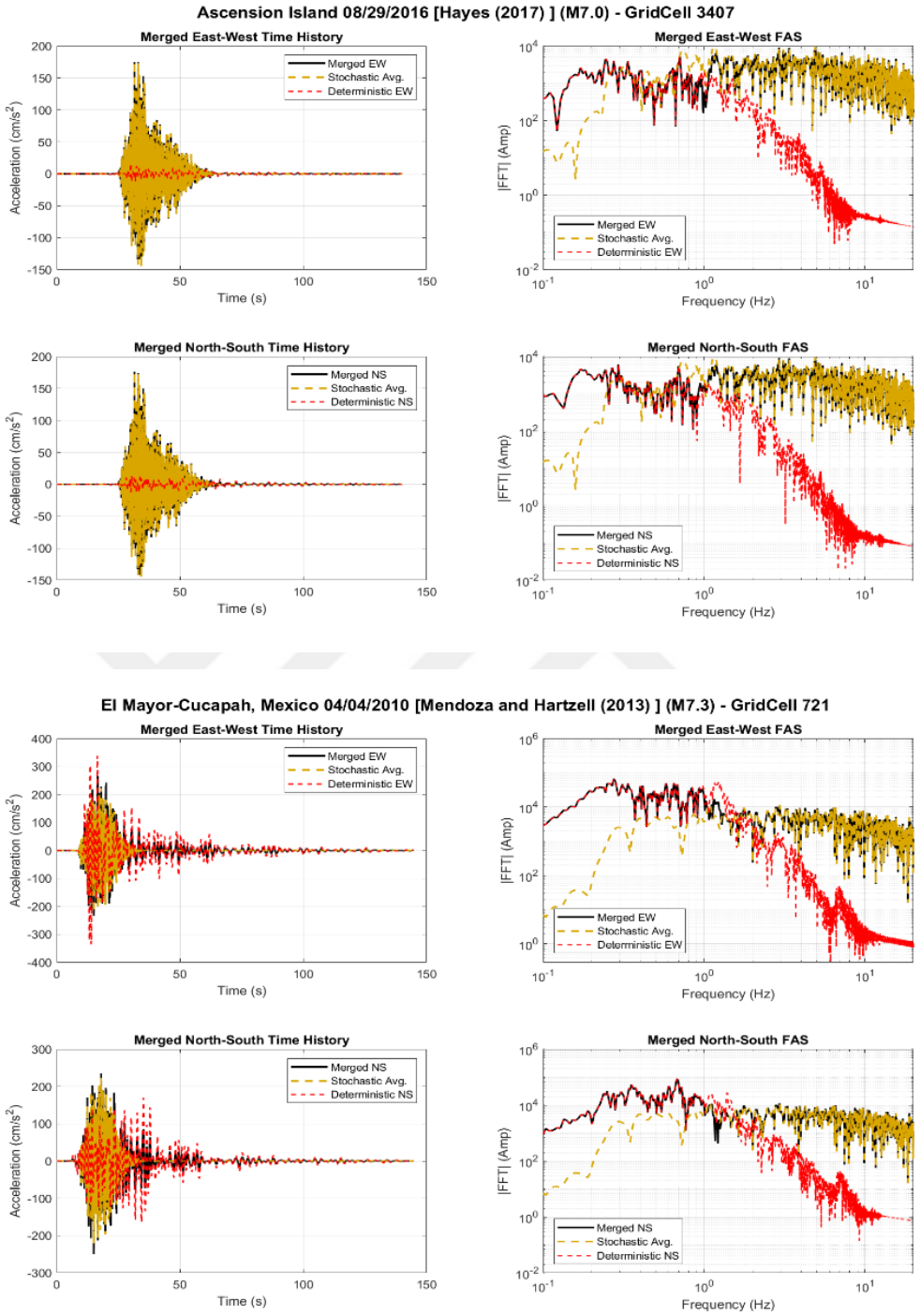

Figure A.1: Stochastic and 3D physics-based simulation comparisons in time domain; at selected grid cells (cont.).

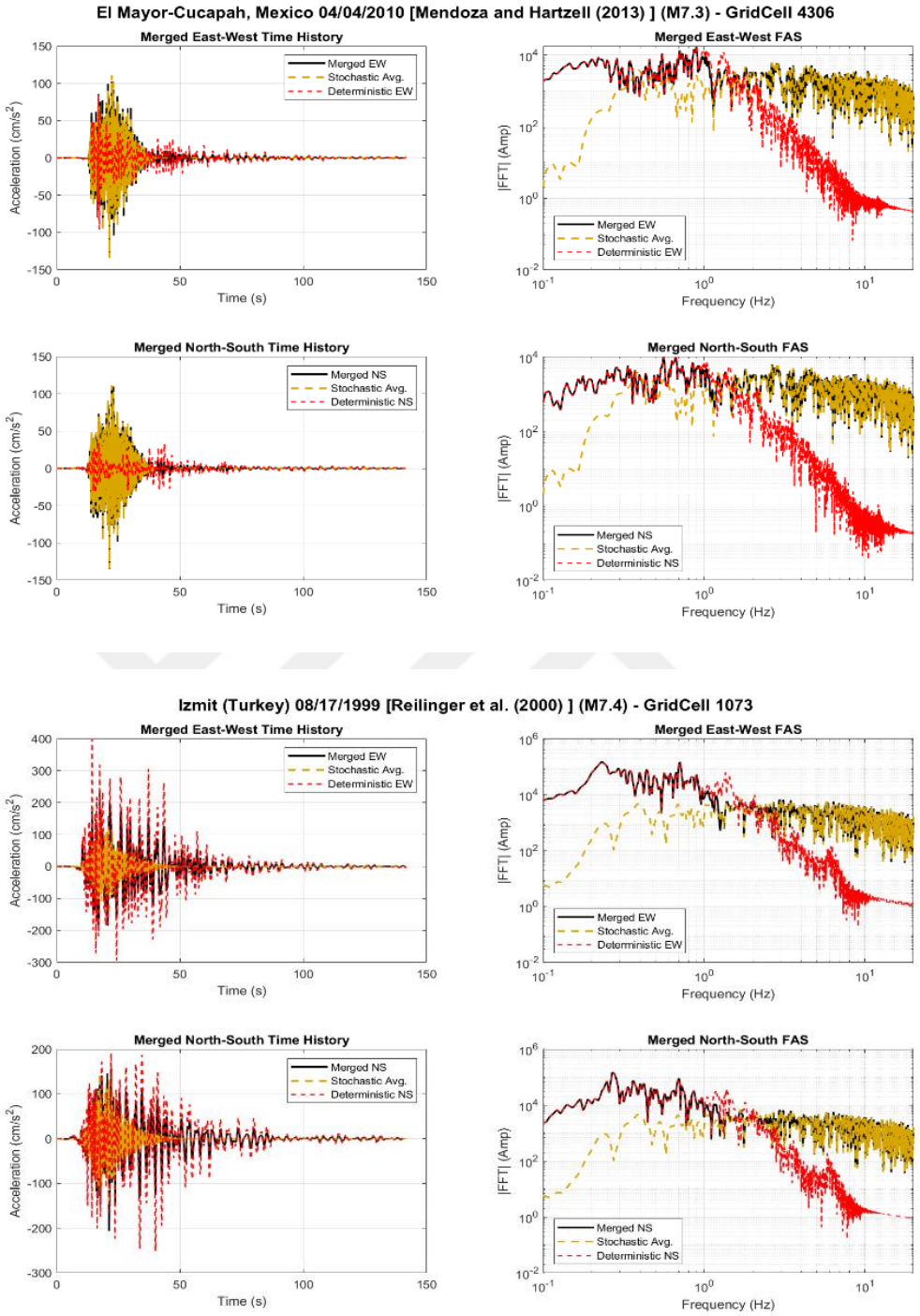

Figure A.1: Stochastic and 3D physics-based simulation comparisons in time domain; at selected grid cells (cont.).

APPENDIX B: PREDICTIVE POWER EVALUATION OF THE DEVELOPED MODELS

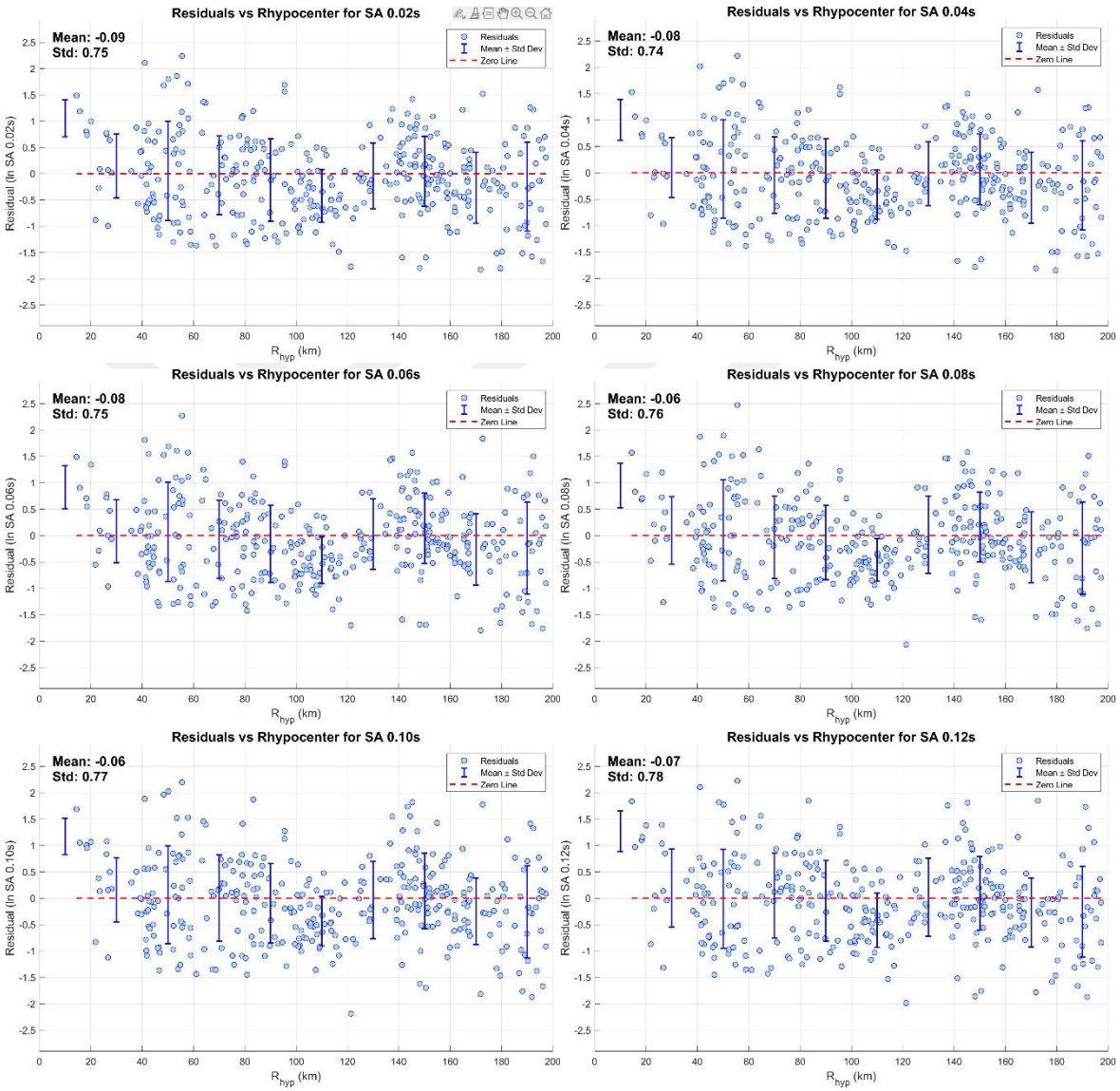

Figure B.1. Residuals versus hypocentral distance for PGA, PSA values at 0.02-5 seconds and PGV.

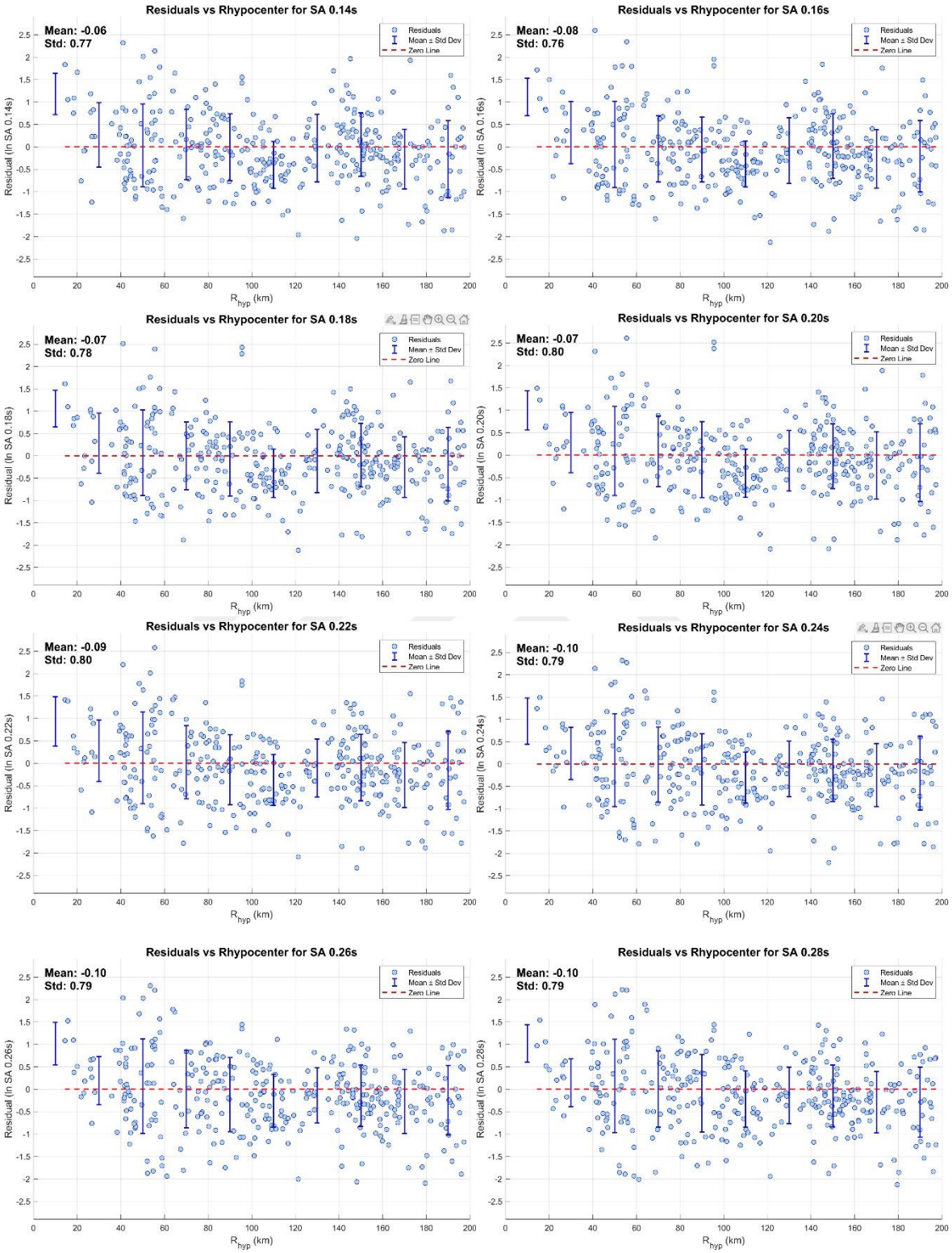

Figure B.1. Residuals versus hypocentral distance for PGA, PSA values at 0.02-5 seconds and PGV (cont.).

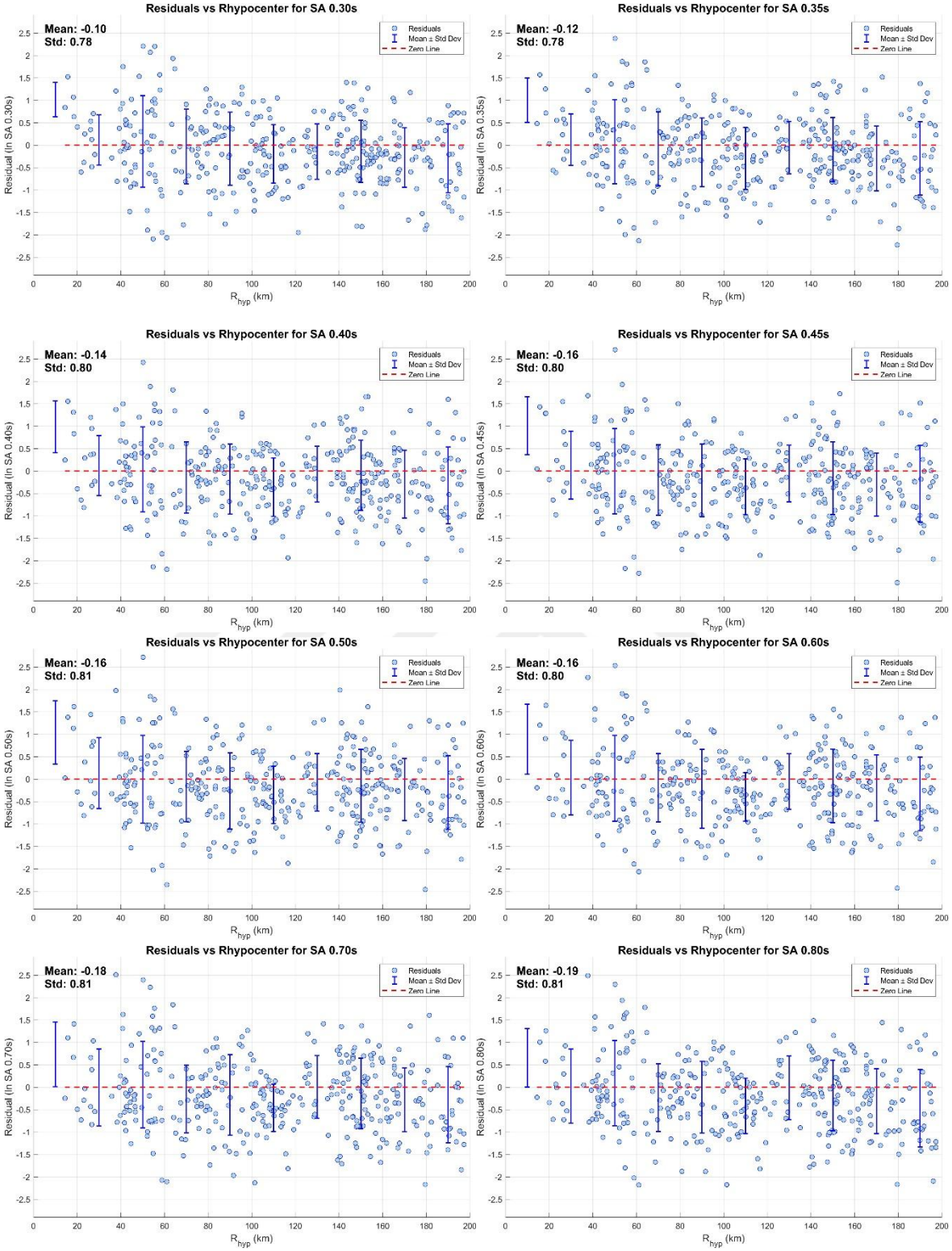

Figure B.1. Residuals versus hypocentral distance for PGA, PSA values at 0.02-5 seconds and PGV (cont.).

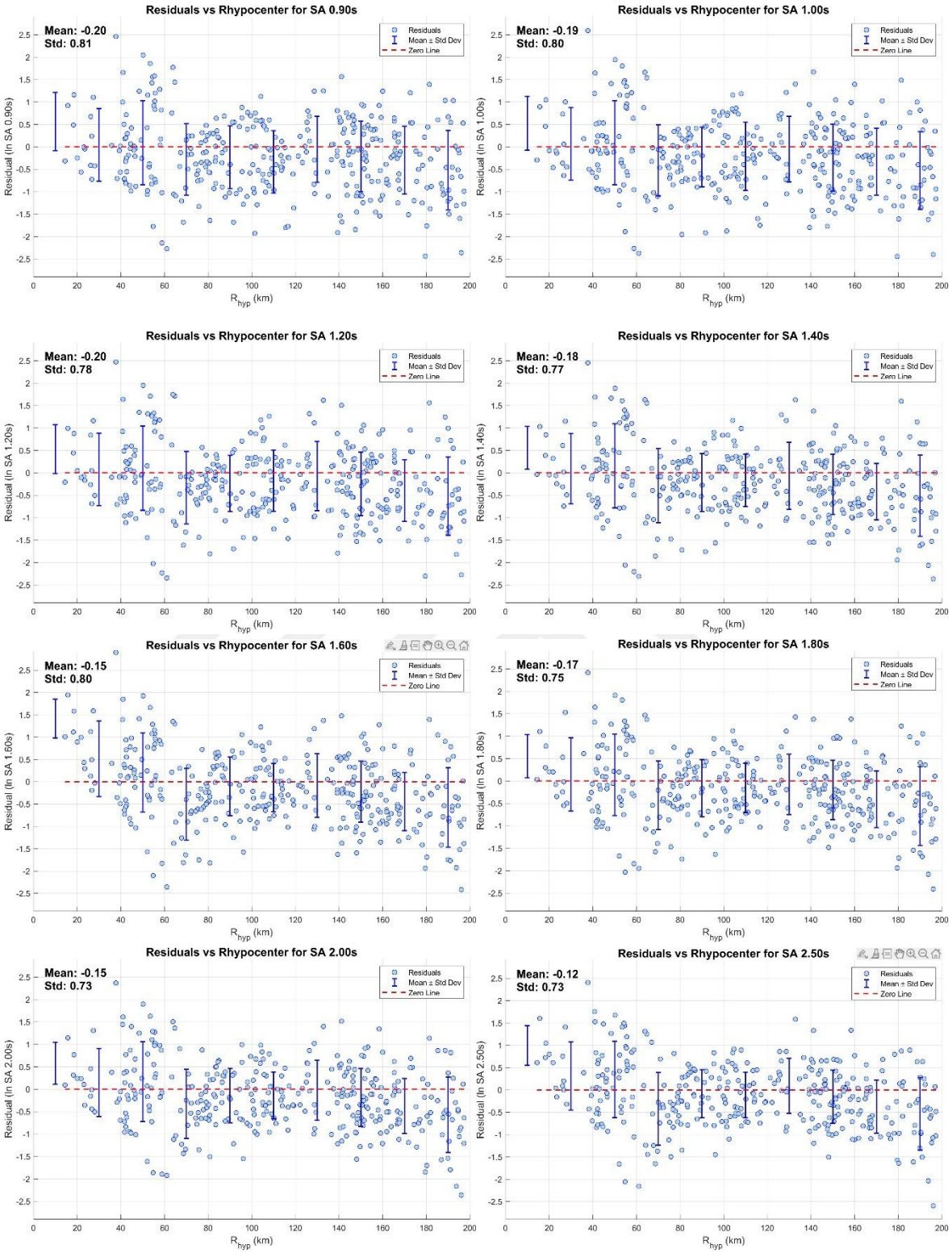

Figure B.1. Residuals versus hypocentral distance for PGA, PSA values at 0.02-5 seconds and PGV (cont.).

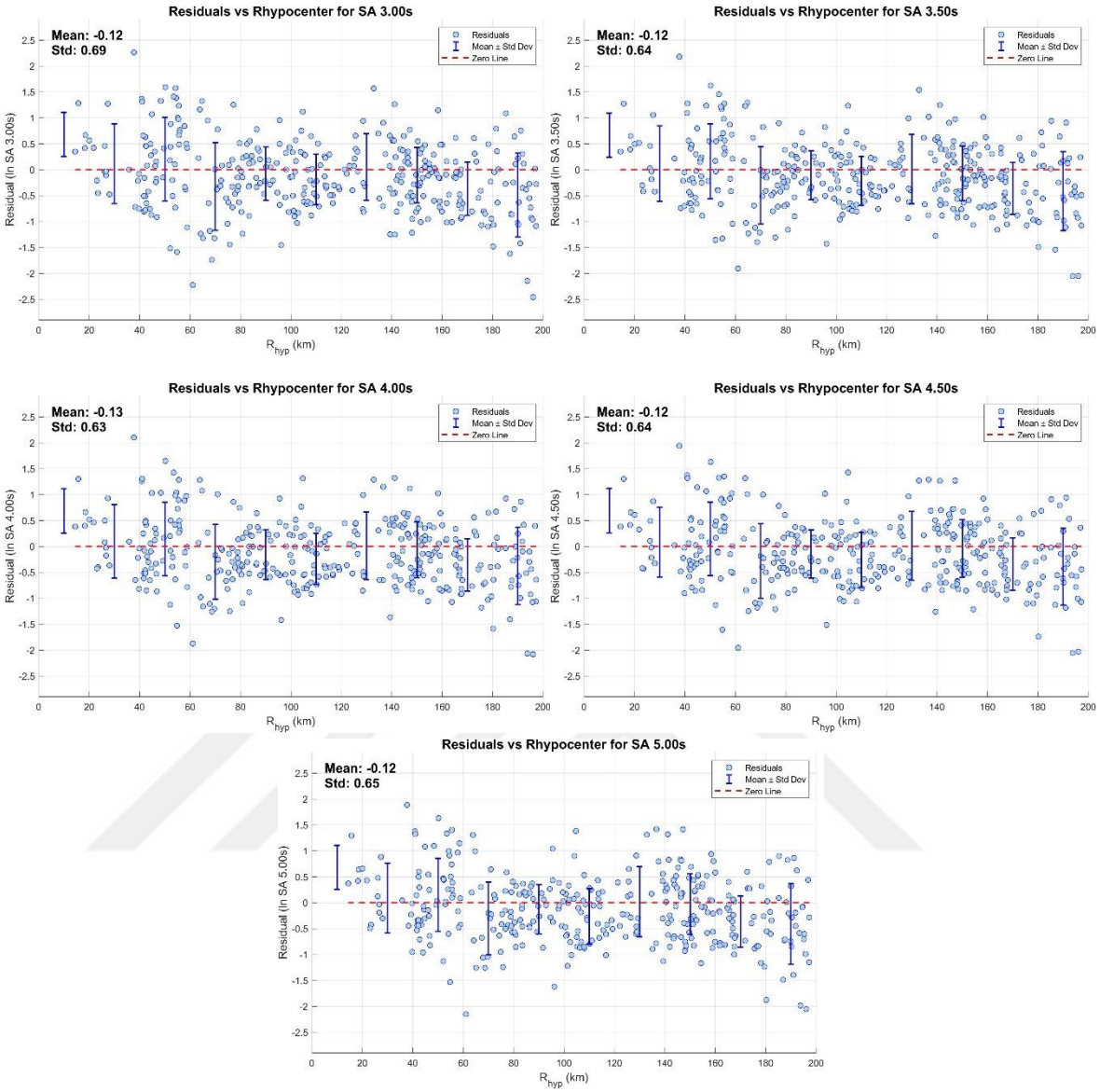

Figure B.1. Residuals versus hypocentral distance for PGA, PSA values at 0.02-5 seconds and PGV (cont.).

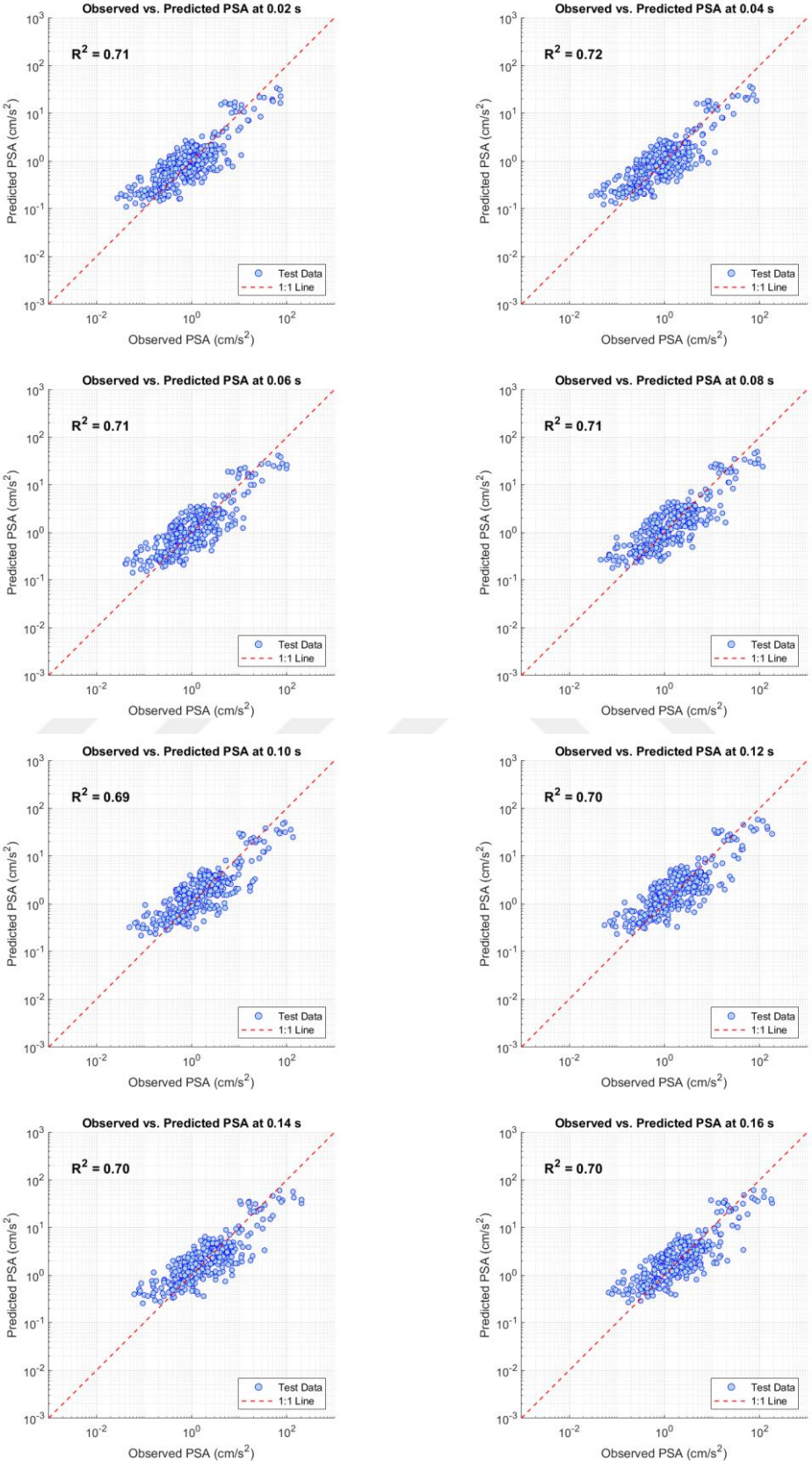

Figure B.2. Predicted versus observed PGA, PSAs at 0.02-5 seconds and PGV comparisons.

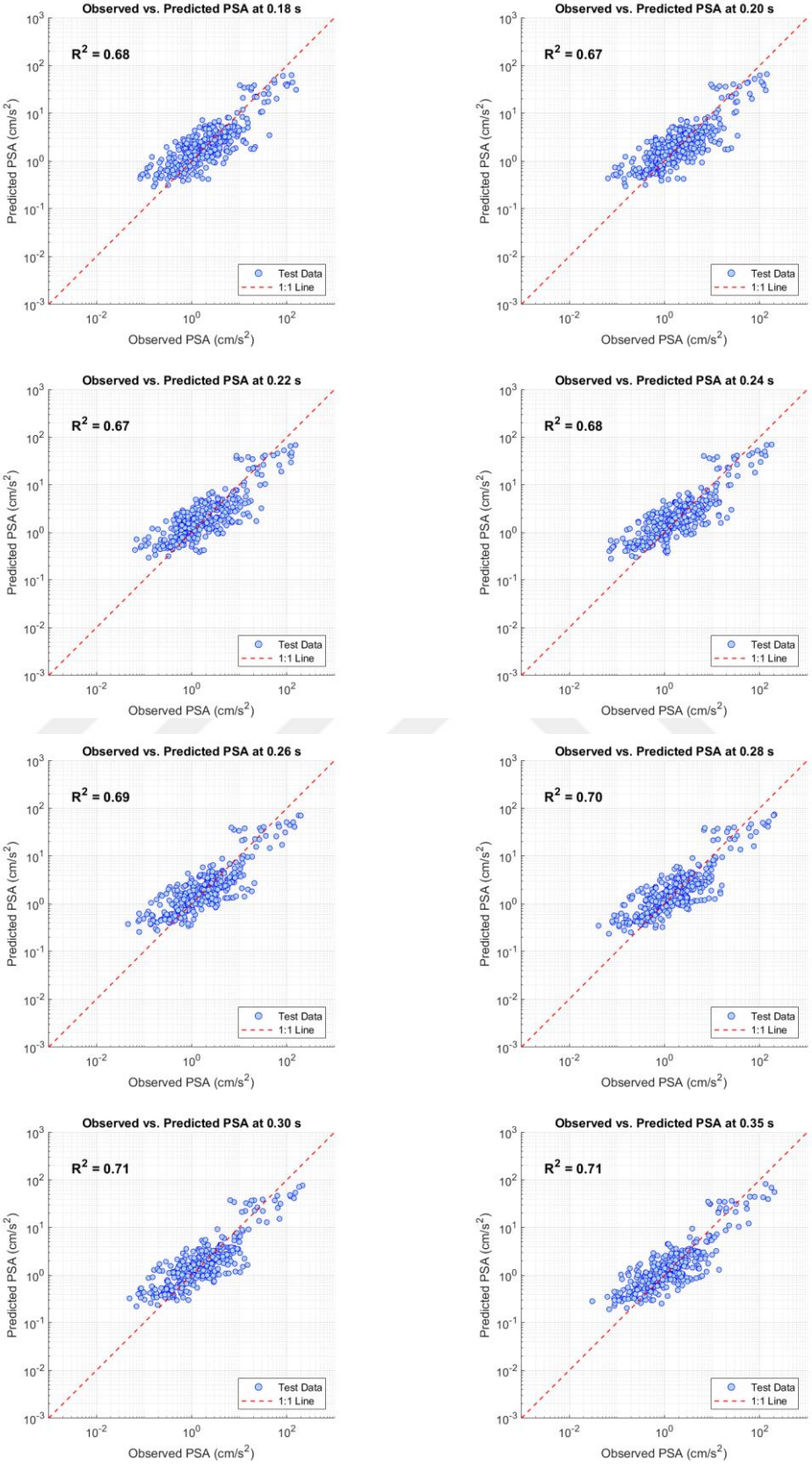

Figure B.2. Predicted versus observed PGA, PSAs at 0.02-5 seconds and PGV comparisons (cont.).

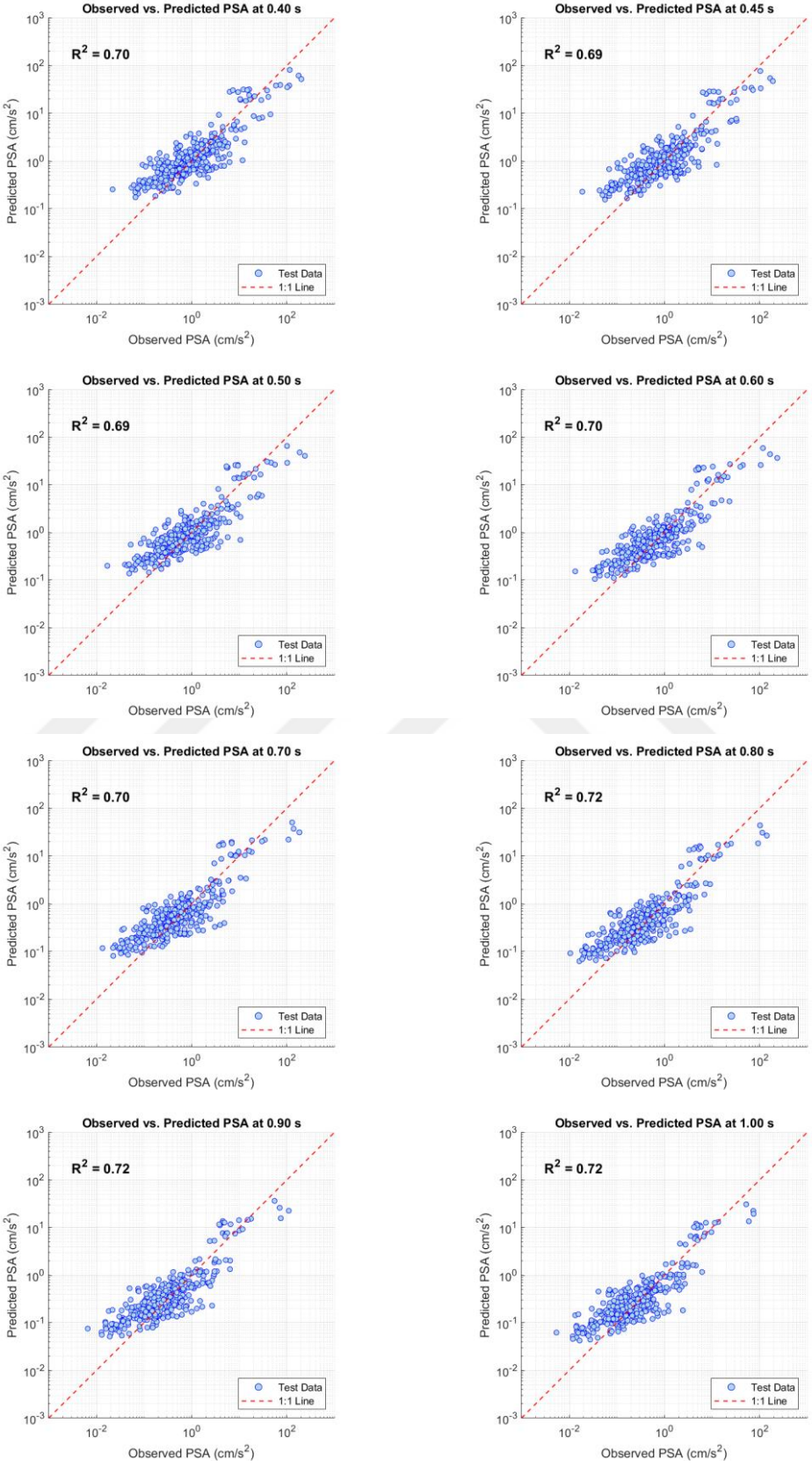

Figure B.2. Predicted versus observed PGA, PSAs at 0.02-5 seconds and PGV comparisons (cont.).

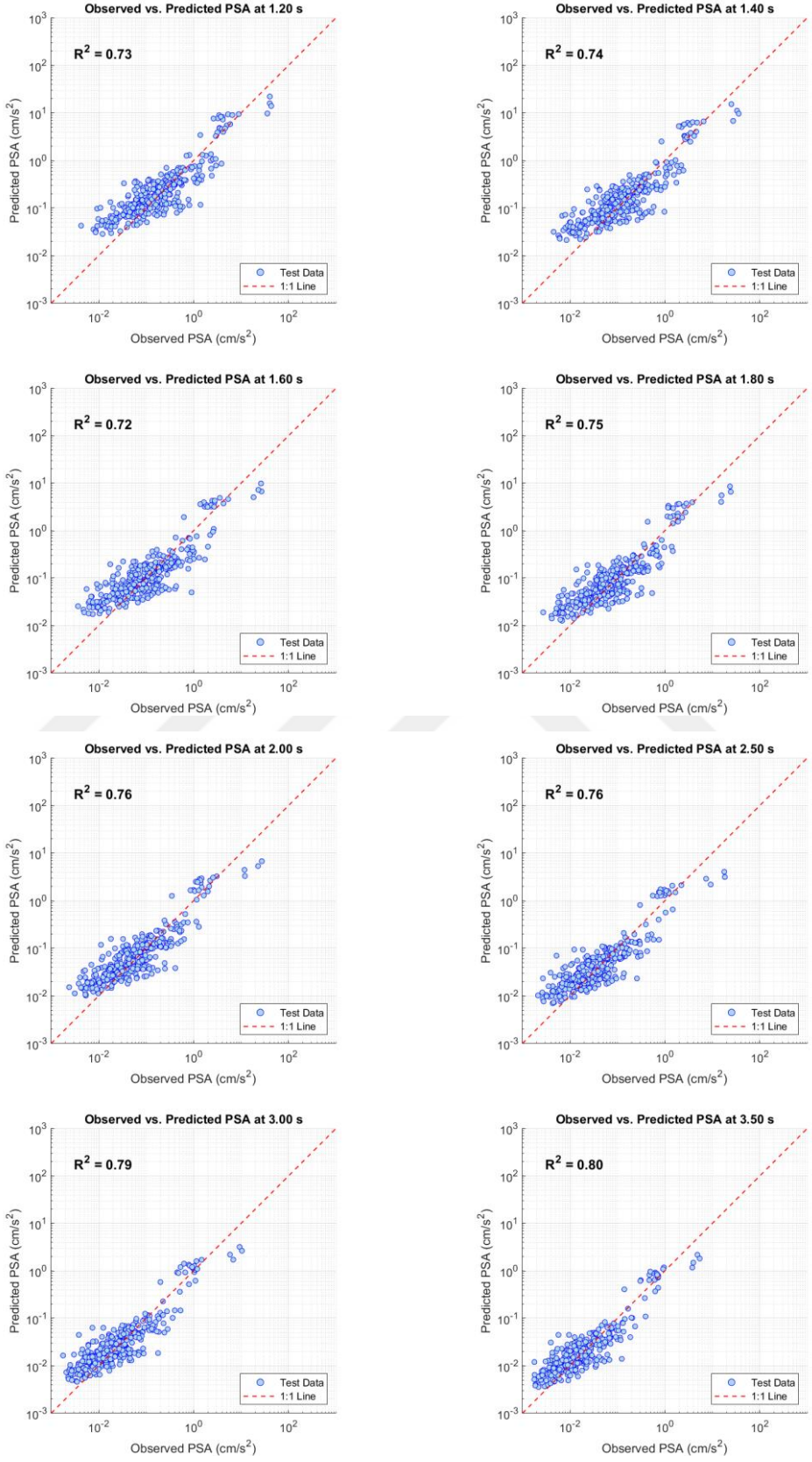

Figure B.2. Predicted versus observed PGA, PSAs at 0.02-5 seconds and PGV comparisons (cont.).

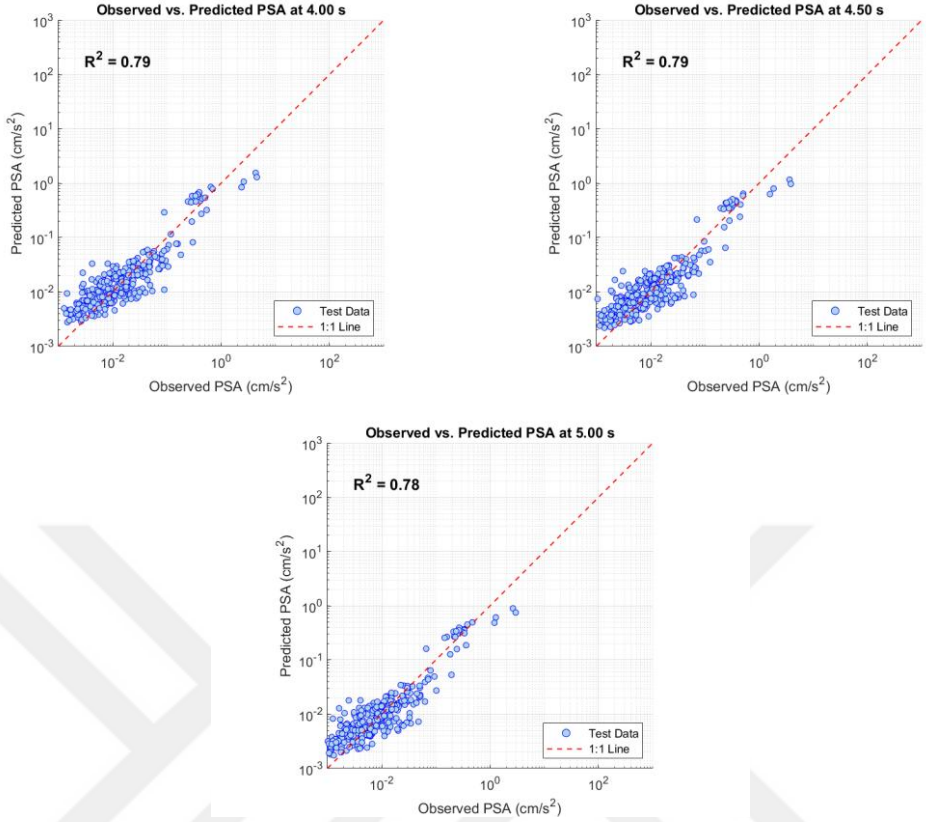

Figure B.2. Predicted versus observed PGA, PSAs at 0.02-5 seconds and PGV comparisons (cont.).

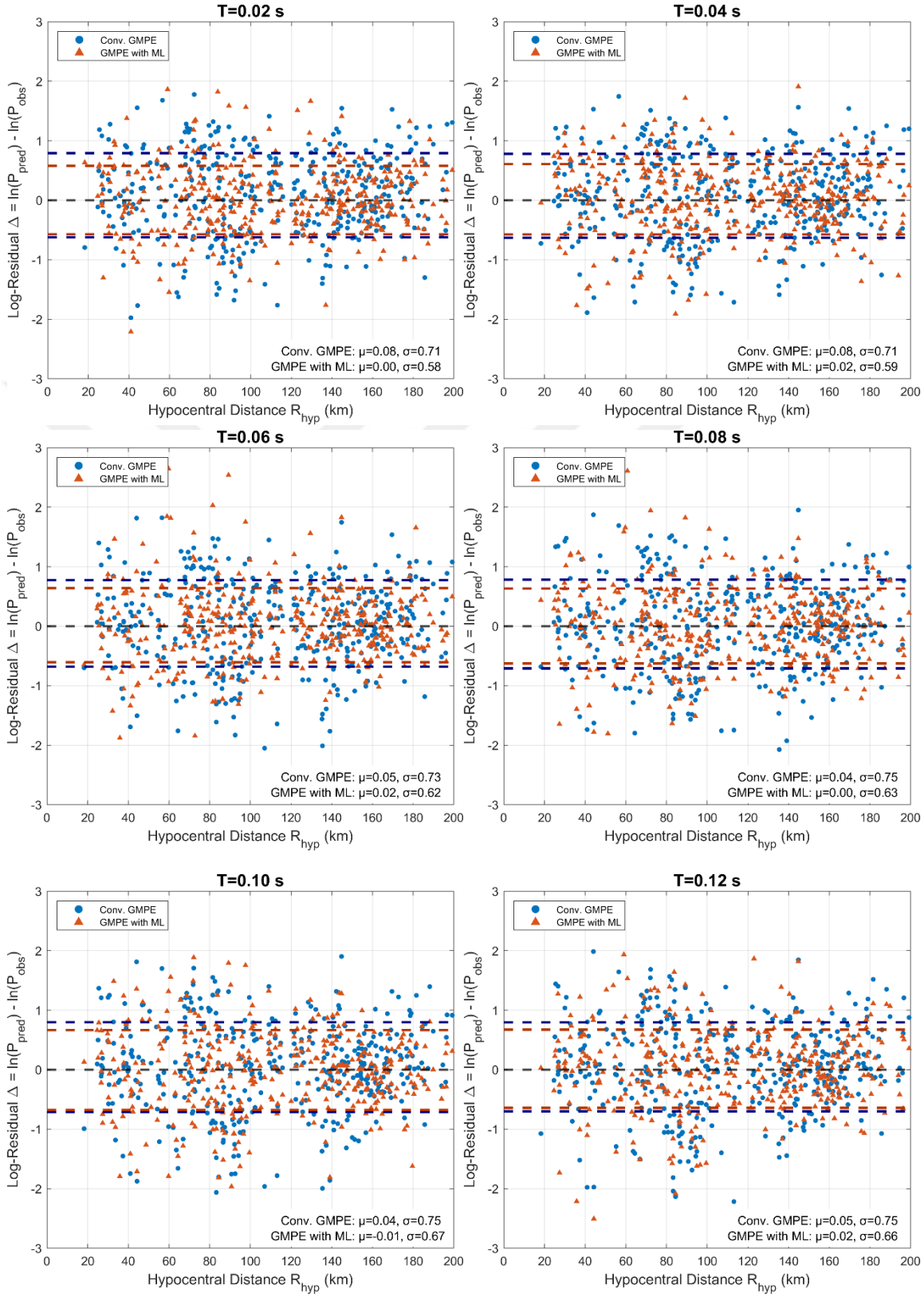

Figure B.3. Residual Analysis of the GMPEs as a function of hypocentral distance for PSA at periods 0.02–5.0 s.

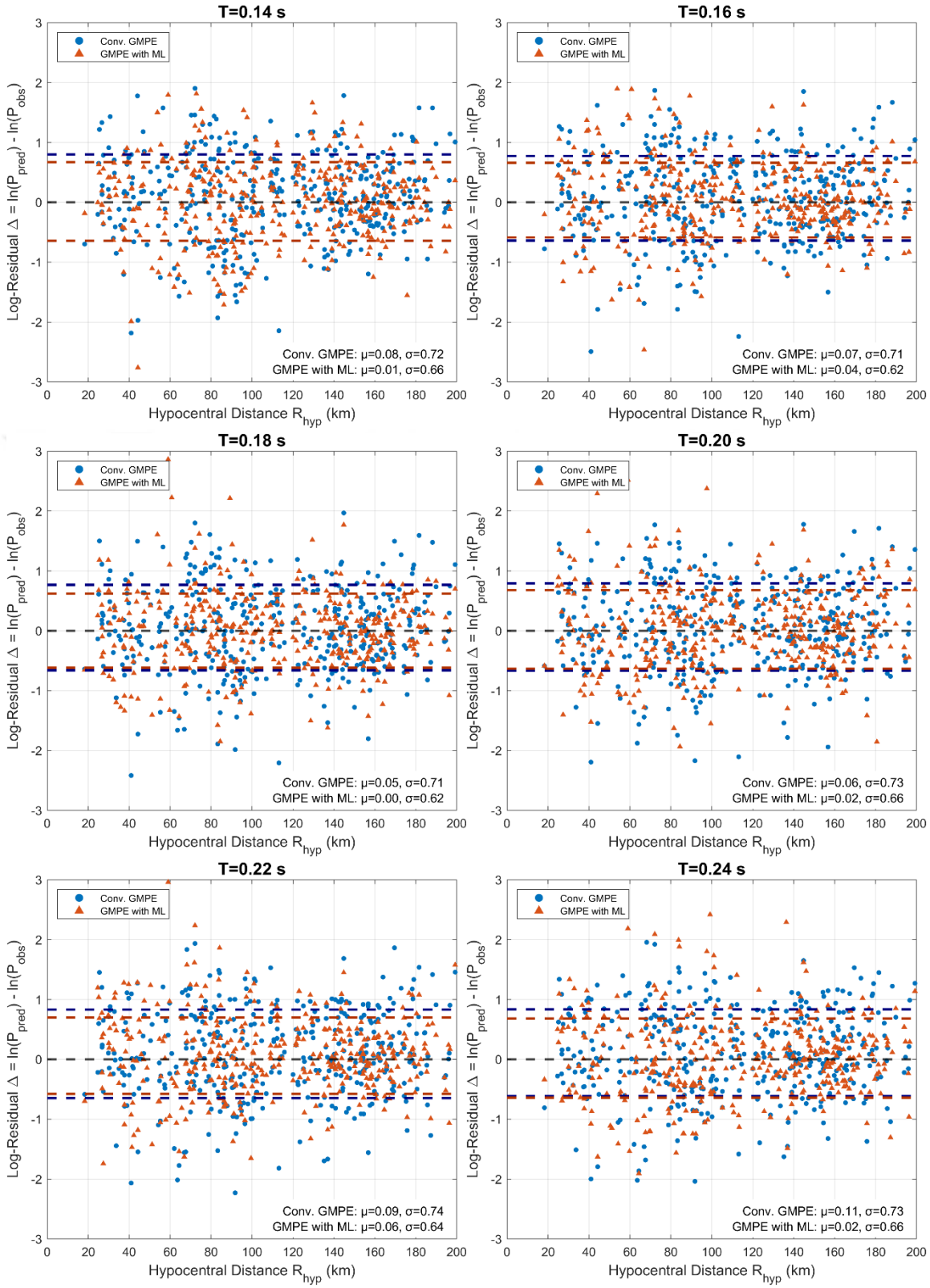

Figure B.3. Residual Analysis of the GMPEs as a function of hypocentral distance for PSA at periods 0.02–5.0 s (cont.).

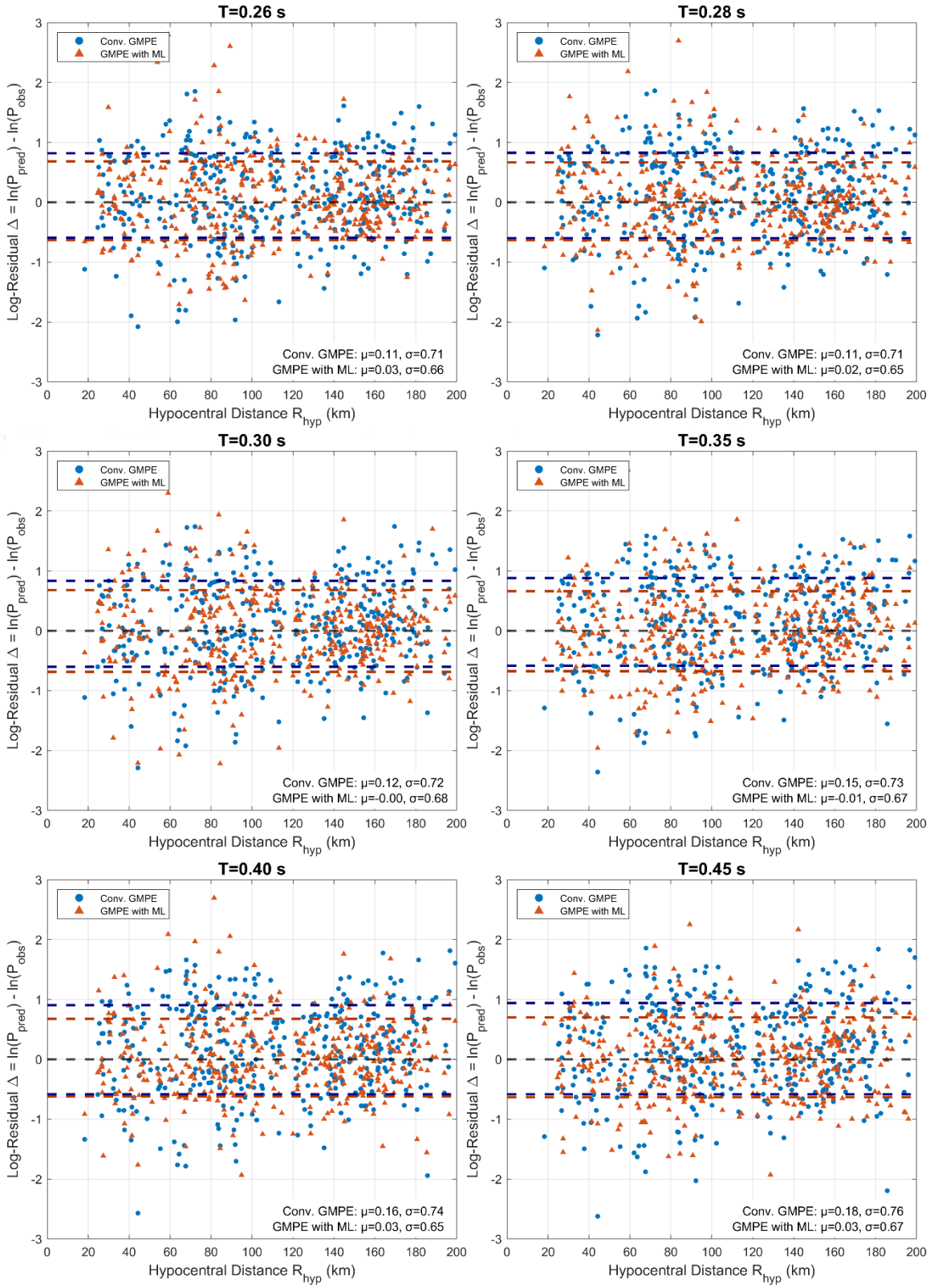

Figure B.3. Residual Analysis of the GMPEs as a function of hypocentral distance for PSA at periods 0.02–5.0 s (cont.).

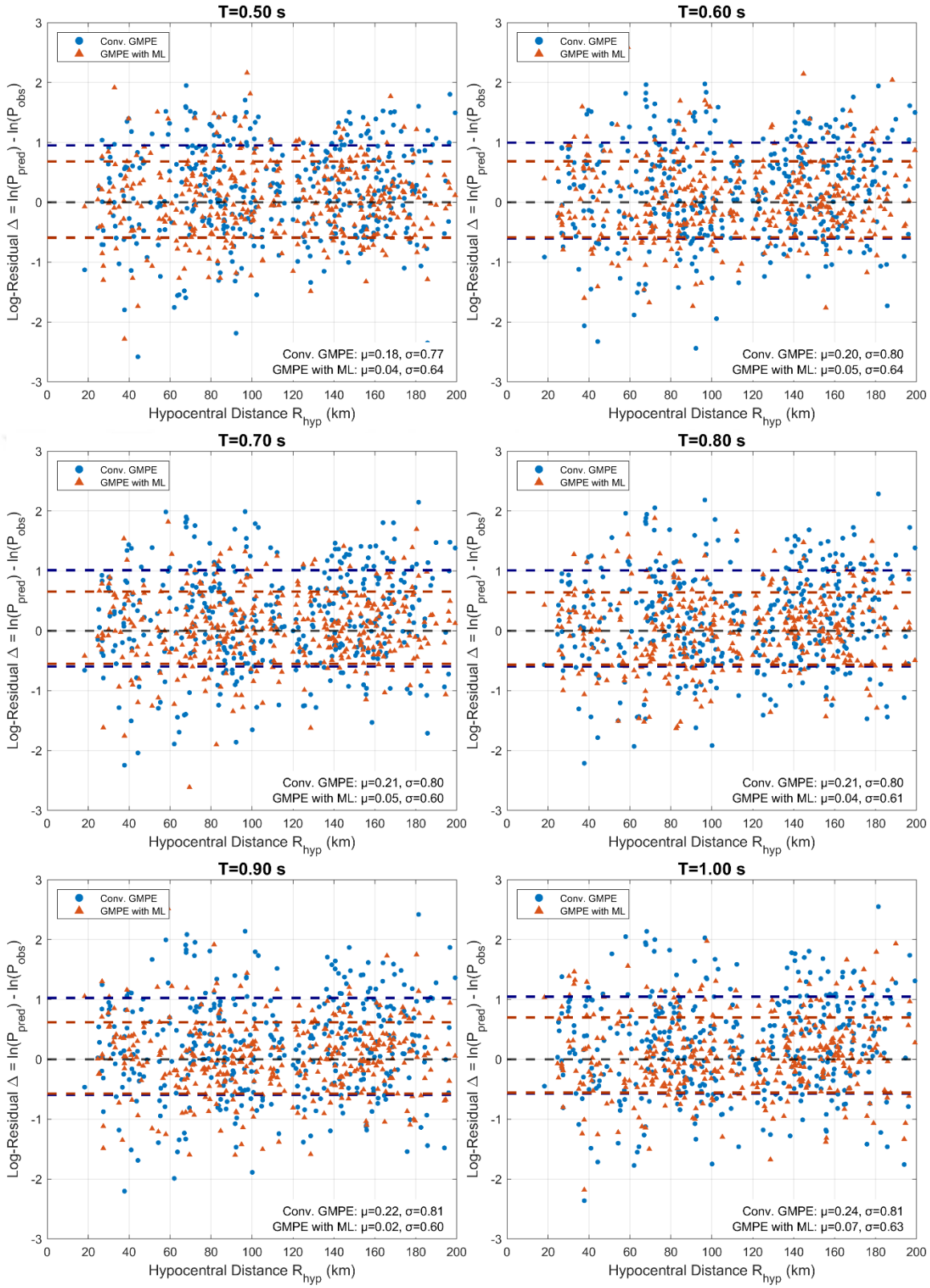

Figure B.3. Residual Analysis of the GMPEs as a function of hypocentral distance for PSA at periods 0.02–5.0 s (cont.).

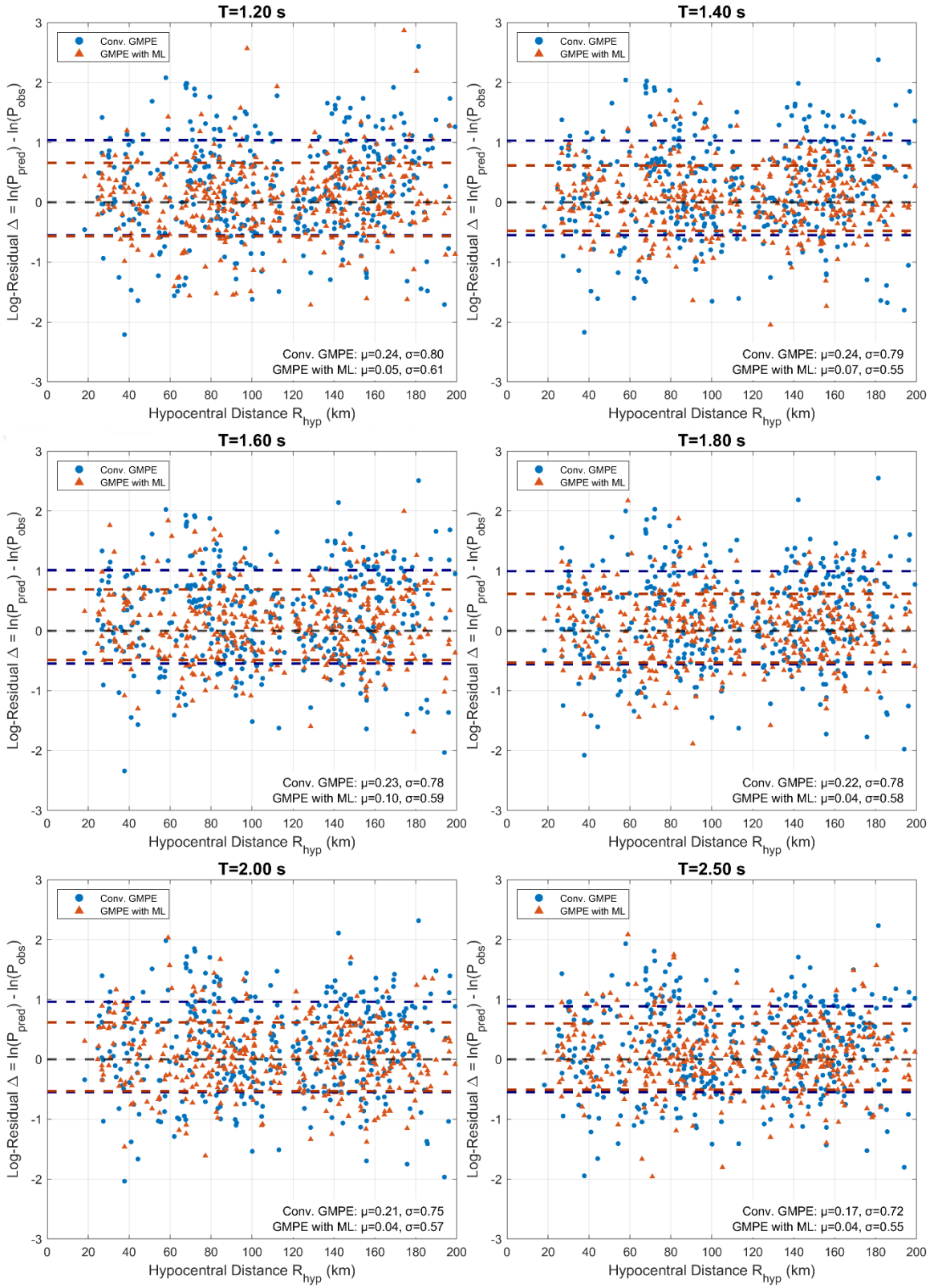

Figure B.3. Residual Analysis of the GMPEs as a function of hypocentral distance for PSA at periods 0.02–5.0 s (cont.).

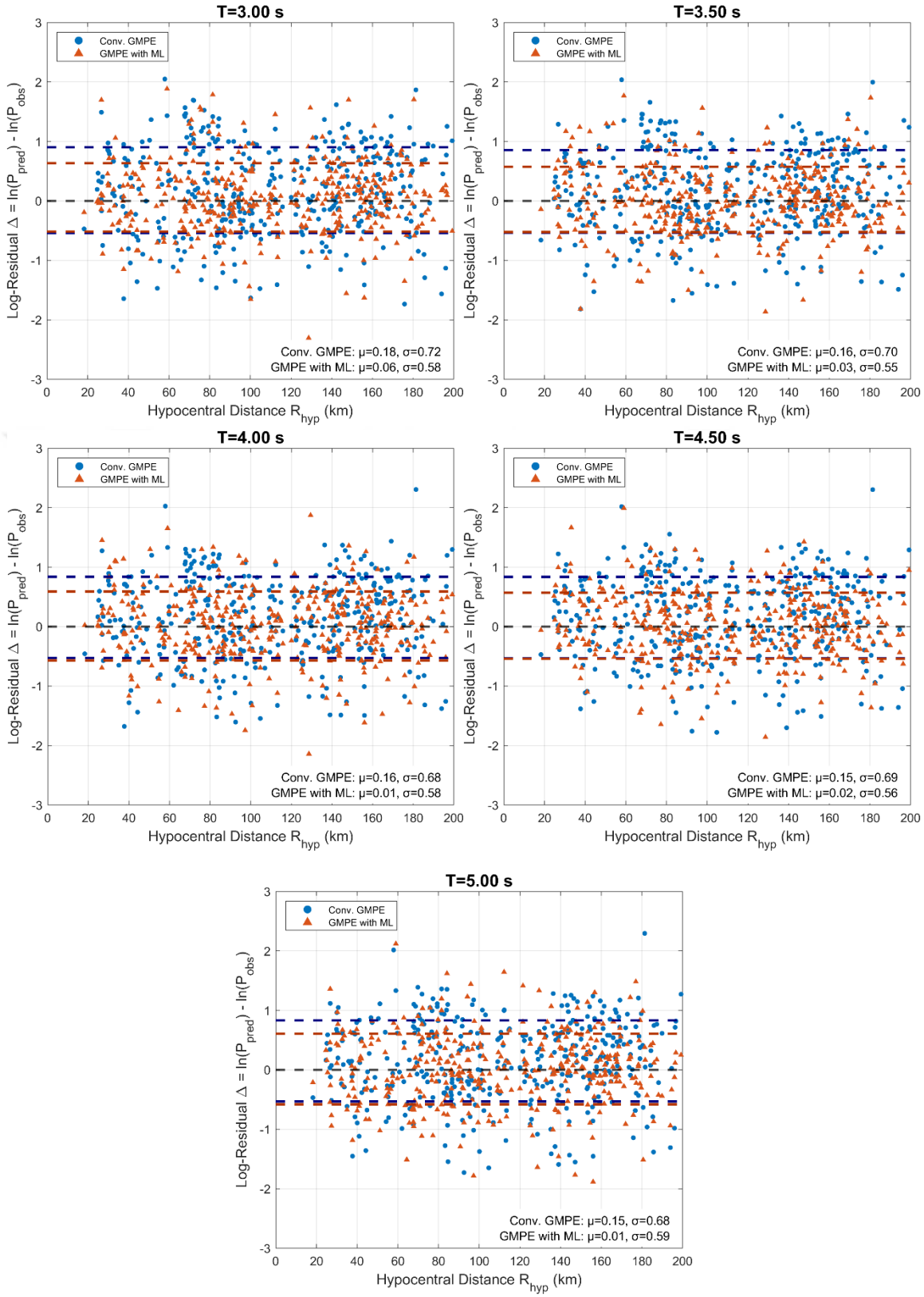

Figure B.3. Residual Analysis of the GMPEs as a function of hypocentral distance for PSA at periods 0.02–5.0 s (cont.).

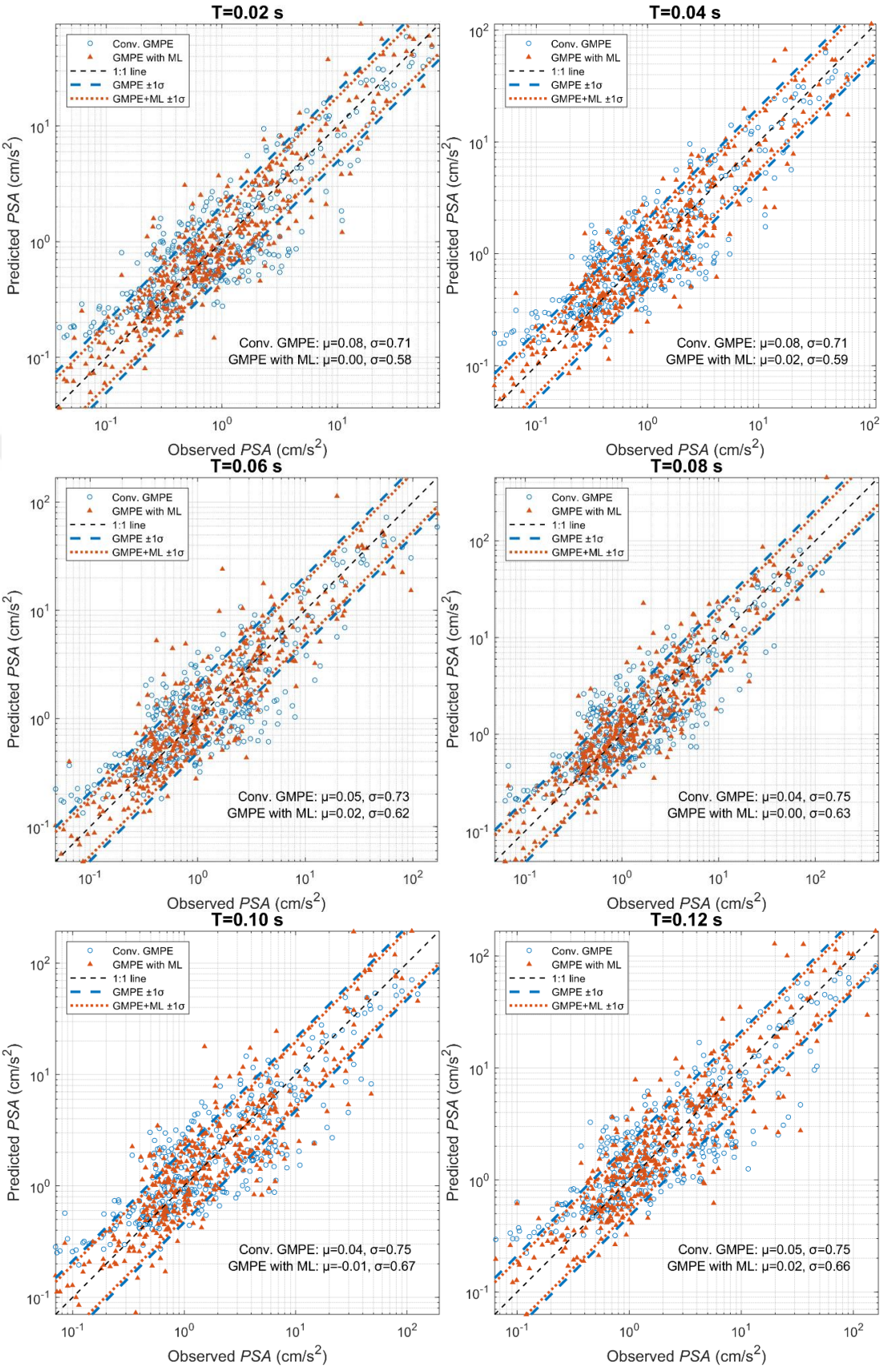

Figure B.4. Comparisons between observed PSA and GMPE predictions across the 0.02–5.0 s period range.

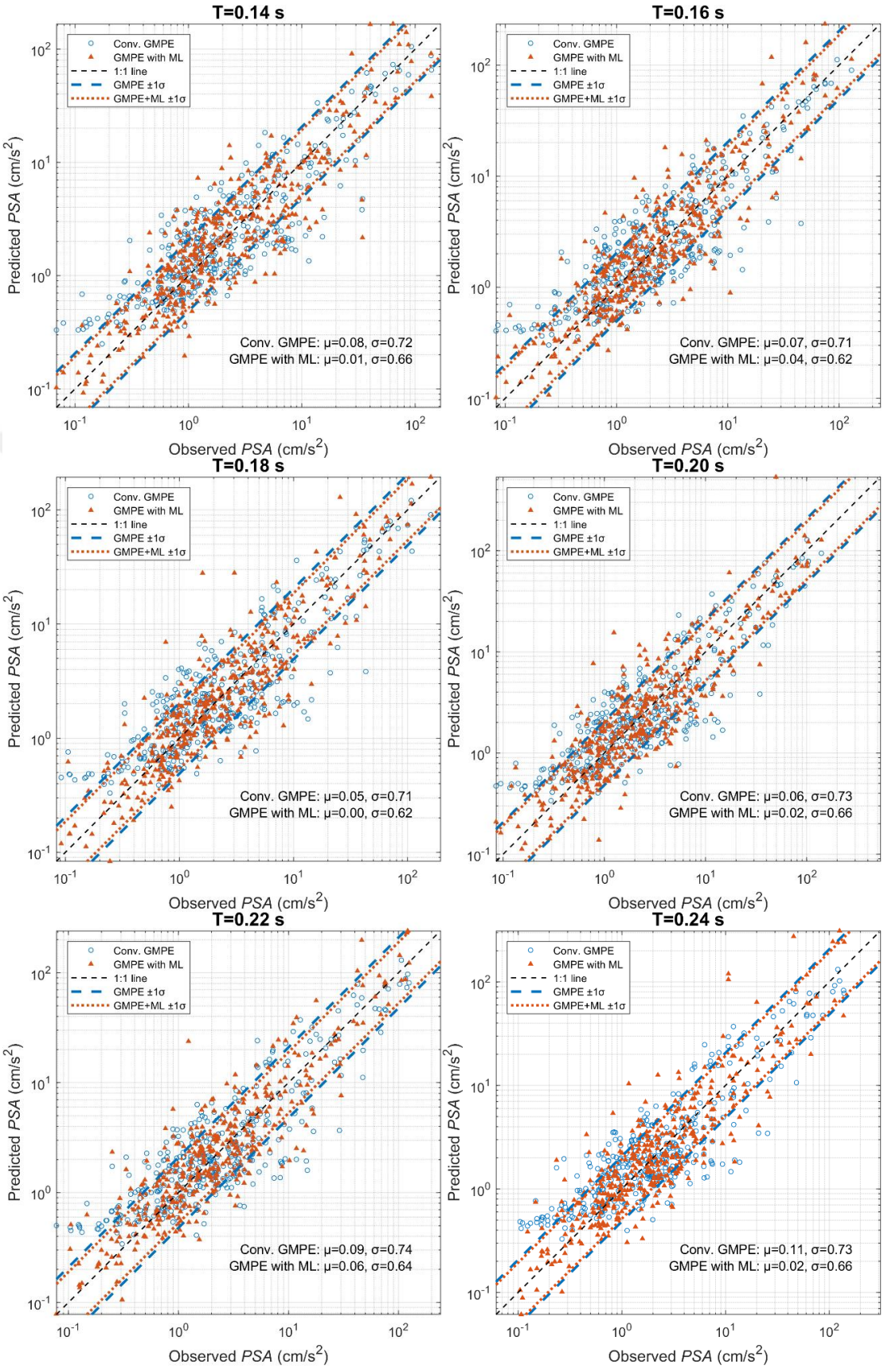

Figure B.4. Comparisons between observed PSA and GMPE predictions across the 0.02–5.0 s period range (cont.).

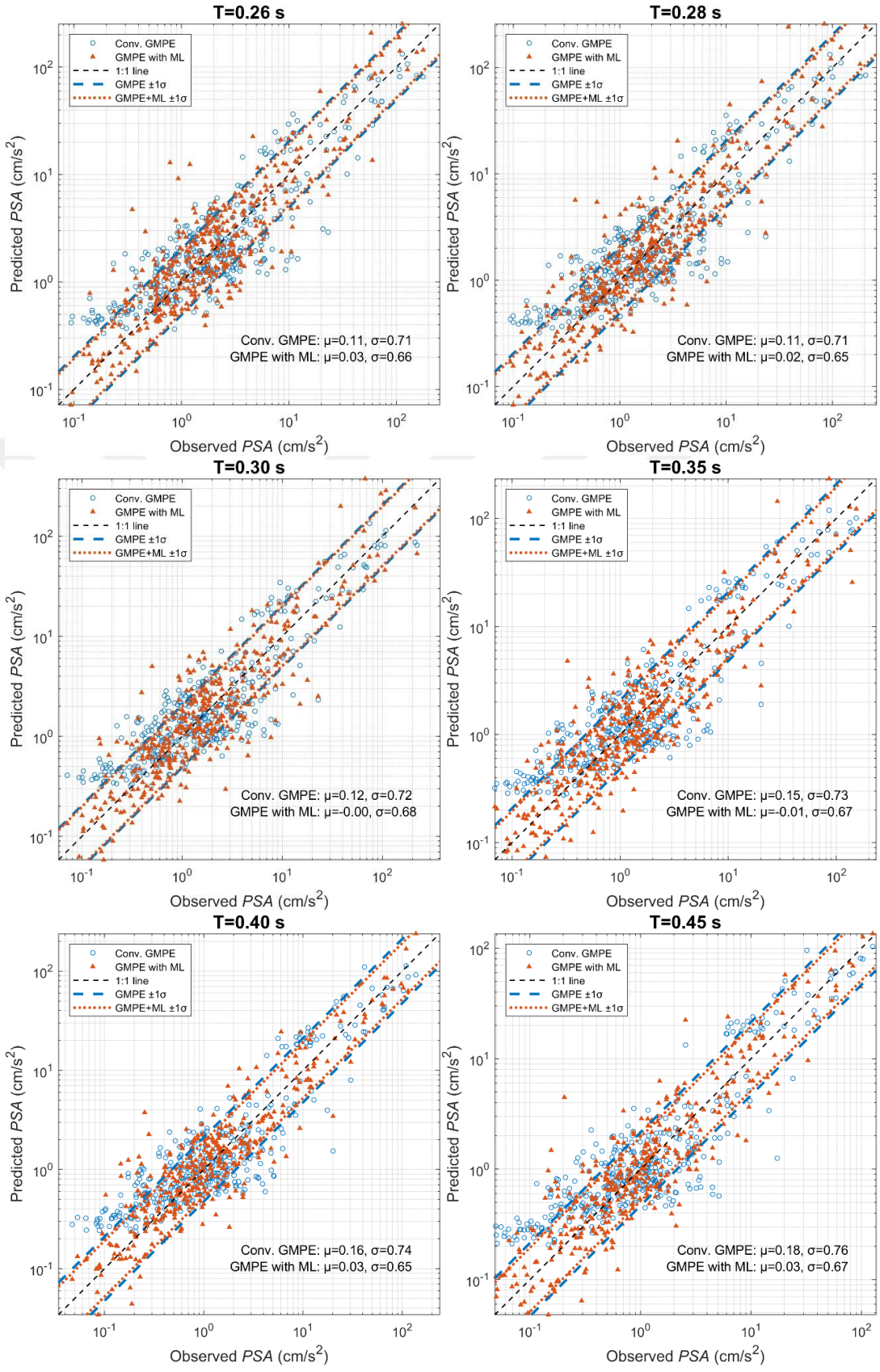

Figure B.4. Comparisons between observed PSA and GMPE predictions across the 0.02–5.0 s period range (cont.).

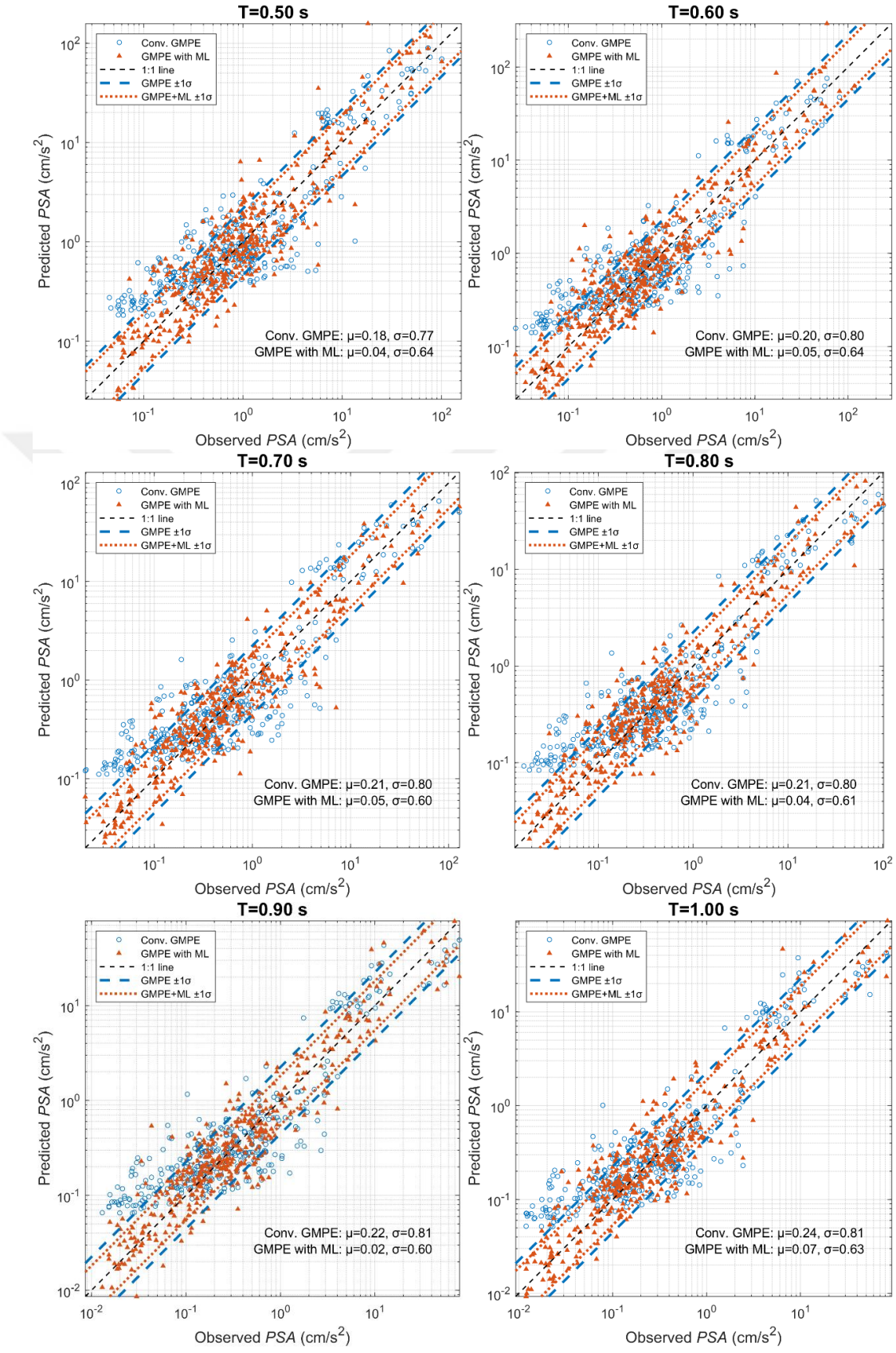

Figure B.4. Comparisons between observed PSA and GMPE predictions across the 0.02–5.0 s period range (cont.).

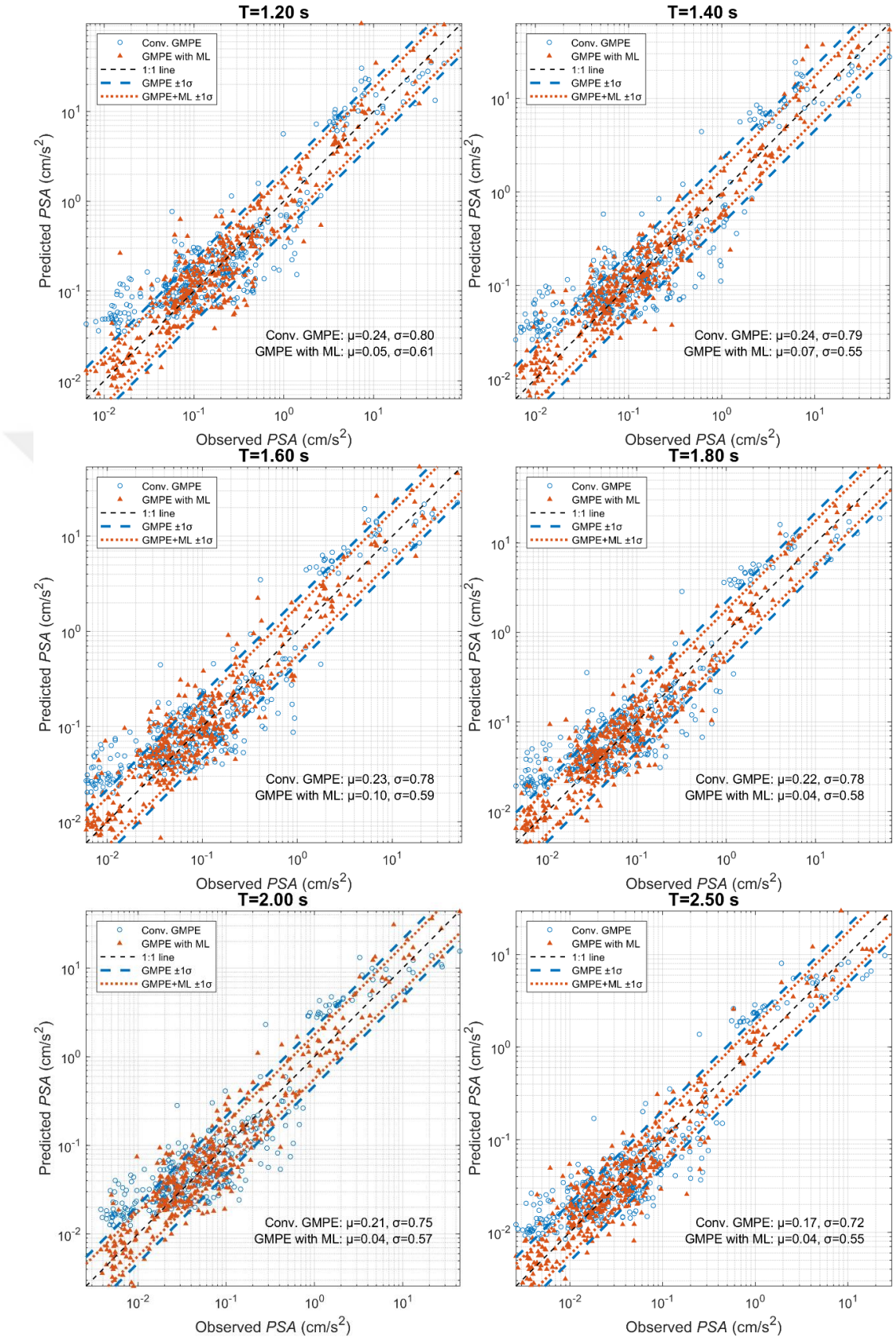

Figure B.4. Comparisons between observed PSA and GMPE predictions across the 0.02–5.0 s period range (cont.).

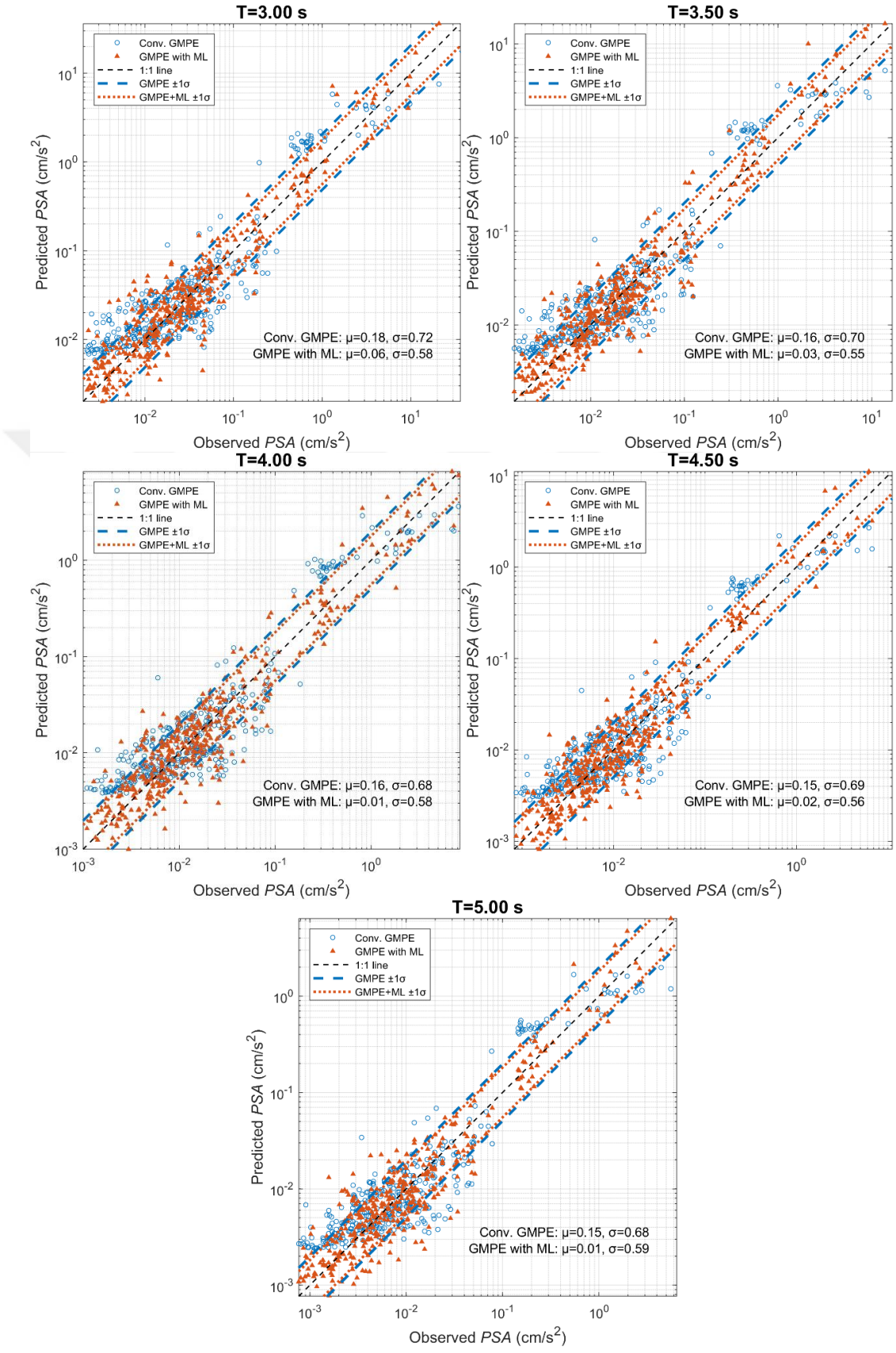

Figure B.4. Comparisons between observed PSA and GMPE predictions across the 0.02–5.0 s period range (cont.).

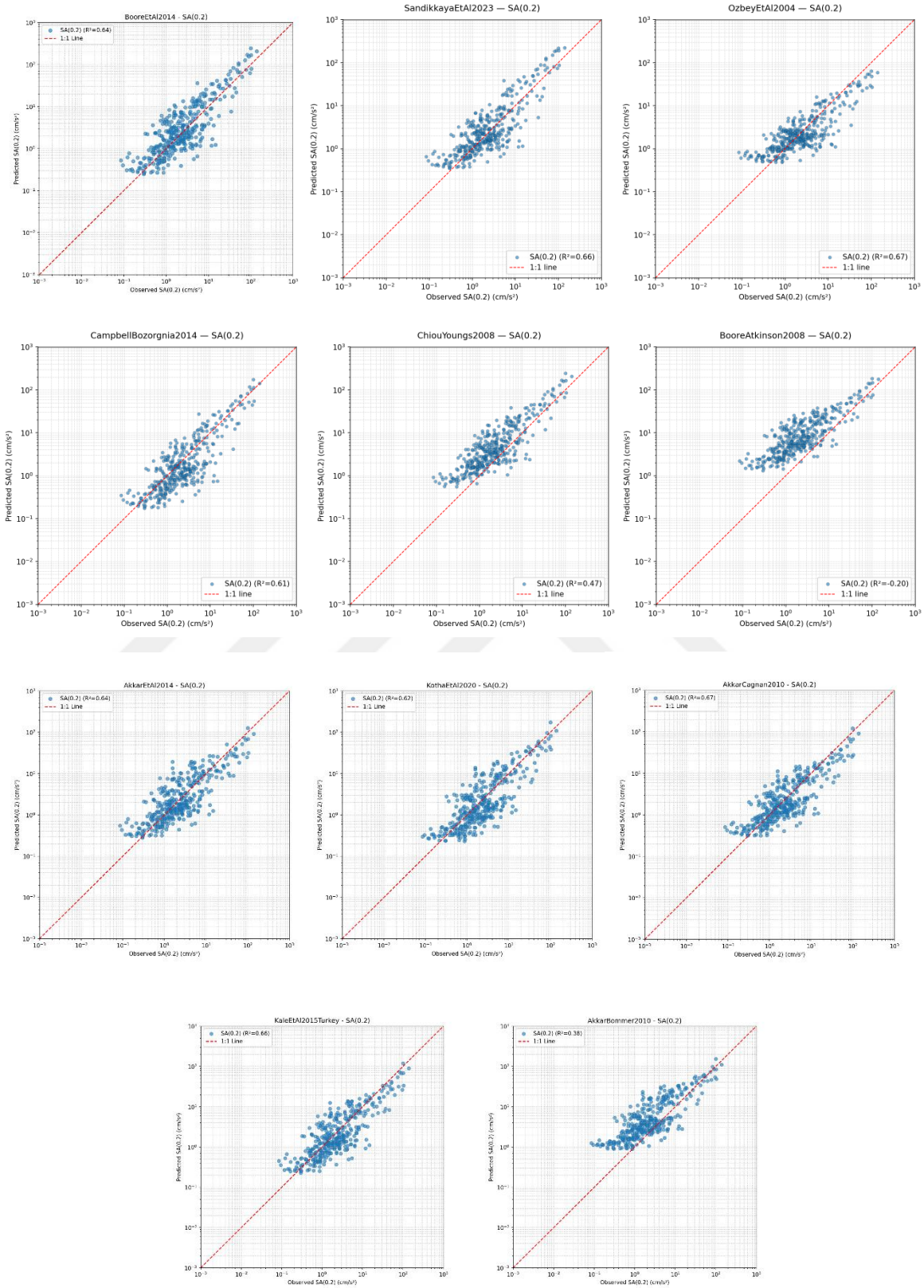

Figure B.5. Comparison of observed and predicted PSA at 0.2 s using the GMPE developed in this study, benchmarked against alternative GMPEs.

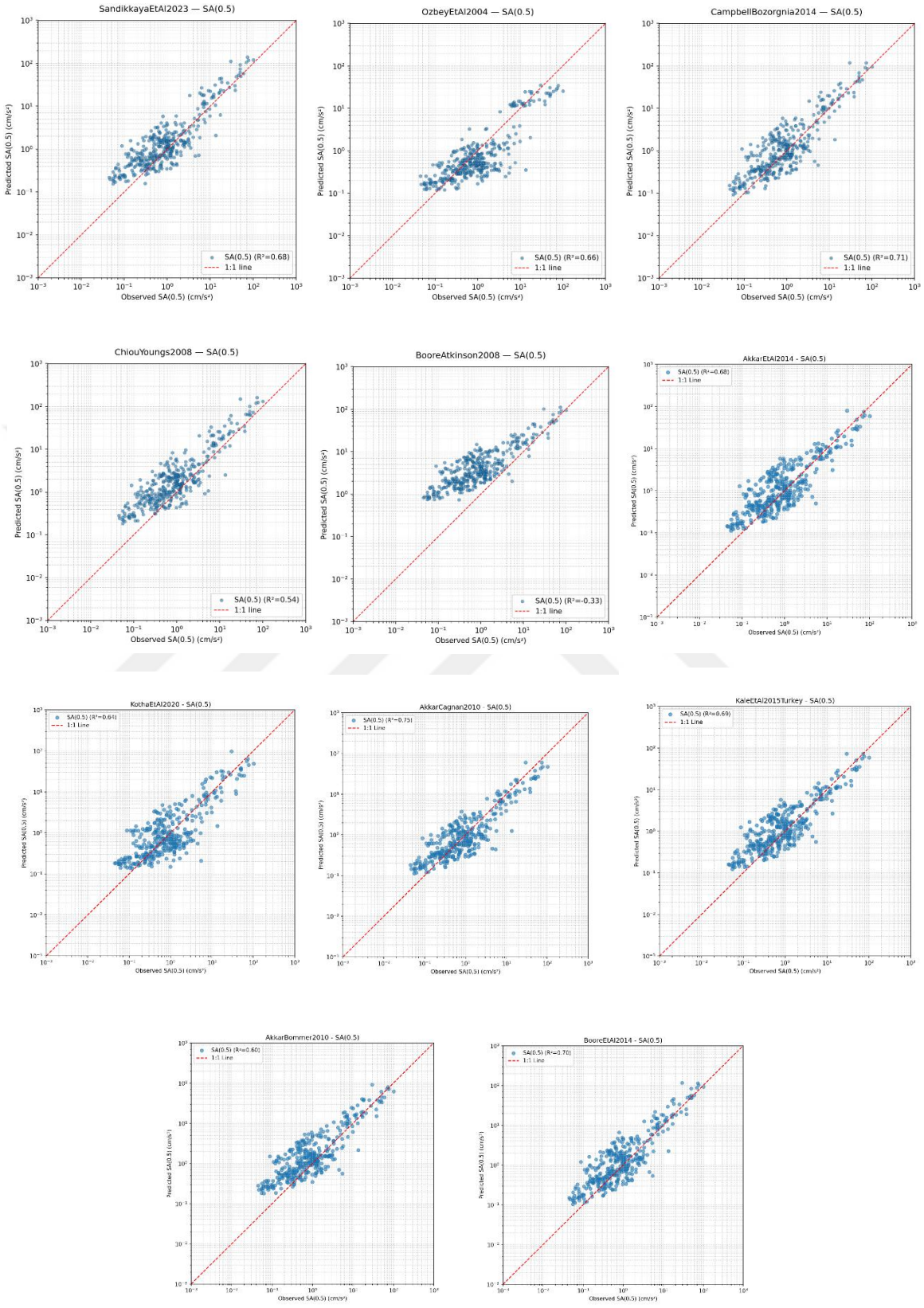

Figure B.6. Comparison of observed and predicted PSA at 0.5 s using the GMPE developed in this study, benchmarked against alternative GMPEs.

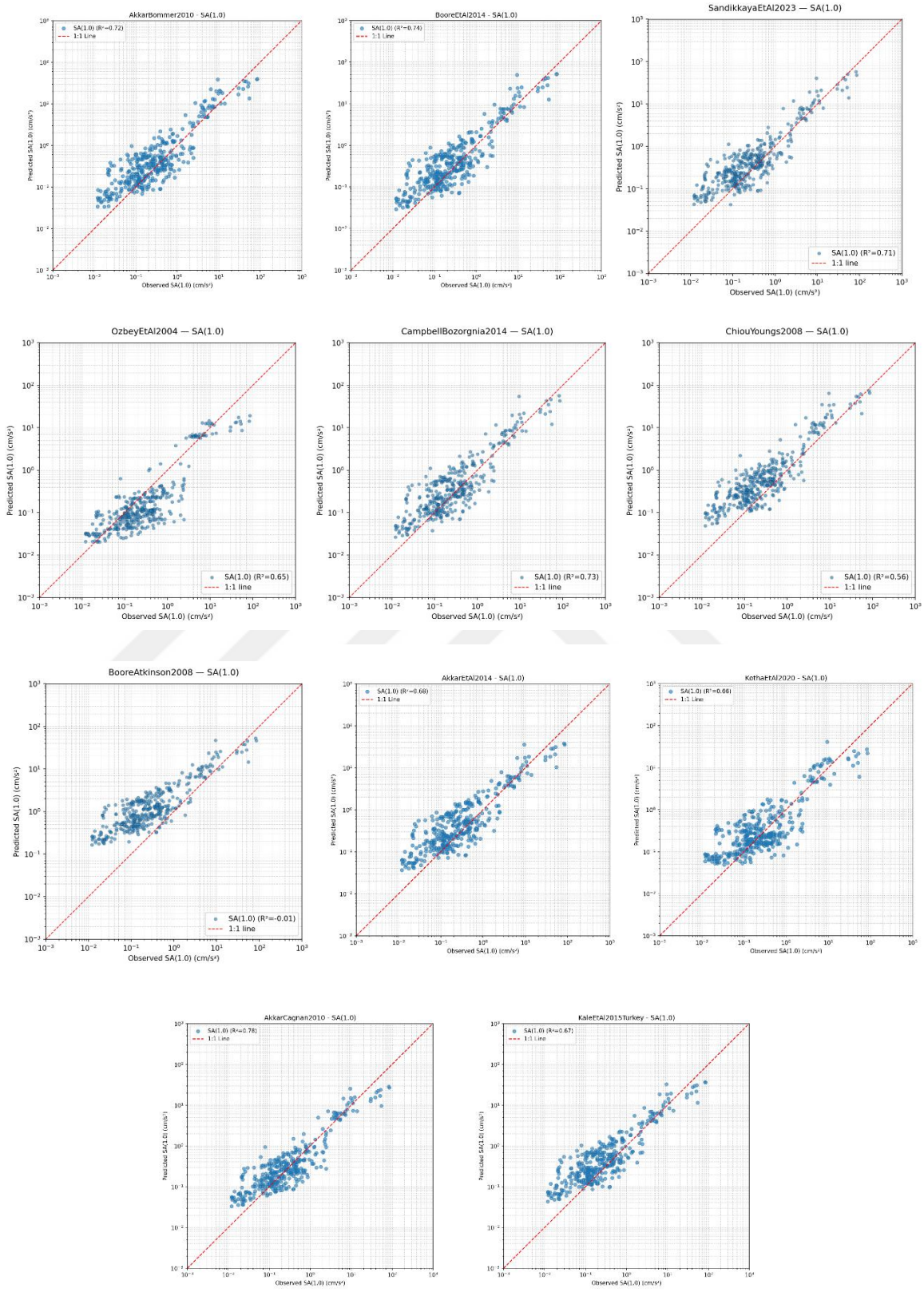

Figure B.7. Comparison of observed and predicted PSA at 1.0 s using the GMPE developed in this study, benchmarked against alternative GMPEs.

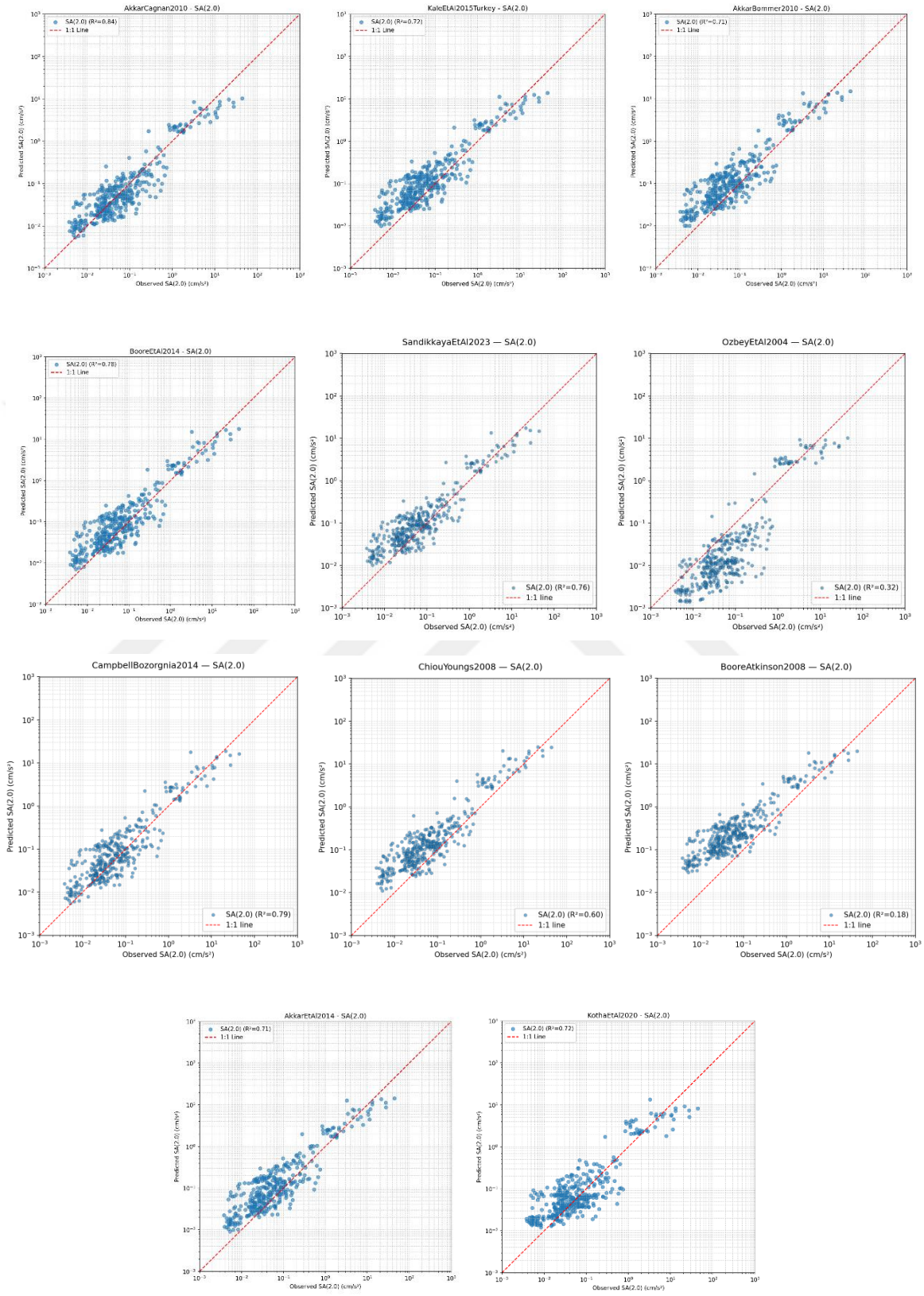

Figure B.8. Comparison of observed and predicted PSA at 2.0 s using the GMPE developed in this study, benchmarked against alternative GMPEs.

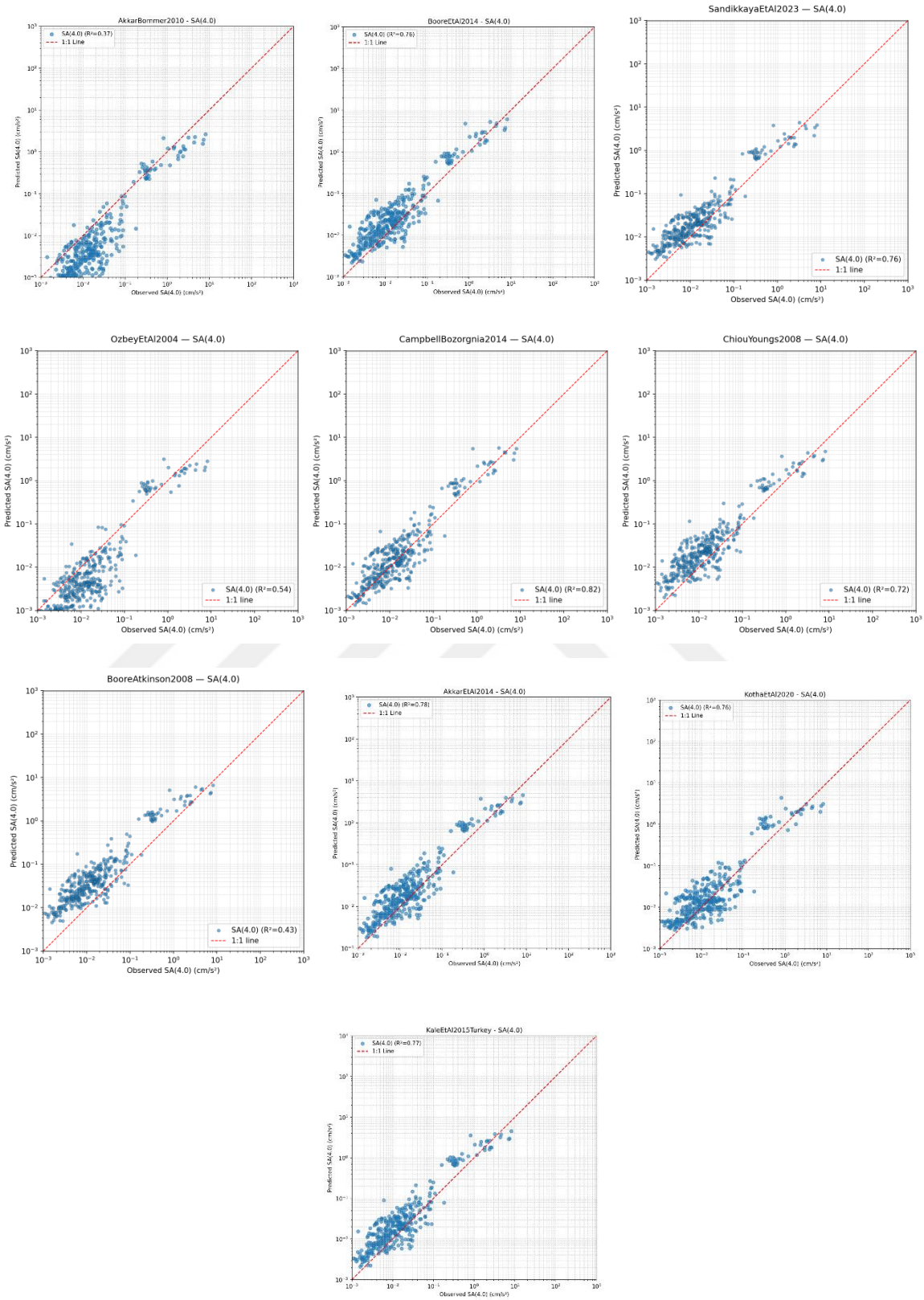

Figure B.9. Comparison of observed and predicted PSA at 4.0 s using the GMPE developed in this study, benchmarked against alternative GMPEs.

APPENDIX C: PERIOD-DEPENDENT SPATIAL CORRELATION MODELS

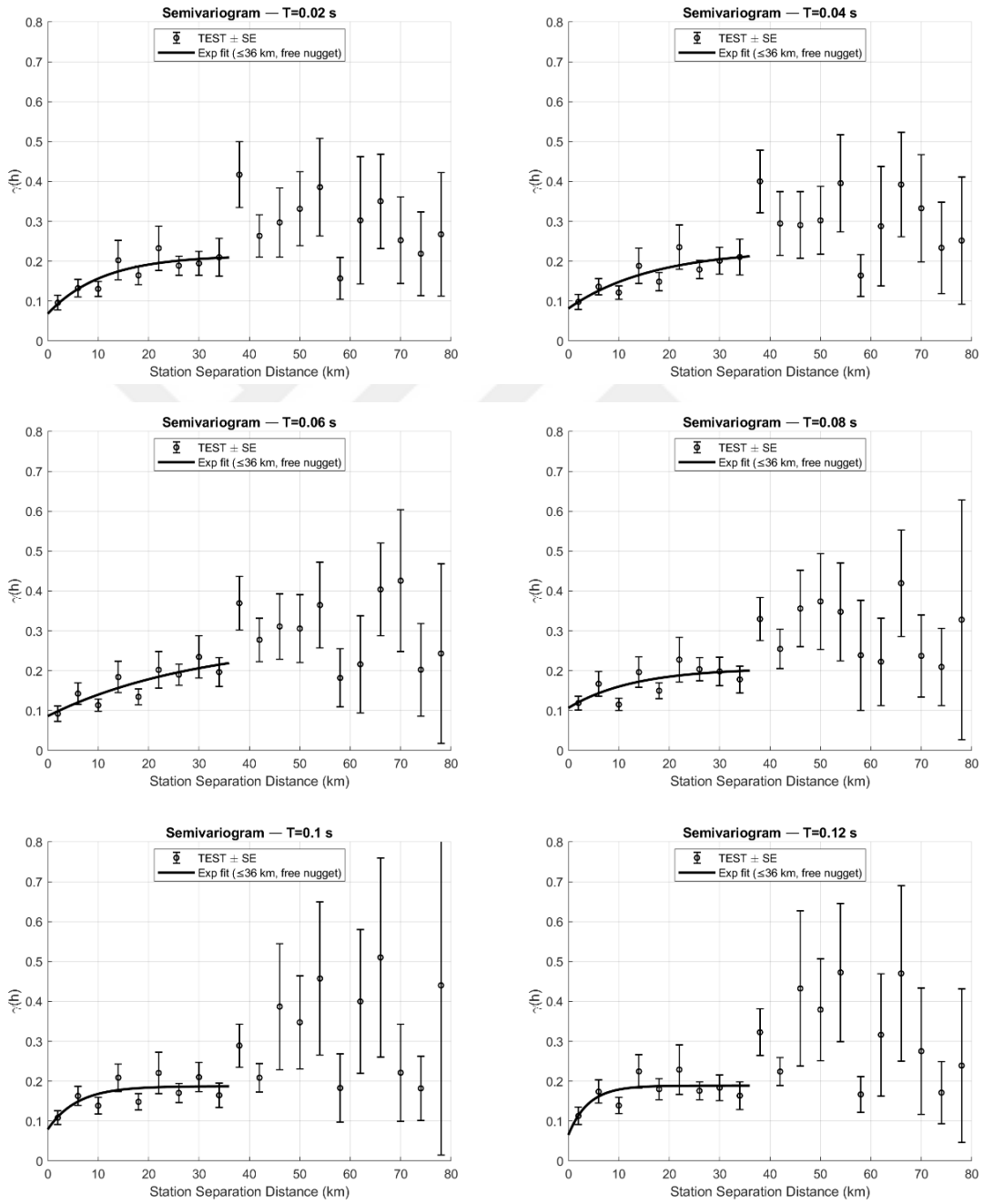

Figure C.1. Empirical semivariogram for periods between 0.02 – 5 seconds and PGV; circles represent mean values, while error ranges show ±1 standard deviation at distance bins.

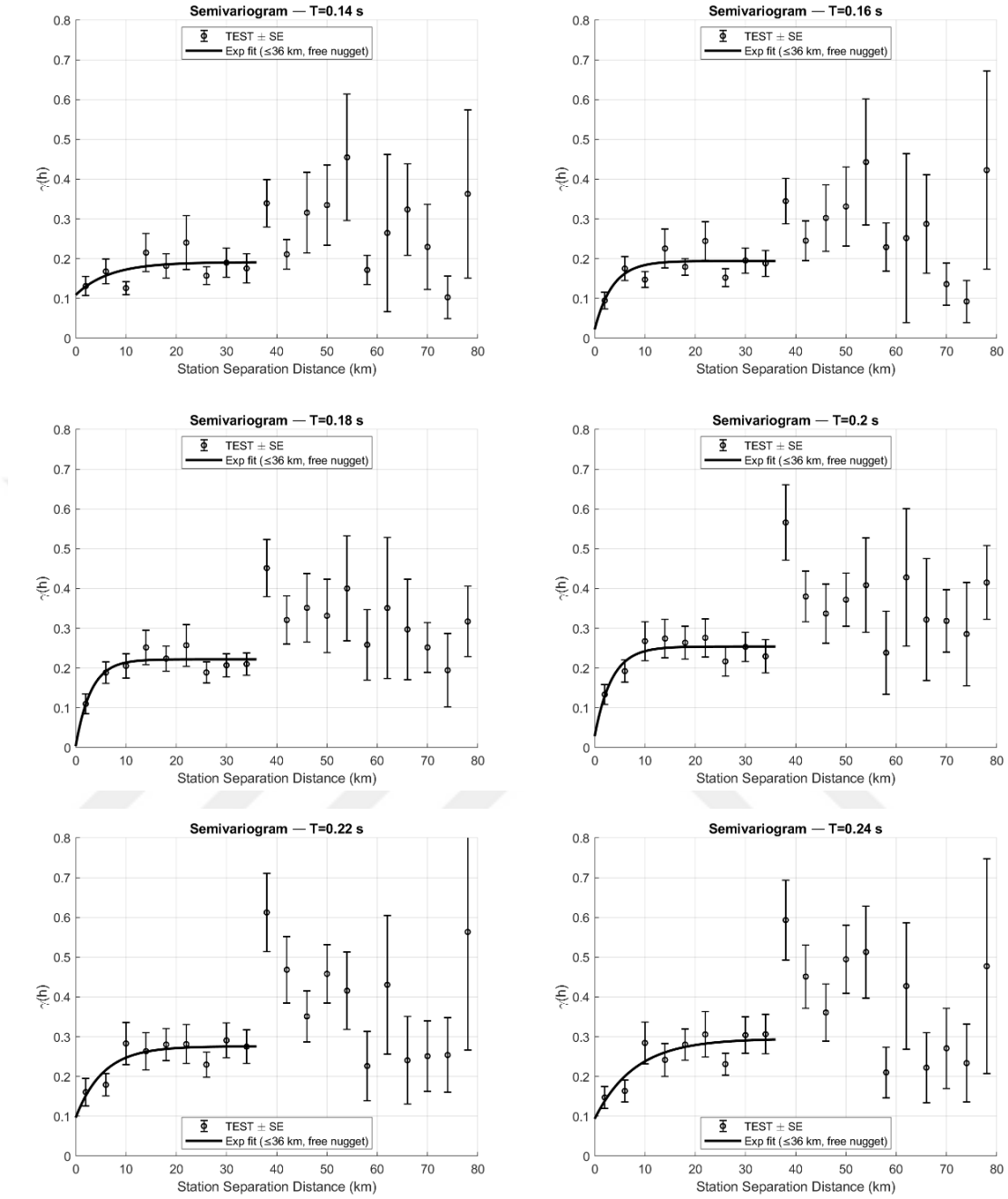

Figure C.1. Empirical semivariogram for periods between 0.02 – 5 seconds and PGV; circles represent mean values, while error ranges show ±1 standard deviation at distance bins (cont.).

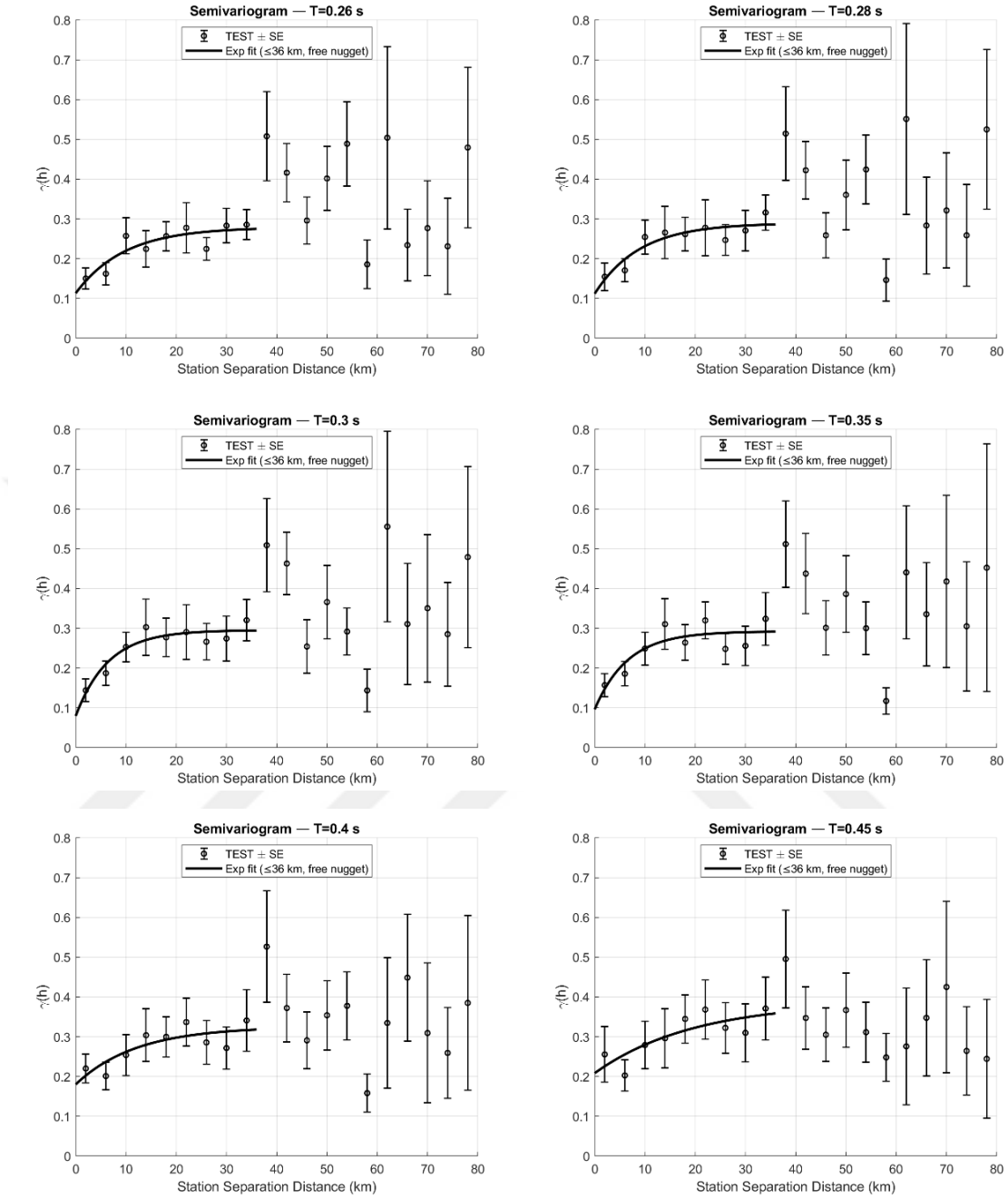

Figure C.1. Empirical semivariogram for periods between 0.02 – 5 seconds and PGV; circles represent mean values, while error ranges show ±1 standard deviation at distance bins (cont.).

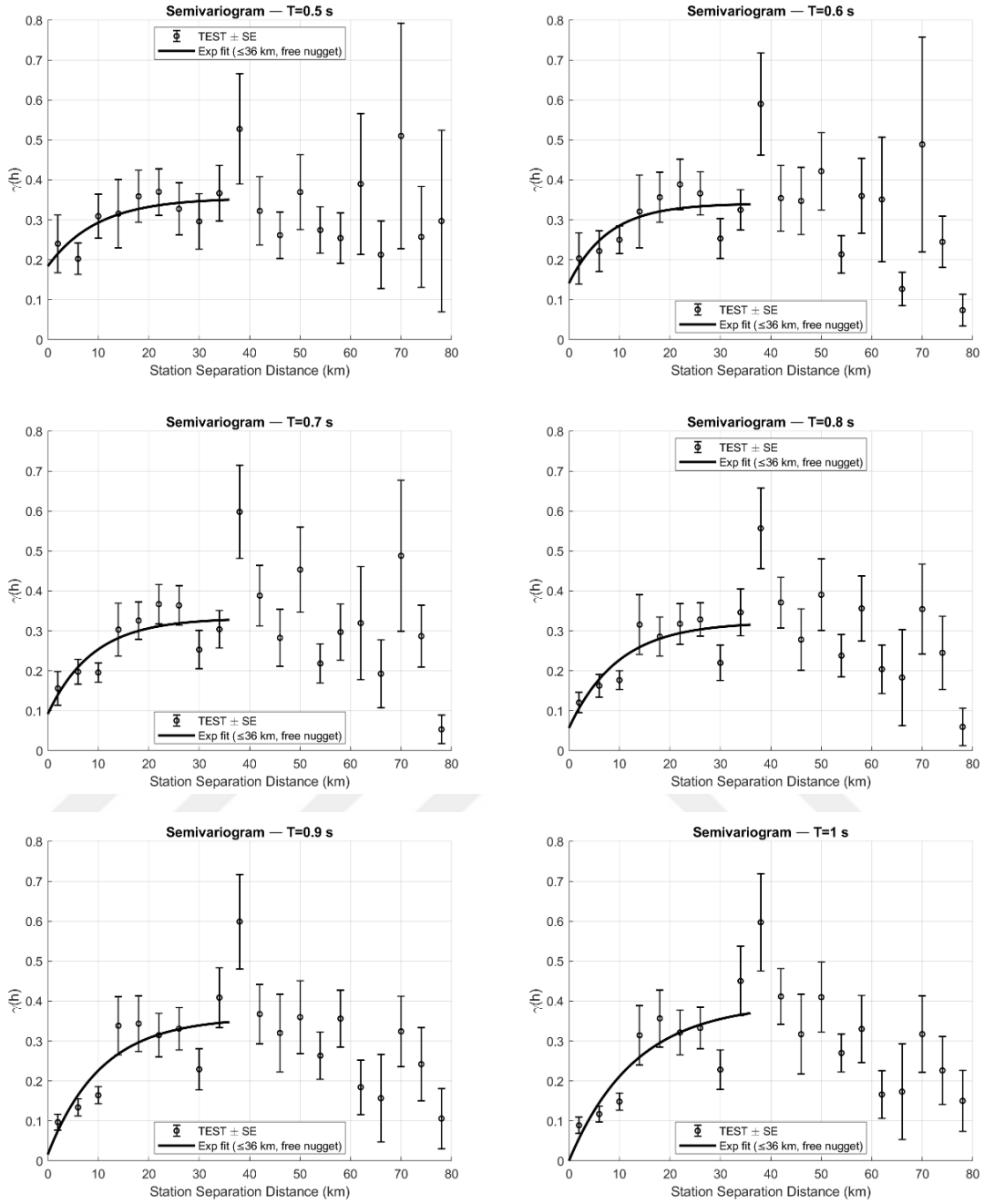

Figure C.1. Empirical semivariogram for periods between 0.02 – 5 seconds and PGV; circles represent mean values, while error ranges show ±1 standard deviation at distance bins (cont.).

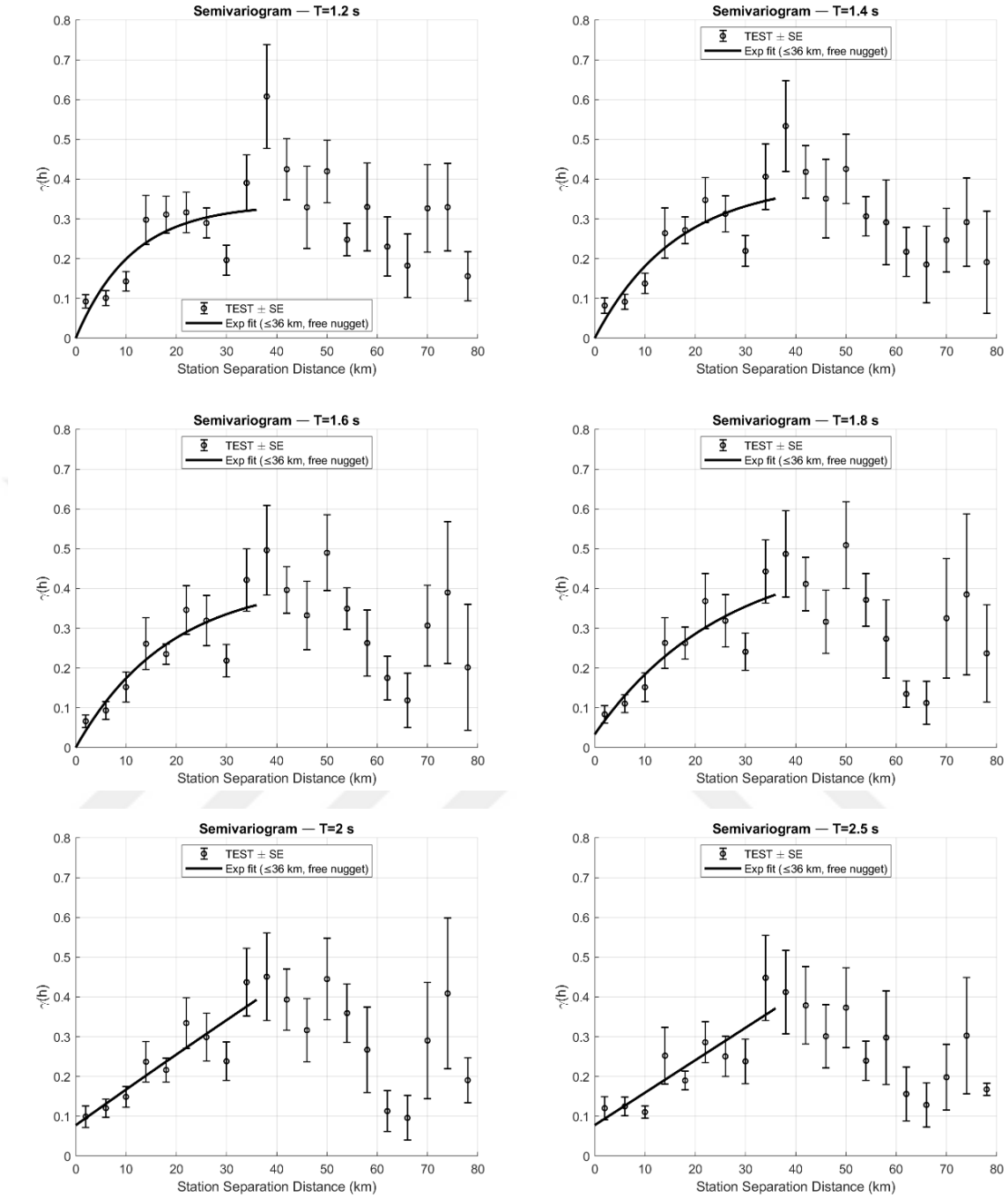

Figure C.1. Empirical semivariogram for periods between 0.02 – 5 seconds and PGV; circles represent mean values, while error ranges show ±1 standard deviation at distance bins (cont.).

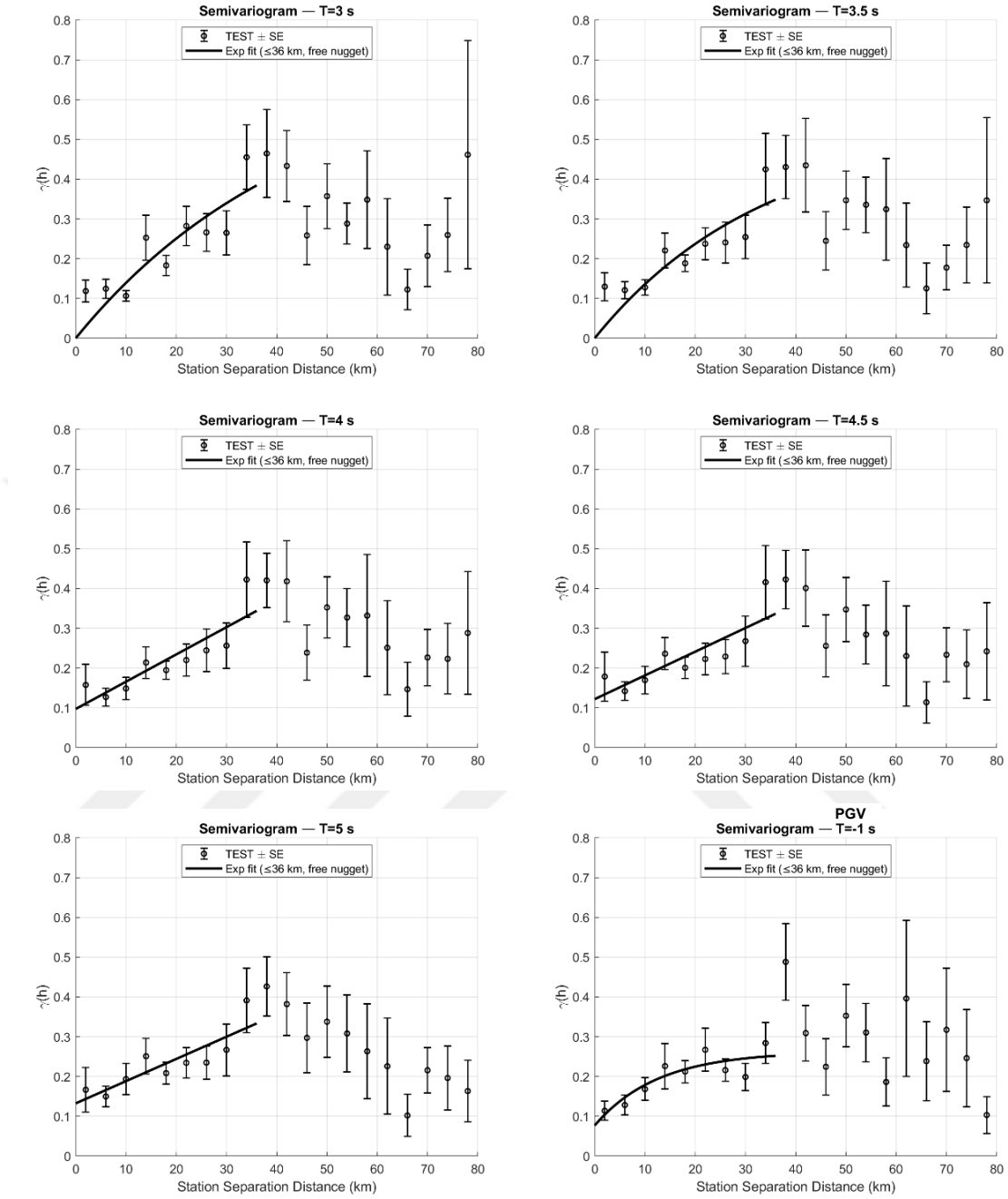

Figure C.1. Empirical semivariogram for periods between 0.02 – 5 seconds and PGV; circles represent mean values, while error ranges show ±1 standard deviation at distance bins (cont.).